MAGNETOSPHERIC IMAGING: PROMISE TO REALITY

J. L. Burch

Southwest Research Institute

San Antonio, Texas, USA

Measurements of the plasmas, energetic particles, and electric and magnetic fields within the Earth's magnetosphere have been made with ever greater coverage and precision throughout the past 46 years; but until recently no images were available of this important environment. However, for two decades or more, theoretical estimates, data from sounding rockets, and background signals from orbiting instruments designed for in-situ ion measurements accumulated to show that most of the plasmas contained in the inner magnetosphere could be imaged if new instruments designed for the purpose could be placed in a suitable high-altitude orbit. With the launch of the NASA IMAGE satellite in March 2000, the promise of magnetospheric imaging began to be realized. IMAGE provides nearly continuous imaging of the inner magnetosphere on a nominal time scale of two minutes. The discoveries made by IMAGE during its first five years of operation are reviewed in this paper.

1. INTRODUCTION

The Earth's magnetosphere is a cavity formed in the solar wind to first order by a balance between the static pressure of the geomagnetic field and the dynamic pressure of the solar wind. A cross-sectional sketch of the magnetosphere in the noon-midnight meridian is shown in **Figure 1**. The magnetosphere is defined by magnetic fields that connect to the Earth and is filled with plasmas that enter it from the Earth's ionosphere and the solar wind. The magnetospheric plasmas undergo episodically dynamic behavior because of the presence of both steady and variable electric fields, which have several different origins. A constant electric field is caused by the Earth's rotation, which carries the geomagnetic field and, by frictional forces, the atmosphere along with it. Collisional forces with the atmosphere cause the ionospheric plasma to rotate with the Earth as well, generating a **v x B** electric field that is everywhere radially outward and which, in the absence of other forces, would set all of the plasma in the magnetosphere into corotational motion with the Earth. A modification to the corotational electric field occurs because of neutral winds in the upper atmosphere, which respond to temperature and pressure gradients caused by inputs such as sunlight, joule heating by currents associated with the aurora, and precipitation of the charged particles that produce the aurora.

By far the strongest electric fields, and the most important ones for magnetospheric dynamics, are produced by the interaction of the solar wind with the magnetosphere, which under normal conditions imposes a potential difference of some 50 to 100 kV across the magnetosphere in a generally dawn-to-dusk direction. This electric field produces sunward plasma convection in the equatorial plane. The interplay between corotation and sunward convection leads to the formation of a boundary within which the convection paths close about the Earth (red region in **Figure 2**) [*Grebowsky*, 1970]. All of the cold plasma, which

originates in the ionosphere, must follow these paths and is trapped in a region known as the plasmasphere. In the vicinity of the outer boundary of the closed convection paths a steep gradient of cold plasma density is typically observed. This plasma gradient is known as the plasmapause.

Since the potential difference in the solar wind over the cross-sectional scale size of the magnetosphere is normally about 250 kV, there must be a fairly efficient mechanism for coupling the solar-wind electric field into the magnetosphere. On the other hand, the injection of solar-wind plasma into the magnetosphere is somewhat less efficient, amounting to only 1 or 2% of the impingent flux primarily because the entry points are highly localized. As a result, the ionosphere competes favorably with the solar wind in populating the magnetosphere with plasma, although the relative fractions will always be difficult to determine because of the presence of large amounts of relatively low energy H^+ ions in both source populations.

It has been estimated that roughly 20% of the electric field from the solar-wind interaction results from a “viscous” interaction of the heated solar wind plasma that has traversed the upstream bow shock and that flows around the magnetosphere in a magnetosheath [*Boyle et al.,* 1997]. The phenomena that lead to this viscous interaction have not been identified. The candidates generally involve either anomalous transport of magnetosheath plasma across the boundary of the magnetosphere (the magnetopause) or MHD instabilities (such as the Kelvin-Helmholtz instability) caused by the high-velocity flow of magnetosheath plasma along the magnetopause.

The process responsible for the other 80% of the electric field is, however, known to be the direct interconnection between geomagnetic and interplanetary fields [*Burch*, 1974; *Vasyliunas*, 1974]. The interconnection results from the process of magnetic merging (also called magnetic reconnection), which occurs

at various locations on the dayside magnetosphere depending upon the direction of the interplanetary magnetic field (IMF). In general, northward-directed IMF leads to reconnection at high latitudes, while southward IMF produces reconnection sites at lower latitudes.

Although reconnection occurs with all directions of the IMF, southward IMF components lead to the transfer of magnetic flux from closed field lines on the day side to open field lines on the night side and thus to the build-up of magnetic stress in the geomagnetic tail. When this stress is later relieved, strong magnetospheric disturbances result [*Akasofu,* 1977; *Baker et al*., 1996]. Northward IMF, on the other hand, leads only to a stirring of magnetic field lines within the polar caps and little energy transfer to the inner magnetosphere [*Reiff and Burch*, 1985], although *Terasawa et al*. [1997] have shown that the near-Earth plasma sheet, while colder, is significantly more dense under this condition. Terasawa et al. conclude that the solar-wind plasma has better access through the flanks of the magnetosphere during northward IMF periods.

In addition to the efficient acceleration and injection of solar-wind plasma onto open magnetospheric field lines (those with one end on the Earth and the other end in the solar wind), reconnection sets up a large-scale system of magnetic-field-aligned currents that flow into, across, and then out of the ionosphere. These currents are known as the Region-1 Birkeland currents. As these currents flow through the resistive ionosphere, they produce electric fields which map along magnetic field lines into the magnetosphere, thereby setting up a global-scale system of plasma convection as first suggested by *Gold* [1959]. The circulation of plasma is generally away from the Sun in the outer magnetosphere and toward the Sun in the inner magnetosphere [*Axford*, 1969].

Since its discovery in 1958 by the detection of magnetically trapped radiation surrounding the Earth [*Van Allen et al.*, 1958], the magnetosphere has been

studied intensely with numerous satellite missions and a worldwide community of magnetospheric physicists. One of the most significant results has been the identification of cross-scale or hierarchical coupling by which small-scale processes like magnetic reconnection drive large-scale and even global-scale phenomena such as magnetospheric convection and the aurora. However, for many years the field was hampered by the lack of a large-scale observing capability. With the launch of the Dynamics Explorer mission in 1981, global images of the aurora on time scales of several minutes began to be available [*Frank et al.*, 1982]. Following the success of Dynamics Explorer, auroral imagers have been flown on several other spacecraft, including Viking, Polar, and most recently, IMAGE. Auroral imaging has helped tremendously in situating the local plasma and field measurements of magnetospheric satellites within the global environment because they map the location of electron precipitation from the entire magnetosphere into the upper atmosphere. What was needed next was the ability to image the plasmas of the magnetosphere, preferably with the identification of different species and energy ranges.

Theoretical models, background signals in charged particle detectors, and measurements of ultraviolet light from sounding rockets and low-altitude satellites gave convincing evidence that the imaging of magnetospheric plasmas was feasible. A comprehensive review of that evidence and an assessment of the promise of magnetospheric imaging has been provided by *Williams et al.* [1992]. The bases for plasma imaging are the resonant scattering of ultraviolet sunlight and the chemical reaction known as charge exchange.

Ultraviolet radiation from the Sun is resonantly absorbed by atoms and ions surrounding the Earth and later re-emitted omnidirectionally, producing a glow, which can be imaged. The most important emissions for magnetospheric imaging are the Lyman-alpha lines of neutral hydrogen (H I) at 121.6 nm, and of singly-

ionized helium (He II) at 30.4 nm, both of which are produced primarily in the solar chromosphere and at the base of the solar corona. Imaging of EUV radiation at 30.4 nm can provide direct detection of helium ions, which make up a variable ~10-15% fraction of the plasmasphere. The rest of the plasmasphere is almost entirely H^+, which has no optical emissions. On average, each helium ion of the plasmasphere resonantly absorbs and then re-emits a 30.4-nm photon about once every three hours, which is sufficient for the formation of global plasmasphere images on a several-minute time scale. Beginning in 1968 there were several instances of the detection of the He II resonance-line emission from low altitudes [e. g., *Young et al*., 1968; *Weller and Meier*, 1974; *Chakrabarti et al.*, 1982]. These early observations and models of expected results from high-altitude imaging are comprehensively reviewed by *Meier* [1991].

More recently, *Nakamura et al*. [2000] reported the first EUV images taken from outside the plasmasphere. The images were formed by scanning the plasmasphere with an EUV telescope using the spin and the orbital motion of the Planet-B spacecraft while it was in a parking orbit around the Earth before its transit to Mars. Even though each image required ~20 hours to accumulate, the observations established firmly the feasibility of global plasmasphere imaging.

The H I Lyman-α emissions have been used to obtain global images of the Earth's extended neutral hydrogen exosphere [e. g., *Carruthers et al*., 1976]. The exosphere provides a significant charge-exchange medium for ions out to distances near 15 R_E. Resonant charge-exchange reactions, e. g., H^+ (fast) + H (slow) $\rightarrow$ H (fast) + H^+ (slow); and accidental charge-exchange reactions, e. g., O^+ (fast) + H (slow) $\rightarrow$ O (fast) + H^+ (slow), between energetic ions and cold exospheric hydrogen atoms produce energetic neutral atoms (ENA), which are not affected by the magnetic field and so can be imaged remotely as a few-% tracer of magnetospheric ion populations. At lower altitudes near the exobase

(~500 km), O, He, and N_2 are also important sources of electrons for charge-exchange reactions [*Roelof and Skinner*, 2000].

The energetic neutral atoms that are produced by charge exchange can be imaged using two methods: (1) imaging of radiation emitted by those atoms that are formed in excited states, and (2) direct imaging with an ENA camera. Analyses of expected signals and backgrounds show that method (1) is limited to the imaging of doppler-shifted Lyman-α radiation from precipitating energetic hydrogen atoms [*Mende et al*., 2000]. Method (2) can be applied to ENAs (primarily H and O) over a very wide energy range (eV to MeV), although different techniques are required for various energy bands [*Moore et al*., 2000; *Pollock et al.*, 2000; *Mitchell et al.*, 2000].

Prior to the launch of IMAGE, ENA imaging was performed from low-altitude Earth orbit by the Astrid-1 satellite [*Brandt et al*., 1999]. At higher altitudes with the Polar satellite, *Henderson et al*. [1997] and *Jorgensen et al.* [2000] used data from an energetic ion dectector in regions devoid of energetic ions to form neutral atom images from a perspective far above the polar cap. These early results showed clearly the enormous potential of ENA imaging for probing the large-scale dynamics of the magnetosphere.

Finally, radio sounding, which has been used for many years to probe the structure of the bottomside ionosphere from the ground and the topside ionosphere from low-altitude satellites, can be used to map out the total plasma density throughout the magnetosphere as long as the ray paths traverse positive plasma density gradients. Within such a gradient, as the plasma frequency ($9 \bullet n^{1/2}$ kHz) rises toward the frequency of the transmitted electromagnetic wave, the wave will begin to be refracted and finally will be reflected back toward the transmitter. By suitable direction-finding and timing techniques, the direction and distance to the reflection point, as well as the total plasma density at that point,

can be determined. Under certain conditions the transmitted waves will travel within magnetic field-aligned density ducts instead of in straight lines. When these two modes are sorted out, the technique yields additional information about the distribution of plasma along magnetic field lines and, for example, the associated phenomenon of plasmasphere refilling. One of the most interesting potential applications of radio sounding is the mapping of changes in the location and structure of the magnetopause.

All of these imaging techniques are implemented together by instruments on the IMAGE satellite [*Burch*, 2000, 2003]. The results to date have led to the discovery of new phenomena such as plasmaspheric “shoulders” and “notches”, subauroral proton auroral arcs, and the sub-corotation of the plasmasphere. They have also provided confirmation of some longstanding predictions, such as plasmaspheric plumes; injection of the ring current in the midnight-to-dawn sector rather than the midnight-to-dusk sector, as commonly believed; and continuous magnetic reconnection at the dayside magnetopause. None of these predictions could have been adequately tested without global imaging of magnetospheric plasmas. Finally, magnetospheric imaging has led to the identification of source regions or causes of phenomena such as plasmaspheric shoulders (south-north transitions of the IMF), kilometric continuum radiation (generated within plasmaspheric notches), and skewed convection electric fields in the inner magnetosphere (caused by IMF B_y variations). The possibility of remote sounding of the position and structure of the magnetopause has been verified, but the techniques used so far have not yet been able to provide this type of mapping on a continuous basis.

The following sections summarize several of the new discoveries that have been made and mysteries that have been solved by magnetospheric imaging.

Also discussed are future directions in magnetospheric imaging at the Earth and at other planets.

2. ENA IMAGING SHEDS NEW LIGHT ON RING CURRENT INJECTION

One of the longest-standing challenges in magnetospheric physics has been understanding the physics of magnetic storms. Magnetic storms are caused by relatively dense, high-velocity solar-wind streams that impose long periods of strong southward IMF on the magnetosphere [*Chen*, 1997]. During the maximum epoch of the solar cycle, large magnetic storms are most often caused by coronal mass ejections (CMEs) from the Sun. CMEs are large magnetic clouds of plasma that can propagate at high speeds relative to the solar wind. During the declining phase of the solar cycle, magnetic storms still occur, but they are more often associated with corotating interaction regions (CIRs). CIRs are produced by high-speed solar-wind streams that emanate from cool, open-field-line regions in the solar corona that are known as coronal holes [*Sheeley et al.*, 1976]. The high-speed streams corotate with the Sun and overtake the lower-speed solar wind, producing interplanetary shock waves. When these reach the Earth, their effect is similar but generally less energetic than that associated with CMEs. Nonetheless, the most important factor in both cases is the direction of the embedded IMF, which when southward leads to magnetic storms but when northward results in only a short-lived compression produced by the shock wave but relatively little magnetospheric activity.

When CMEs or CIRs reach the Earth, the associated shock waves compress the magnetosphere impulsively, causing an increase of the magnetic field that is observed by surface magnetometers. This compression is known as a storm sudden commencement (SSC) or a sudden impulse (SI), depending on whether or not a magnetic storm is initiated. Over the next several hours, provided the IMF continues to have a southward component, a number of magnetospheric substorms occur, each one injecting plasma from the plasma sheet toward the inner magnetosphere. This time period of increasing energy input to the inner

magnetosphere is known as the magnetic storm main phase, during which the newly-injected particles begin to encircle the Earth, producing a “partial ring current.” During the main phase, the dayside magnetopause generally moves inward from its usual location at ~10 Earth radii to 6-8 Earth radii. As the storm recovers over the next few days, the magnetopause moves back outward and the ring current completely encircles the Earth (producing the “symmetric ring current”).

In the simplest terms, plasma-sheet ions and electrons are convected toward the Earth by convection electric fields (perpendicular to **B**), which affect them both equally. As they reach the stronger magnetic-field regions nearer the Earth, magnetic drifts, caused by the curvature of magnetic field lines and gradients in the magnetic field experienced by particles in their cyclotron motion, become more important [*Northrop and Teller*, 1960]. Magnetic drifts are westward for positive ions and eastward for electrons. Corotation competes with the magnetic drifts close to the Earth, causing the lowest energy positive ions also to drift eastward along with the electrons. In addition to the drift currents, another contribution to the current comes from plasma pressure gradients, which cause net currents to be produced by the gyration of ions in the magnetic field, as explained by *Hoffman and Bracken* [1965]. A general relationship for the currents attributable to these various sources was derived by *Parker* [1957]. *Dessler and Parker* [1959] and *Sckopke* [1966] later showed that the intensity of a magnetic storm as measured by the Dst index is proportional to the total particle energy density within the ring current. While both ions and electrons contribute to the ring current, ions with energies between ~10 keV and 100 keV make by far the largest contribution because of their much greater energy density [*Baumjohann*, 1993]. In addition to inward transport of plasma from the plasma sheet, direct injection of ions from the ionosphere is also an important source of the ring

current [*Gazey et al*., 1996]. A comprehensive review of the physics of the ring current and the results of in situ satellite ring-current measurements has been published by *Daglis et al*., [1999].

Just as important as the sources of the ring current are the various processes by which it is lost. A major loss process, particularly during the main phase of storms when the dayside magnetosphere shrinks markedly in size, is particle drift through the dayside magnetopause, causing loss of particles to the solar wind [*Liemohn et al*., 2001]. Charge exchange with the hydrogen atoms of the Earth's exosphere is another important loss process, which has been modeled quantitatively [e. g., *Fok et al.*, 1995]. Fok et al. also modeled the loss of ions by coulomb collisions with particles in the plasmasphere. A potentially important, but more difficult to assess, loss process is wave-particle interactions, which cause the precipitation of ions into the atmosphere [*Kozyra et al*., 1997; *Thorne and Horne,* 1997]. Even though the theory of wave-particle interactions, particularly those between ring-current ions and electromagnetic ion cyclotron (EMIC) waves, is well-developed, estimates of their importance are still limited to the residuals left over after the other processes have been quantitatively applied to satellite data. Wave-particle interactions are, therefore, a secondary but still potentially important ring-current loss process, as pointed out in the global simulations of *Jordanova et al*. [1997, 1998].

For many years the main-phase ring current has been called the asymmetric (or partial) ring current, while the recovery-phase current has been called the symmetric ring current. During the main phase the decrease of the horizontal component (H) of the geomagnetic field at low latitudes on the Earth's surface exhibits a systematic local-time dependence. The decrease is largest in the midnight-to-dusk sector with a maximum that gradually moves from ~22 MLT early in the main phase to ~18 MLT as the storm develops [*Akasofu and*

Chapman, 1967; *Fukushima and Kamide*, 1973; *Harel et al.*, 1981]. The belief had always been, therefore, that the build-up of the ring current during the main phase first occurs in the midnight-to-dusk sector. However, *Harel et al*. [1981], using the first comprehensive computer simulation of the behavior of the Earth's inner magnetosphere during a substorm-type event, concluded that "the observed asymmetry in the change of the horizontal magnetic field at low-latitude ground stations during the main phase of a magnetic storm should not be interpreted simply as asymmetric development of the inner-magnetospheric ring current and the associated region 2 Birkeland currents. Region 1 Birkeland currents, which connect to the outer magnetosphere, play a major role in the asymmetry of low-latitude ΔH…." The computer simulations of *Harel et al*. [1981] showed a partial ring current centered at midnight--a result that was basically ignored for the next 20 years.

Figure 3 (from *Harel et al*. [1981]) is a schematic diagram for the basic magnetospheric-convection current system. The region-1 currents (R1 in **Figure 3**) are generated by the interaction of the solar wind with the magnetosphere and are the driving currents for magnetospheric convection. The region-2 currents (R2) drive the return flow, which is sunward in the inner magnetosphere. During magnetic storms R2 currents close in the magnetosphere through the partial ring current (PRC), while during quiet times R2 currents close through the quiet-time ring current. The R2 currents provide a shielding effect that prevents the strong outer-magnetospheric convection electric fields from penetrating very far into the inner magnetosphere. A local breakdown of this shielding is responsible for allowing the injection of the storm-time ring current, as was directly observed by *Wygant et al*. [1998].

The magnetic perturbation measured at the surface of the Earth, which is expressed by the Dst (disturbance storm time) index, is produced by several

different current systems, including PRC, R1, R2, horizontal ionospheric currents, induced currents beneath the Earth's surface, magnetic tail currents, and magnetopause currents. The results of *Harel et al*. [1981] are consistent with Dst enhancements during the main phase of magnetic storms being caused primarily by a net R1 + R2 current system that is toward the Earth near noon and away from the Earth near midnight and not with the generally accepted effects of a dusk-centered partial ring current.

An example of a recent result which attributes Dst to a dusk-centered PRC is the study by *Liemohn et al*. [2001], who used the *McIlwain* [1986] electric field model to solve the kinetic equation of magnetospheric particle motion. **Figure 4** shows the particle-tracing results for three magnetic storms in 1997 and 1998. In each case a dusk-centered partial ring current formed during the early phases of the storm and evolved into a symmetric ring current during the recovery phase. During the main phase of the storms there is a pronounced minimum of energy density in the midnight-to-dawn sector (columns (a) and (b) of **Figure 4)**. *Liemohn et al*. [2001] showed that fully 80% of the Dst disturbances for these storms could be explained by the dusk-centered PRCs produced by the model.

Analysis of ring-current images obtained routinely by the IMAGE satellite has yielded consistently the puzzling result that the partial ring current does not appear in the dusk sector of the magnetosphere but in the midnight-to-dawn sector [*Brandt et al.*, 2002, 2004; *Fok et al*., 2003]. An example of this result is shown in **Figure 5**, which displays data from a magnetic storm on August 12, 2000. The top panel of **Figure 5** is a plot of the magnetic storm index Dst, along with the SYMH and ASYH indices for August 12. Dst is derived from the horizontal component of the average disturbance magnetic field at four lower-latitude (21°-33° magnetic) observatories spaced around the Earth. SYMH is similar in that it contains the average horizontal disturbance field for 12 low- and

mid-latitude (10°-50° magnetic) observatories, while ASYH measures the largest difference disturbance field among the 12 observatories. ASYH is believed to respond mostly to polar-region auroral disturbances.

The Dst and SYMH traces in **Figure 5** show the classic development of a strong geomagnetic storm with a main-phase decrease (minimum Dst = -235 nT) occurring between 03 and 09 UT, followed by a recovery phase lasting at least throughout the rest of the day. The classical computations of drift physics would predict a dusk-centered partial ring current during the main phase of this storm; however, as seen in the second and third panels of **Figure 5**, the PRC ion fluxes peak strongly in the midnight-to-dawn sector. The second panel displays equatorial ion fluxes obtained by deconvolution of the ENA images from the IMAGE HENA instrument that are plotted in the bottom panel of the figure [*Fok et al*., 2003].

As shown in **Figure 6**, *Fok et al.* [2003] were able to reproduce the post-midnight PRC using the self-consistent CRCM code—a combination of the Rice Convection Model [*Harel et al*., 1981], which serves as a convection electric field solver, and the Fok Ring Current Model [*Fok and Moore*, 1997], which traces particles. On the other hand, Fok et al. showed that the Weimer electric field model [*Weimer*, 1995], like the McIlwain model used by *Liemohn et al*. [2001], produced a pre-midnight PRC. Both the Weimer and the McIlwain electric field models are empirical models. The Weimer model is based on ionospheric electric field data, which is sorted by IMF direction and dipole tilt angle. The McIlwain model is based on plasma data obtained at geosynchronous orbit and is sorted by Kp (three-hour-average geomagnetic activity index).

Figure 6 plots simulated equatorial H^+ flux along with simulated ENA images from perspectives similar to those in **Figure 5** for two times (8 UT and 11 UT) during the August 12, 2000 magnetic storm for both the Weimer electric field

model and the CRCM electric field model. For the main phase of the storm (at 8 UT), the CRCM model produces a PRC extending across the night side with maximum fluxes in the early morning sector, while the Weimer model produces a dusk-hemisphere PRC with peak fluxes in the premidnight hours. **Figure 7** shows plots of electric equipotential contours (left-hand panels) and drift paths of equatorially-mirroring ions (right-hand panels) for both the Weimer and the CRCM electric-field models. The strong skewing of the CRCM equipotentials toward the morning sector is clearly responsible for the concentration of the PRC in that sector, while the strong electric fields extending inward to ~L=2 are consistent with the satellite electric-field measurements reported by *Wygant et al.* [1998]. Neither of these features is present in the Weimer model. However, it is not clear why the self-consistent (in electric field) CRCM model reproduces these observed features. Regarding the skewed electric field, *Fok et al*. [2003] suggested that the skewing may result from R2-current shielding effects or from ionospheric conductance gradients around the terminator.

A clue to the origin of the skewed electric potentials has been obtained by *Brandt et al*. [2002], who found a tendency for the ion injections to move from midnight toward the dawn meridian as IMF B_y became more positive and as the solar-wind velocity increased. Although B_y variations produce distortions in the ionospheric potential distributions presented by *Weimer* [1995], they apparently do not produce the post-midnight ion injections, as shown in **Figure 6**.

Although total closure between magnetospheric convection and ring current injection models with the ring current imaging data has not yet been achieved, it is very clear that without ring-current imaging the true distribution of the partial ring current might never have been appreciated.

3. EUV IMAGING REVEALS DETAILS OF PLASMASPHERE STRUCTURE

Cold plasma from the ionosphere flows outward along magnetic field lines, forming a roughly donut-shaped plasmasphere that encircles the Earth. During magnetic storms, the electric field induced by the solar wind becomes stronger, penetrating into the plasmasphere. Instead of continuing to drift around the Earth, plasmas in these outer shells are then drawn out of the plasmasphere. Modeling of this process over thirty years ago suggested that plasmaspheric erosion results in a tail or plume of cold plasma in the local afternoon extending from the plasmasphere outward to the dayside magnetopause [*Grebowsky*, 1970]. Although in-situ satellite measurements of plasma densities in the equatorial plane and at high latitudes showed localized density enhancements outside the plasmapause, it was not clear whether they were part of a plasma plume, or instead were isolated islands of plasma or “detached plasma regions” as described by *Chappell et al*. [1971].

With IMAGE we have begun to assemble a global description of plasmaspheric structure, its motion, and the physical processes that dominate its behavior. As noted before, extreme ultraviolet (EUV) light from the Sun is absorbed and re-emitted by helium ions, rendering the plasmasphere luminous in 30.4 nm light. The EUV instrument on IMAGE [*Sandel et al*., 2000] is able to detect light at this wavelength and return global images of the plasmasphere every 10 minutes, making it possible to identify and follow the pattern of plasmaspheric ebb and flow throughout the inner magnetosphere.

One of the early results of IMAGE was to establish without any doubt the existence of the plasma plumes some thirty years after their prediction [*Burch et al*., 2001a; *Sandel et al.*, 2001]. **Figure 8** shows a particularly striking example of a plasma plume observed during the recovery phase of a modest magnetic storm

on August 11, 2000. The IMAGE plume observations do not rule out the possibility that detached plasma regions also exist, but if they do, they are below the limit of detectability of the IMAGE-EUV instrument, which is equivalent to a total plasma density of approximately 40 cm^{-3} (He^{+} density of 5-8 cm^{-3}) [*Goldstein et al., 2003a*] or they exist beyond the FOV of the IMAGE-EUV camera, which at apogee extends to a geocentric distance of 8 R_E.

Important confirmation of the existence of plasma plumes has been provided by in-situ plasma measurements from the LANL geosynchronous satellites as they cross the plumes during the acquisition of images by IMAGE-EUV. **Figure 9**, taken from *Goldstein et al*. [2004a], shows data from two LANL satellites (L1 and L9) on June 26, 2000. The EUV image in **Figure 9** was obtained just as L1 had finished crossing the plume. Both L1 and L9 observed enhanced structured plasma densities in the plume region and also measured sunward plasma flows within the plume in the range 10 to 25 km/s. These measurements provide independent evidence that, as predicted theoretically by *Grebowsky* [1970], plasma flows outward through the plumes toward the magnetopause.

In addition to the predicted plasma plumes, other features are routinely observed in the IMAGE EUV images. Several of these features are noted in **Figure 10**. One of the most surprising is the shoulder [*Burch et al*., 2001a], which forms in the pre-dawn region and then rotates with the plasmasphere through the day side. *Goldstein et al*. [2002, 2003b] showed conclusively that shoulders can form when the IMF turns northward. They also identified the process that causes the shoulder to form. When the IMF is southward, magnetic reconnection produces strong convection and field-aligned currents in the magnetosphere. Near the plasmapause, the field-aligned currents act to shield the innermost magnetosphere from the convection electric field. Numerical modeling using the Rice Convection Model (RCM) showed that when the IMF suddenly turns

northward, the shielding effect, which is no longer needed, persists for some time as a kind of hysteresis or flywheel effect. This residual shielding (or overshielding) produces a localized reverse eddy flow that produces the shoulder feature [*Goldstein et al*., 2002].

Goldstein et al. [2003c] have made certain refinements to the model of *Grebowsky* [1970] in light of ionospheric and magnetospheric convection measurements that have been obtained in the interim. The most significant new convection feature is the intense convection zone that forms on the night side equatorward of the auroral oval during magnetospheric substorms and especially during their recovery phases. These strong convection zones were first pointed out by *Gurnett and Frank* [1973]; their development during substorms was identified by *Burch et al*. [1976]. *Anderson et al*. [1991] gave them the name Subauroral Ion Drifts (SAID) and noted their relationship to heavy-ion density enhancements in the midlatitude ion trough as noted earlier by *Burch* [1973a]. After *Yeh et al*. [1991] identified a more widespread convection enhancement in the same general region during magnetic storms, *Foster and Vo* [2002] studied both phenomena using radar data and proposed the composite name Subauroral Polarization Stream (SAPS).

Goldstein et al. [2003c] compare IMAGE-EUV images during a magnetic storm to the results of two convection electric-field models for the inner magnetosphere. The first is a model derived independently from different considerations by *Volland* [1973] and *Stern* [1975] and is basically a combination of the corotation electric field and a dawn-dusk electric field imposed on the magnetosphere by its interaction with the solar wind. The Volland-Stern model was refined by satellite measurements of high-latitude electric fields and, in the case of *Volland* [1973], by ground-based measurements of plasmapause positions. The second model involves the addition of an ad-hoc SAPS electric

field distribution to the Volland-Stern model. The ad-hoc SAPS model is based on the statistical properties of SAPS that are presented by *Foster and Vo* [2002].

The results of *Goldstein et al. [2003c]* are presented in **Figures 11** and **12**, which show four EUV images acquired during a magnetic storm on June 2, 2001. Each figure also shows white curves, which are the loci of strong plasma density gradients typical of the plasmapause and the boundaries of plasma tails. The white curves in **Figure 11** were derived from the Volland-Stern electric-field model, while those in **Figure 12** used the Volland-Stern model with the addition of the ad hoc SAPS model. While both models show excellent agreement with the dawn-hemisphere plasmapause, **Figure 12** shows better agreement than **Figure 11** in the dusk hemisphere, especially in panels (c) and (d) when the plasma tail begins to wrap around the plasmasphere as is typical for the late development of the tails. Addition of subcorotation at the observed 80-90% rate [**Section 4**] is found to further improve, although only slightly, the agreement between the models and the data [J. Goldstein, private communication].

Noted in **Figure 10** and seen clearly in **Figures 11** and **12** are channels that both form between the main plasmasphere and the plume [*Sandel et al.*, 2003]. *Spasojevic et al.* [2003] have shown that these channels appear as convection begins to subside following a strong erosion event during which a plume has formed. During such periods, the base of the plume begins to corotate with the Earth while its outer reaches remain nearly fixed in magnetic local time. This pattern leads to a wrapping of the plume about the plasmasphere and the formation of a low-density channel. **Figure 13** [adapted from *Sandel et al*., 2003] clearly shows the channel development for an event during which two plumes form and coexist as the convection increases, ebbs, and then increases again in response to two periods of strong substorm activity separated by a quiet period [*Spasojevic et al*., 2003].

4. DISCOVERY OF PLASMASPHERE COROTATION LAG

One of the basic tenets of magnetospheric physics, which has been accepted without question for the past 40+ years is that the plasmasphere, and especially its central core, corotates with the Earth. With the advent of plasmaspheric imaging, it has been shown that the plasmaspheric rotation actually lags corotation by a variable amount, averaging about 10-15% [*Sandel et al*., 2003]. This result, which has far-reaching implications for magnetospheric convection theory, has been explained by *Burch et al*. [2004] as resulting from the latitude-dependent departure of the ionosphere from ideal corotation.

Sandel et al. [2003] used localized low-density regions (or notches) as markers to track the rotation of the plasmasphere. Such notches have been observed to persist for periods as long as 60 hours, during which time they can be seen for up to six hours of each 14-hour IMAGE orbit when the spacecraft is hovering near apogee. **Figure 14** shows data for the longest-lived notches seen to date. In the upper part of **Figure 14** are (a) an EUV image and (b) a plot showing the position of the plasmapause in L and magnetic longitude coordinates as scaled from the image. Two notches are present—one at about 7.5 hours MLT and the other at about 19.8 hours MLT. The bottom panel of **Figure 14** shows the magnetic longitude of the 7.5-hour MLT notch over its observed lifetime. The plot shows that the notch drifted westward (toward smaller longitude values), corresponding to an angular velocity that is nearly constant at about 90% of corotation. Moreover, this lag appeared roughly constant over the full range of MLT. While some notches showed variable lags during their lifetimes, the general result for 13 notches was that a rotation rate of 85% to 90% of the corotation rate was observed for radial distances of $2<L<4$ regardless of MLT.

As noted by *Hill* [1979], planetary plasma corotation is generally expected to break down when the corotation velocity exceeds the Alfvén speed. Mass loading by plasma flowing outward from the planetary ionosphere can move this point much closer in, e. g., to ~60 planetary radii in the case of Jupiter. Similar calculations for the Earth show the breakdown radius for the observed plasma outflow rates to lie far outside the plasmapause. In the Jovian magnetosphere, a variable corotation lag averaging about 5% has been observed for the Io plasma torus (at 6 Jovian radii) [*Brown*, 1994]. *Pontius and Hill* [1982] have shown that for this level of corotation lag local plasma production within the Io torus would be required, and *Brown* [1994] has estimated an ion production rate between 2000 and 3000 kg sec^{-1}, which is reasonable given the large volcanic and atmospheric gas source at Io. The IMAGE observations, which show a corotation lag at 2-3 Earth radii two to three times that in the Io plasma torus (even though there is no local gas source as there is at Io), therefore demanded a very different type of explanation.

To account for the corotation lag, *Burch et al*. [2004] hypothesized that mid-latitude ionospheric winds are directly resposible for the phenomenon. Mid-latitude westward winds (in the Earth's frame of reference) were predicted to result from the ionospheric disturbance dynamo [*Blanc and Richmond*, 1980], according to which heating of the ionosphere by auroral particles and currents causes an equatorial flow that, because of angular momentum conservation, is diverted westward (that is, by the coriolis force). The equatorward electric field associated with the westward flow drives a Pedersen current that results in the accumulation of charge in the equatorial region and an ambipolar electric field that is directed poleward. At low latitudes this polarization electric field can dominate, causing corotation, and sometimes even superrotation, to be established. *Heelis and Coley* [1992] showed that the predictions of the

ionospheric disturbance dynamo are confirmed by the ion drift meter data obtained by DMSP spacecraft.

Burch et al. [2004] analyzed DMSP ion drift data collected within an 80°-wide sector of magnetic longitude and between magnetic latitudes of 40° and 45°, within which a plasmaspheric notch identified by *Sandel et al*., [2003] rotated nearly, but not exactly, with the Earth. Over a two-day period, the motion of the notch agreed closely with that predicted by the ionospheric drift measurements. The derived rotation rate was 90 ± 1% of the corotation rate. While the observed corotation lag should not be surprising, in light of the previous results of *Blanc and Richmond* [1980] and *Heelis and Coley* [1992], it is considerably at odds with the usual assumption of strict corotation that has part of all magnetospheric convection models that have been in use for at least the past three decades. Moreover, it is clear that without global plasmaspheric imaging the corotation lag might never have been detected.

5. EUV IMAGING AND RADIO SOUNDING IDENTIFY SOURCE OF KILOMETRIC CONTINUUM RADIATION

In addition to their usefulness as tracers of plasmaspheric corotation, the notches in density that are observed in EUV images have been found to be the source regions for the often-observed but previously unexplained phenomenon known as kilometric continuum radiation.

Continuum radiation is observed over a very broad frequency range from as low as 5 kHz [*Gurnett*, 1975] to as high as 800 kHz [*Hashimoto et al*., 1999]. The highest frequency component of the continuum radiation from 100 to 800 kHz has been referred to as kilometric continuum [*Hashimoto et al*., 1999]. Hashimoto et al. also found that kilometric continuum was primarily observed when Geotail was at a magnetic latitude less than about 15^{o}. Prior to IMAGE, kilometric continuum was believed to be generated deep inside the plasmasphere, and the conditions under which it was generated were largely unknown [*Hashimoto et al*., 1999].

Panel A of **Figure 15** is a frequency versus time spectrogram from RPI passive measurements on April 8, 2001 during a time when IMAGE was moving nearly in the noon-midnight meridian through the dayside and nightside plasmasphere (see insert). The RPI instrument observes kilometric continuum radiation in a plasmaspheric density depression on the dayside as delineated by the difference between the model f_p (the plasma frequency) and the observed f_{uhr} (the upper hybrid resonance frequency). Observations of kilometric continuum in density depletions, like those shown in panel A, have also been observed by a number of other missions with wave instruments [e.g., *Carpenter, et al*., 2000].

When compared with measurements by the EUV instrument on IMAGE, these passive wave measurements by RPI have provided a new insight into the source region of kilometric continuum [*Green et al*., 2002]. Panel B of **Figure 15** is an image of the plasmasphere taken at 23:52 UT on April 7, 2001 by EUV. The direction to the Sun is in the upper left in this image. The distinct plasmaspheric notch (or bite-out) shown in panel B was observed for approximately 5 hours in successive EUV images and found to rotate with the plasmasphere as discussed in **Section 4**. The EUV instrument is routinely turned off during perigee passages of IMAGE below about L = 8 so was not imaging during the time of the RPI observations in panel A. However, the mapping of the IMAGE trajectory with respect to the corotating notch structure is shown in **Figure 15** panel C. From these results, *Green et al*. [2002] proposed that kilometric continuum would be generated at the newly established plasmapause deep within plasmaspheric notches. At this time it is not known how these newly discovered plasmaspheric notch structures are created.

In a follow-up study by *Green et al.* [2004], IMAGE and Geotail observations of kilometric continuum and EUV observations of the plasmasphere were combined to confirm these initial results. **Figure 16** shows a Geotail spectrogram of the narrow band kilometric continuum emissions (panel A) and its position relative to a simultaneously observed EUV notch structure (panel B). Geotail's position during these observations was within 10° of the magnetic equator at nearly 20 R_E. The plasmapause determined from EUV data including the notch structure, is shown in panel B at the same magnetic longitude as the Geotail observations of the kilometric continuum. Ray tracing calculations by *Green et al*. [2002], shown in the inset of panel B, illustrate that the kilometric continuum source region lying deep within the plasmaspheric notch provides a significant

propagation effect to the ray paths that will confine the kilometric continuum emission cone in longitude to approximately fill the notch structure.

The results from the RPI observations of kilometric radiation are summarized in the cartoon shown in **Figure 17**, which also illustrates the emission cone of auroral kilometric radiation. Since kilometric continuum is observed in the same frequency range as AKR, earlier surveys using instruments with poor frequency resolution could have easily mistaken kilometric continuum for AKR [see, for example, Figure 6 in *Green, et al*., 1977]. Unlike AKR, which is generated in the nightside auroral zone and beamed primarily tailward, kilometric continuum emissions are emitted into relatively flat emission cones in the magnetic equator that co-rotate with the plasmasphere over all local times or until the emission ceases.

6. REMOTE SOUNDING OF THE MAGNETOPAUSE DEMONSTRATED WITH RADIO SOUNDING

Among the promises of magnetospheric imaging were plans to map large-scale variations in the magnetopause, its wave structure, and its motion [*Green et al*., 2000]. While the Radio Plasma Imager (RPI) on IMAGE has shown that the magnetopause and its density gradient can on occasion be measured, a continuous mapping has not yet been achieved. Further refinement of the sounding techniques are, however, expected to improve the duty cycle of magnetopause measurements.

Figure 18 shows three RPI range-vs.-frequency plasmagrams during times when IMAGE was near 7 R_E radial distance, descending from apogee. Each plasmagram clearly shows echoes from the plasmapause (~5 R_E distant) and the magnetopause/boundary layer (~3 R_E distant). The time sequence of plasmagrams in **Figure 18** reveals a decreasing distance to the plasmapause and a corresponding increasing distance to the magnetopause.

The magnetopause boundary layer echoes always show a considerable amount of range (i. e., vertical) spreading indicating that plasma density irregularities are common in this region as has been reported by *Larson and Parks* [1992] and others. The diffuse nature of the boundary layer echoes in **Figure 18** are due to multiple direct reflections, while the rapid drop-off of the trace at high frequencies provides both the distance to the magnetopause and the maximum density there (as indicated by the plasma frequency). For this event, the plasma frequency at the magnetopause, assuming O-mode propagation, ranges from 60 to nearly 68 kHz corresponding to a density of ~45-55 cm^{-3}. The nearly horizontal nature of the magnetopause echoes in the plasmagrams indicates a very steep increase in density at the boundary layer starting at about ~18 cm^{-3} and quickly rising up to the magnetopause density. In addition, the 32 minutes covered by these observations indicate that the magnetopause boundary layer was relatively stable with its motion confined to within less than about 1 R_E.

7. CONTINUOUS RECONNECTION DETECTED WITH PROTON AURORA IMAGING

Magnetic reconnection is known to produce ~80% of the magnetospheric convection electric field and to be the driving process for magnetospheric substorms and magnetic storms. Although the importance of reconnection is well-accepted, little is known about its nature. Ground-based and satellite measurements of auroral forms, precipitating ions, and electric and magnetic fields have raised questions but provided few answers about reconnection. Is it localized or widespread? Is it continuous or sporadic? Does it occur only between oppositely-directed magnetic field lines (antiparallel reconnection) or also between field lines with oblique relative orientations that just have a component that is antiparallel (component reconnection)? The answers to these questions require continuous, global measurements of some phenomenon that provides a marker for reconnection.

Smith and Lockwood [1996] and *Fuselier et al.* [2002a] have reviewed much of the evidence that reconnection at the magnetopause is primarily responsible for the acceleration of solar-wind particles and their injection into the polar cusps. Before the IMAGE mission was launched it was recognized that the development of a capability to remotely sense the accelerated cusp particles would provide a nearly continuous monitor of reconnection and a determination of whether it is continuous, sporadic, or pulsating. Such a capability is provided by the doppler-shifted Lyman-α channel of the IMAGE-FUV spectrographic imager (SI-12) [*Mende et al*., 2000]. The SI-12 images energetic neutral hydrogen atoms that are moving downward into the atmosphere. There is an overwhelming glow of Lyman-α radiation at 121.6 nm (the geocorona) that is produced by the Earth's outermost atmosphere (the exosphere). In fact, the detectable geocorona extends outward to a distance of ~15 R_E [*Carruthers et al*., 1976; *Rairden et al*.,

1986]. The very weak (in comparison) emission of energetic hydrogen would be undetectable except for the slight Doppler red shift (to 121.8 nm for 2-3 keV hydrogen) [*Gérard et al*., 2000]. The SI-12 can separate these signals and image the precipitating hydrogen atoms.

As noted by *Fuselier et al*. [2003], for nominal solar-wind dynamic pressures (~1.5 nPa), the SI-12 is not able to detect the cusp proton aurora. However, when the dynamic pressure is above about five times nominal, the cusp aurora is observed; moreover, *Frey et al*., [2003a] showed that the cusp footpoint is continuously visible during extended periods of northward IMF and high solar wind ram pressure. The eight frames covering ~3.5 hours on March 18, 2002 shown in **Figure 19** [taken from *Frey et al.*, 2003a] indicate that magnetic reconnection at the magnetopause can be a very steady process. The cusp proton aurora spot can be seen in each image in **Figure 19** near the noon meridian at latitudes near 80°. It moves toward the afternoon whenever the IMF takes on an eastward component (e.g., at 15:58:56 and 16:20:47 as shown in the small green boxes in the upper left-hand corner of each image) and toward the morning when the IMF takes on a westward component (e.g., at 15:50:06 and 16:59:37). This correlation between the local time of reconnection and the east-west component of the IMF is precisely what is predicted by the antiparallel model of reconnection [*Crooker*, 1979].

The question of antiparallel versus component reconnection has been debated for many years, with the predictions of both being supported by various in-situ data sets. However, as in the case of continuous versus sporadic reconnection, definitive progress was limited by the lack of a continuous marker for reconnection. With the availability of cusp auroral spot images from SI-12, the occurrence of antiparallel reconnection has now been confirmed, and all of the predictions of this model [*Crooker*, 1979] have been verified [*Fuselier et al*.,

2002a; 2003]. Specifically, the predicted movement of the cusp footpoint with changes in IMF B_y and B_z, which was earler determined on a statistical basis by *Burch* [1973b] and *Newell et al*. [1989], has been observed for the first time with continuous observations. When B_z is positive (northward), there is a highly localized spot located poleward of the dayside auroral oval. As shown by *Fuselier et al*. [2003], magnetic field lines from the spot map to a narrow region on the magnetopause poleward of the cusp where magnetosheath field lines are draped along the magnetopause and are expected to be antiparallel to the magnetic field lines of the magnetosphere. The spot moves with IMF B_y and is located at magnetic local times before noon for negative B_y and after noon for positive B_y components. When the IMF turns southward (B_z<0), the cusp footpoint moves equatorward and spreads out along the auroral oval, maintaining the same local-time dependence in response to the IMF east-west component as for northward IMF [*Frey et al*., 2003b].

Phan et al. [2003] present direct observations by Cluster along the high-latitude magnetopause in a region that maps magnetically to a simultaneously observed proton auroral spot. The reconnection signatures observed by Cluster (plasma jets and magnetic field rotations) occurred in a high magnetic shear (~175°) region, which indicates that antiparallel reconnection was occurring. The size of the auroral spot suggested a reconnection line 3.6 R_E long in the dawn-dusk direction. However, Phan et al. note that the reconnection line may have been even longer, extending into a lower shear region in which weaker auroras, falling below the SI-12 threshold, may have been produced.

In spite of the dramatic confirmation of the antiparallel reconnection model provided by IMAGE, the tilted neutral line (component reconnection) model has not been ruled out by the observations. More work remains to be done to determine if and when component reconnection begins to operate.

7. SOLAR-WIND CONTROL OF IONOSPHERIC OUTFLOW ESTABLISHED WITH NEUTRAL ATOM IMAGING

The Low-Energy Neutral Atom (LENA) imager on the IMAGE satellite is designed to take two-minute snapshots of the lowest-energy range of ENAs that can be detected (10 eV to 500 eV). In this energy range, the most important signal within the magnetosphere was anticipated to be the outflowing ions from the ionosphere. While the classical polar wind [*Banks and Holzer*, 1968] is generally below this energy range, important outflow occurs at higher energies because of perpendicular heating by ion cyclotron or lower-hybrid waves (ion conics) and by field-aligned acceleration by auroral electric fields (ion beams) [*Cornwall*, 1986].

Copious amounts of ionospheric plasma are injected upward into the magnetosphere, causing the ionosphere to compete favorably with, and perhaps even to dominate, the solar wind as a source of magnetospheric plasma. Identified sources include the cusp ion fountain effect [*Moore,* 1984] and auroral ion beams [*Collin et al.,* 1981]; however, the global distribution of ion outlfow and its response to inputs such as solar-wind pressure pulses remained unknown because of the lack of a global imaging capability. Images from LENA have led to some progress in these areas, although the anisotropic nature of the upflowing ion pitch-angle distributins [*Peterson et al.*, 1992] has caused the effective field of view of the low-energy neutral-atom images to be dependent upon the spacecraft location, leading to partial, rather than truly global, views [*Fuselier et al.*, 2003].

Figure 20 [adapted from *Fuselier et al., 2003 and Burch*, 2003] shows six IMAGE-LENA images of ionospheric neutral-atom outflow along with solar-wind pressure data from the Geotail satellite on June 24, 2000. As shown by *Fuselier et al*. [2002b], the ion outflow occurs promptly in response to each of the three successive but fairly weak pressure pulses and subsides between them. If the

outflowing ion distributions were isotropic, then global images could be obtained from any location above the polar cap. However, the distributions are generally peaked either along the local magnetic field (ion beams) or at an intermediate angle (ion conics). In either case, the neutral atoms produced by charge exchange will be beamed along the direction of the parent ions, even though they are unaffected by the magnetic field. Thus, as the spacecraft moves in its orbit, the outflowing ion images appear to move against the backdrop of the Earth (as seen in **Figure 20**). Nonetheless, the timing of the outflow with respect to the solar-wind pressure pulses has established that the ion outflow is driven directly by the solar wind. Modeling performed by *Fuselier et al*. [2003] has shown further that the outflow is produced by the deposition of energy at high altitudes (several hundred to 1000 km) in regions containing intense auroral emissions.

8. SUMMARY AND CONCLUSIONS

Preparations for global imaging of magnetospheric plasmas extended over more than thirty years, during which theoretical models and low-altitude measurements from sounding rockets and satellites steadily built up a strong case both for the scientific value of magnetospheric imaging and for its feasibility. Much of the early work has been reviewed by *Williams et al*. [1992]. Fortunately, by the year 2000 a mission containing instruments for all of the imaging techniques that had been developed was ready for launch and operation [*Burch*, 2000]. IMAGE was deployed in an orbit suitable for obtaining global views of the inner magnetosphere and has a time resolution (~two minutes) appropriate for the study of magnetospheric disturbances. It was also fortunate that by this time the physics of the inner magnetosphere was well enough understood that specific tests of many hypotheses could be performed in ways not possible

without global imaging. Although several of these tests were anticipated before and during the development of the IMAGE mission, others were not foreseen, particularly those related to the direct response of inner magnetospheric phenomena to changes in the solar wind and interplanetary magnetic field. In some cases, phenomena that were considered to be well understood and not in need of further experimental tests were shown by global imaging to have behavior fundamentally different from the accepted description, leading to revolutionary changes in understanding.

An example of testable hypotheses addressed by IMAGE is the detection of long plasma tails extending toward the magnetopause in the duskside hemisphere. These tails had been predicted by *Grebowsky* [1970], and in-situ measurements from spacecraft such as OGO-5 [*Chappell et al.,* 1971] and LANL [*McComas et al.,* 1993] had shown clear evidence for “outlying” plasma populations beyond the plasmapause. But whether these features were islands of plasmas or segments of attached plasma tails was not known and could not be known until global plasmaspheric images were available.

Examples of previously unknown phenomena first detected by IMAGE are the various plasmaspheric structures such as shoulders [*Burch et al*., 2001a] and notches [*Green and Reinisch*, 2003]. A somewhat surprising aspect of the shoulder features is that, in spite of their location far inward from the magnetopause, they are produced directly by northward turnings of the IMF [*Goldstein et al*., 2002]. As shown by Goldstein et al., the shoulders are caused by reverse eddies in the pre-dawn region that are generated by the residual shielding of the convection electric field following the sudden weakening of convection when the IMF shifts from southward to northward. The plasmaspheric notches were shown by *Green et al*. [2002] to have added significance as the source regions for the well-known kilometric continuum radiation.

An example of imaging data that challenged previously accepted interpretations is the observation that ring-current injections occur in the midnight-to-pre-dawn sector rather than in the pre-midnight-to-dusk sector of the magnetosphere [*Brandt et al*., 2002]. With IMAGE it was further shown that the IMF controls the location of injection with stronger positive B_y components moving the injection location more toward the dawn meridian. This post-midnight injection was a surprising result because the ground magnetic signature of the partial ring current peaks in the dusk sector. However, *Harel et al*. [1981] had in fact essentially predicted this injection morphology with a global convection model and showed further that the main-phase magnetic signature was due to field-aligned currents flowing into the ionosphere on the dayside and out of the ionosphere on the night side rather than by a dusk-centered ring current. Nonetheless, this prediction was not widely accepted until the ring current images became available.

Another example of how global imaging has overturned conventional wisdom about the magnetosphere is the discovery that the plasmasphere does not corotate with the Earth as is assumed in all dynamic models of the magnetosphere. Using plasmasphere notches as markers, *Sandel et al*. [2003] showed that during relatively quiet times the rotation of the plasmasphere lags that of the Earth by some 10-15%. This lag occurs at all local times and so cannot be explained by the penetration of convection electric fields, which would cause a speed-up on the dawn side and a slow-down on the dusk side. *Burch et al*. [2004] showed that the corotation lag is matched by a quantitatively similar lag in the topside ionosphere in regions below the notches. These mid-latitude westward ionospheric winds (in the Earth's frame of reference) had been predicted much earlier in the context of an ionospheric disturbance dynamo effect [*Blanc and Richmond*, 1980] and confirmed with satellite data by *Heelis*

and Coley [1992]. Since the collisionless plasma of the plasmasphere must move with the magnetic field lines that map to the ionosphere, the plasmasphere corotation lag could have been specifically predicted but was not.

By combining images from the different instruments on IMAGE, multi-spectral views of the magnetosphere showing interactions among different plasma populations can be obtained [see *Burch et al*., 2001b]. **Figure 21** shows a sequence of composite images during a magnetic storm on April 17, 2002, which was investigated by *Goldstein et al*. [2004b, 2005]. In **Figure 21** the red-yellow-white pixels are mappings of FUV auroral pixels to the equatorial plane using the Tsyganenko 2001 magnetosphere model [*Tsyganenko*, 2002]. The blue-to-white pixels form IMAGE-HENA ring current images, and the green-to-white pixels are from the EUV instrument. On the Earth's disk, the EUV aurora can be seen.

Images such as those in **Figure 21** show clearly the dynamic juxtaposition and sometimes overlap of the hot and cold populations of the magnetospheric plasma. Of particular interest is the propagation of a plasmapause undulation [discovered by *Goldstein et al*., 2004b] through the dusk-to-afternoon sector and the overlap of the ring current with the plasma tail or "plume" closer to the noon meridian.

As more global imaging data are obtained with IMAGE and other spacecraft orbiting the Earth and other magnetized planets such as Mercury and Saturn, we can anticipate more surprises and more revolutionary changes in our understanding of the global dynamics of planetary magnetospheres. A neutral atom imager in the higher energy range (10 to 500 keV) is now obtaining data in the Saturn magnetosphere. On the way to Saturn, this camera obtained ENA images of the Jovian magnetosphere [*Mitchell et al*., 2004]. In the case of the Earth, the NASA TWINS mission will improve the ability to interpret images of

plasmas in the 1 to 50 keV energy range by obtaining a stereoscopic view. Multiple views are extremely important for the interpretation of images of optically thin media such as magnetospheric plasma populations.

It is fair to say that the reality of magnetospheric imaging, even with the first space mission dedicated to it, far exceeds its promise. While it is obvious that being able to “see” the Earth’s space environment for the first time is exciting both for scientists and the general public, IMAGE has shown that the dynamical and multi-spectral imaging capability that it provides are more importantly leading to revolutionary advances in our understanding of the global physics of the magnetosphere.

ACKNOWLEDGMENTS. I would like to thank Drs. R. A. Hoffman, W. S. Lewis, D. Hassler, and J. Goldstein, for very helpful discussions. This work was supported by NASA Contract NAS5-96020 with the Southwest Research Institute.

REFERENCES

Akasofu, S.-I. *Physics of Magnetospheric Substorms*, D. Reidel, Dordrecht, 1977.

Akasofu, S.-I., and S. Chapman, A systematic shift of the DS axis, *Planet. Space Sci., 15*, 937, 1967.

Anderson, P. C., R. A. Heelis, and W. B. Hanson, The ionospheric signatures of rapid subauroral ion drifts, *J. Geophys. Res., 96*, 5785-5792, 1991.

Axford, W. I., Magnetospheric convection, *Rev. Geophys., 7*, 421-459, 1969.

Baker, D. N., T. I. Pulkkinen, V. Angelopoulos, W. Baumjohann, and R. L. McPherron, Neutral line model of substorms: Past results and present view, *J. Geophys. Res., 101*, 12,975-13,010, 1996.

Banks, P. M., and T. E. Holzer, The polar wind, J. Geophys. Res., 73, 6846-6854, 1968.

Baumjohann, W., The near-Earth plasma sheet: an AMPTE/IRM perspective, *Space Sci. Rev., 64*, 141-163, 1993.

Blanc, M., and A. D. Richmond, The ionospheric disturbance dynamo, *J. Geophys. Res*., 1980.

Boyle, C. B., P. H. Reiff, and M. R. Hairston, Empirical polar cap potentials, *J. Geophys. Res., 102*, 111-125, 1997.

Brandt, P. C., S. Barabash, O. Norberg, R. Lundin, E. C. Roelof, and C. J. Chase, Energetic neutral atom imaging at low altitudes from the Swedish

microsatellite Astrid: Images and spectral analysis, *J. Geophys. Res., 104*, 2367-2379,1999.

Brandt, P. C., S. Ohtani, D. G. Mitchell, M.-C. Fok, E. C. Roelof, and R. Demajistre, Global ENA observations of the storm mainphase ring current: Implications for skewed electric fields in the inner magnetosphere, *Geophys. Res. Lett., 29*(20), 10.1029/2002GL015160, 2002.

Brandt, P. C., D. G. Mitchell, R. Demajistre, E. C. Roelof, S. Ohtani, J.-M. Jahn, C. Pollock, G. Reeves, Storm-substorm relationship during the 4 October, 2000 storm. IMAGE global ENA imaging results, in *Disturbances in Geospace: The Storm-Substorm Relationship*, edited by *A. Surjalal Sharma, Yohsuke Kamide, and Gurbax S. Lakhina*, Geophysical Monograph No. 142, p. 103-118, doi:10.1029/142GM10, 2004.

Brown, M. E., Observation of mass loading in the Io plasma torus, *Geophys. Res. Lett., 21*, 847-850, 1994.

Burch, J. L., High-latitude proton precipitation and light-ion density profiles during the magnetic storm initial phase, *J. Geophys. Res., 78*, 6569-6578, 1973a.

Burch, J. L., Rate of erosion of dayside magnetic flux based on a quantitative study of the dependence of polar cusp latitude on the interplanetary magnetic field, *Radio Sci., 8*, 955-961, 1973b.

Burch, J. L., Observations of interactions between interplanetary and geomagnetic fields, *Rev. Geophys. Space Phys., 12*, 363-378, 1974.

Burch, J. L., S. A. Fields, and R. A. Heelis, Substorm effects observed in the auroral plasma, in *Physics of Solar Planetary Environments*, Edited by D. J. Williams, p. 740-759, American Geophysical Union, 1976.

Burch, J. L., IMAGE mission overview, *Space Sci. Rev.*, *91*, 1-14, 2000.

Burch, J. L., S. B. Mende, D. G. Mitchell, T. E. Moore, C. J. Pollock, B. W. Reinisch, B. R. Sandel, S. A. Fuselier, D. L. Gallagher, J. L. Green, J. D.

Perez, and P. H,. Reiff, Views of Earth's magnetosphere with the IMAGE satellite, *Science*, *291*, 619-624, 2001a.

Burch, J. L., D. G. Mitchell, B. R. Sandel, P. C. Brandt, and M. Wuest, Global dynamics of the plasmasphere and ring current during magnetic storms, *Geophys. Res. Lett., 28*, 1159-1162, 2001b.

Burch, J. L., The first two years of IMAGE, *Space Sci. Rev.*, *94*, 1-24, 2003.

Burch, J. L., J. Goldstein, and B. R. Sandel, Cause of plasmasphere corotation lag, *Geophys. Res. Lett*., *31*(5), doi: 10.1029/2003GL019164, 2004.

Carpenter, D. L., R. R. Anderson, W. Calvert, and M. B. Moldwin, CRRES observations of density cavities inside the plasmasphere, *J. Geophys. Res., 105*, 23,323-23,338, 2000.

Carruthers, G. R., T. Page, and R. R. Meier, Apollo 16 Lyman alpha imagery of the hydrogen geocorona, *J. Geophys. Res., 81*, 1664-1672, 1976.

Chakrabarti, S., F. Paresce, S. Bowyer, Y. T. Chiu, and A. Aikin, Plasmaspheric helium ion distribution from satellite observations of He II 304Å, *Geophys. Res. Lett., 9*, 151-154, 1982.

Chappell, C. R., K. K. Harris, and G. W. Sharp, The dayside of the plasmasphere, *J. Geophys. Res., 76*, 7632-7647, 1971

Chen, J., Prominence eruptions and geoeffective solar wind structures, in *Magnetic Storms*, edited by B. T. Tsurutani, W. D. Gonzalez, Y. Kamide, and J. K. Arballo, 45-58, Geophysical Monograph 98, American Geophysical Union, Washington, D. C., 1997.

Collin, H. L., R. D. Sharp, E. G. Shelley, and R. G. Johnson, Some general characteristics of upflowing ion beams over the auroral zone and their relationship to auroral electrons, *J. Geophys. Res., 86*, 6820-6826, 1981.

Cornwall, J. M., Magnetospheric ion acceleration processes, in Ion Acceleration in the Magnetosphere and Ionosphere, ed. by T. Chang, 3-16, Geophysical Monograph 38, American Geophysical Union, Washington, D. C., 1986.

Crooker, N. U., Dayside merging and cusp geometry, *J. Geophys. Res., 84*, 951-959, 1979.

Daglis, I. A., R. M. Thorne, W. Baumjohann, and S. Orsini, The terrestrial ring current: origin, formation, and decay, *Rev. Geophys., 37*, 407-438, 1999.

Dessler, A. J., and E. N. Parker, Hydromagnetic theory of geomagnetic storms, *J. Geophys. Res., 64*, 2239-2252, 1959.

Fok, M.-C., and T. E. Moore, Ring current modeling in a realistic magnetic field configuration, *Geophys. Res. Lett., 24*, 1775-1778, 1997.

Fok, M.-C., T. E. Moore, J. U. Kozyra, G. C. Ho, and D. C. Hamilton, Three-dimensional ring current decay model, *J. Geophys. Res., 100*, 9619-9632, 1995.

Fok, M.-C., T. E. Moore, G. R. Wilson, J. D. Perez, X. X. Zhang, P. C:Son Brandt, D. G. Mitchell, E. C. Roelof, J.-M. Jahn, C. J. Pollock, and R. A. Wolf, Global ENA image simulations, *Space Sci,. Rev., 109*, 77-104, 2003.

Foster, J. C., and H. B. Vo, Average characteristics and activity dependence of the subauroral polarization stream, *J. Geophys. Res., 107*(A12), 1475, doi:10.1.29/2002JA009409, 2002.

Frank, L. A., J. D. Craven, J. L. Burch, and J. D. Winningham, Polar views of the earth's aurora with Dynamics Explorer, *Geophys. Res. Lett., 9*, 1001-1004, 1982.

Frey, H. U., T. D. Phan, S. A. Fuselier, and S. B. Mende, Continuous magnetic reconnection at Earth's magnetopause, *Nature, 426*, 533-537, doi:10.1038/nature02084, 2003a.

Frey, H. U., S. B. Mende, S. A. Fuselier, T. J. Immel, and N. Østgaard, Proton aurora in the cusp during southward IMF, *J. Geophys. Res., 108*(A7), 1277, doi:10.1029/2003JA009861, 2003b.

Fukushima, N., and Y. Kamide, Partial ring current models for worldwide geomagnetic disturbances, *Rev. Geophys. Space Phys., 11*, 795, 1973.

Fuselier, S. A., H. U. Frey, K. J. Trattner, S. B. Mende, and J. L. Burch, Cusp aurora dependence on IMF B_z, *J. Geophys. Res., 107*(A7), doi:10.1029/2001JA900165, 2002a.

Fuselier, S. A., H. L. Collin, A. G.Ghielmetti, E. S. Claflin, T. E. Moore, M. R. Collier, H. Frey, and S. B. Mende, Localized ion outflow in response to a solar wind pressure pulse, *J. Geophys. Res., 107*(A8), 1203, doi: 10.1029/2001JA000297, 2002b.

Fuselier, S. A., S. B. Mende, T. E. Moore, H. U. Frey, S. M. Petrinec, E. S. Claflin, and M. R. Collier, Cusp dynamics and ionospheric outflow, *Space Sci. Rev., 109*, 285-312, 2003.

Gazey, N. G. J., M. Lockwood, M. Grandé, C. H. Perry, P. N. Smith, S. Coles, A. D. Aylward, and R. J. Bunting, EISCAT/CRRES observations: nightside ionospheric ion outflow and oxygen-rich substorm injections, *Ann. Geophys. 14*, 1032-1043, 1996.

Gérard, J.-C., B. Hubert, D. V. Bisikalo, and V. I. Shematovich, A model of the Lyman-α line profile in the proton aurora, *J. Geophys. Res., 105*, 15795-15,806, 2000.

Gold, T., Motions in the magnetosphere of the Earth, *J. Geophys. Res., 64*, 1219-1224, 1959.

Goldstein, J., R. W. Spiro, P. H. Reiff, R. A. Wolf, B. R. Sandel, J. W. Freeman, and R. L. Lambour, IMF-driven overshielding electric field and the origin of

the plasmaspheric shoulder of May 24, 2000, *Geophysical Research Letters, 29*, doi: 10.1029/2001GL014534, 2002.

Goldstein, J., M. Spasojevic, P. H. Reiff, B. R. Sandel, W. T. Forrester, D. L. Gallagher, and B. W. Reinisch, Identifying the plasmapause in IMAGE EUV data using IMAGE RPI in situ steep density gradients, *J. Geophys. Res., 108*(A4), 1147, doi:10.1029/2002JA009475, 2003a.

Goldstein, J., R. W. Spiro, B. R. Sandel, R. A. Wolf, S.-Y. Su, and P. H. Reiff, Overshielding event of 28-29 July 2000, *Geophys. Res. Lett.*, *30*(8), 1421, doi:10.1029/2002GL016644, 2003b.

Goldstein, J., B. R. Sandel, M. R. Hairston, and P. H. Reiff, Control of plasmaspheric dynamics by both convection and sub-auroral polarization stream, *Geophys. Res. Lett.*, *30*(24), 2243, doi:10.1029/2003GL018390, 2003c.

Goldstein, J., B. R. Sandel, M. F. Thomsen, and P. H. Reiff, Simultaneous remote-sensing and in situ observations of plasmaspheric drainage plumes, *J. Geophys. Res.*, *109*(A03202), doi:10.1029/2003JA010281, 2004a.

Goldstein, J., B. R. Sandel, M. R. Hairston, and S. B. Mende, Plasmapause undulation of 17 April 2002, *Geophys. Res. Lett.*, *31*(L15801), doi:10.1029/2004GL019959, 2004b.

Goldstein, J., J. L. Burch, B. R. Sandel, S. B. Mende, P. C:son Brandt, and M. R. Hairston, Coupled response of the inner magnetosphere and ionosphere on 17 April 2002, *J. Geophys. Res.*, *110*(A03205), doi: 10.1029/2004JA010712, 2005.

Grebowsky, J. M., Model study of plasmapause motion, *J. Geophys. Res., 75*, 4329-4334, 1970.

Green, J. L., D. A. Gurnett, and S. D. Shawhan, The angular distribution of auroral kilometric radiation, *J. Geophys. Res., 82*, 1825-1838, 1977.

Green, J. L., R. F. Benson, S. F. Fung, W. W. L. Taylor, S. A. Boardsen, B. W. Reinisch, D. M. Haines, K. Bibl, G. Cheney, I. A. Galkin, X. Huang, S. H., Meyers, G. S. Sales, J.-L. Bougeret, R. Manning, N. Meyer-Vernet, M. Moncuquet, D. L. Carpenter, D. L. Gallagher, and P. H. Reiff, Radio Plasma Imager simulations and measurements, *Space Sci. Rev., 91*, 361-389, 2000.

Green, J. L., B. R. Sandel, S. F. Fung, D. L. Gallagher, and B. W. Reinisch, On the origin of kilometric continuum, *J. Geophys. Res., 107*(A7), 10.1029/2001JA000193, 2002.

Green, J. L., and B. W. Reinisch, An overview of results from RPI on IMAGE, *Space Sci. Rev*., *109*, 183-210, 2003.

Green, J. L., S. A. Boardsen, S. F. Fung, H. Matsumoto, K. Hashimoto, R. R. Anderson, B. R. Sandel, B. W. Reinisch, Association of Kilometric Continuum Radiation with Plasmaspheric Structures, *J. Geophys. Res*., *109*(A03203), doi: 10.1029/2003JA010093, 2004.

Gurnett, D. A., The Earth as a radio source: The nonthermal continuum, *J. Geophys. Res*., *80*, 2751-2763, 1975.

Gurnett, D. A., and L. A. Frank, Observed relationships between electric fields and auroral particle precipitation, *J. Geophys. Res., 78*, 145-170, 1973.

Harel, M., R. A. Wolf, R. W. Spiro, P. H,. Reiff, C.-K. Chen, W. J. Burke, F. J. Rich, and M. Smiddy, Quantitative simulation of a magnetospheric substorm 2. Comparison with observations, *J. Geophys. Res., 86*, 2242-2260, 1981.

Hashimoto, K., W. Calvert, and H. Matsumoto, Kilometric continuum detected by Geotail, *J. Geophys. Res*., *104***,** 28,645-28,656, 1999.

Heelis, R. A., and R. J. Coley, East-west ion drifts at mid-latitudes observed by Dynamics Explorer 2, J. Geophys. Res., 97, 19,461-19,469, 1992.

Henderson, M. G., G. D. Reeves, H. E. Spence, R. B. Sheldon, A. M. Jorgensen, J. B. Blake, and J. F. Fennell, First energetic neutral atom images from Polar, *Geophys. Res. Lett., 24*, 1167-1170, 1997.

Hill, T. W., Inertial limit on corotation, *J. Geophys. Res., 84*, 6554-6558, 1979.

Hoffman, R. A., and P. A. Bracken, Magnetic effects of the quiet-time proton belt, *J. Geophys. Res., 70*, 3541-3556, 1965.

Hultqvist, B., M. André, S. P. Christon, G. Paschmann, D. G. Sibeck, Contributions of different source and loss processes to the plasma content of the magnetosphere, Ch. 7 of *Magnetospheric Plasma Sources and Losses*, edited by B. Hultqvist, M. Øieroset, G. Paschmann, and R. Treumann, Kluwer Academic Publishers, Dordrecht, 1999.

Jordanova, V. K., J. U. Kozyra, A. G. Nagy and G. V. Khazanov, Kinetic model of the ring current-atmosphere interactions, *J. Geophys. Res., 102*, 14,279-14,291, 1997.

Jordanova, V. K., C. J. Farrugia, J. M. Quinn, R. M. Thorne, K. W. Ogilvie, R. P. Lepping, G. Lu, A. J. Lazarus, M. F. Thomsen and R. D. Belian, Effect of wave-particle interactions on ring current evolution for January 10-11, 1997: Initial results, *Geophys. Res. Lett., 25*, 2971-2974, 1998.

Jorgensen, A. M., L. Kepko, M. G. Henderson, H. E. Spence, G. D. Reeves, J. B. Sigwarth, and L. A. Frank, Association of energetic neutral atom bursts and magnetospheric substorms, *J. Geophys. Res., 105*, 18,753-18,763, 2000.

Kozyra, J. U., V. K. Jordanova, R. B. Horne and R. M. Thorne, Modeling of the contribution of electromagnetic ion cyclotron (EMIC) waves to stormtime ring current erosion, in *Magnetic Storms*, edited by B. T. Tsurutani, W. D. Gonzalez, Y. Kamide, and J. K. Arballo, 187-202, Geophysical Monograph No. 98, American Geophysical Union, Washington, D. C., 1997.

Larson, N. R., and G. K. Parks, Motions of particle microstructures in the magnetopause boundary layer, *J. Geophys. Res., 97*, 10733-10749, 1992.

Liemohn, M. W., J. U. Kozyra, M. F. Thomsen, J. L. Roeder, G. Lu, J. E. Borovsky, and T. E. Cayton, Dominant role of the asymmetric ring current in producing the stormtime *Dst**, *J. Geophys. Res., 106*, 10,883-10,904, 2001.

McComas, D. J., S. J. Bame, B. L. Barraclough, J. R. Donart, R. C. Elphic, J. T. Gosling, M. B. Moldwin, K. R. Moore, and M. F. Thomsen, Magnetospheric Plasma Analyzer: Initial three-spacecraft observations from geosynchronous orbit, *J. Geophys. Res., 98*, 13,453-13,465, 1993.

McIlwain, C. E., A Kp dependent equatorial electric field model, *Adv. Space Res., 6*(3), 187, 1986.

Meier, R. R., Ultraviolet spectroscopy and remote sensing of the upper atmosphere, *Space Sci. Rev., 59*, 1, 1991.

Mende, S. B., H. Heetderks, H. U. Frey, J. M. Stock, M. Lampton, S. P. Geller, R. Abiad, O. H., W. Siegmund, S. Hagraken, E. Renotte, C. Jamar, P. Rochus, J.-C. Gérard, R. Sigler and H. Lauche, Far-Ultraviolet Imaging from the IMAGE Spacecraft. 3. Spectral imaging of Lyman-alpha and OI 135.6 nm, *Space Sci. Rev.*, *91*, 287-318, 2000.

Mitchell, D. G., S. E. Jaskulek, C. E. Schlemm, E. P. Keath, R. E. Thompson, B. E. Tossman, J. D. Boldt, J. R. Hayes, G. B. Andrews, N. Paschalidis, D. C. Hamilton, R. A. Lundgren, E. O. Tums, P. Wilson IV, H. D. Voss, D. Prentice, K. C. Hsieh, C. C. Curtis and F. R. Powell, The High-Energy Neutral Atom (HENA) imager for the IMAGE mission, *Space Sci. Rev.*, *91*, 67-112, 2000.

Mitchell, D. G., C. P. Paranicas, B. H. Mauk, E. C. Roelof, S. M. Krimigis, Energetic neutral atoms from Jupiter measured with the Cassini magnetospheric imaging instrument: Time dependence and composition, *J. Geophys. Res.*, *109*(A09S11), doi:10.1029/2003JA010120, 2004.

Moore, T. E., Superthermal ionospheric outflows, *Rev. Geophys. Space Phys., 22*, 264-274, 1984.

Moore, T. E., D. J. Chornay, M. R., Collier, F. A. Herrero, J. Johnson, M. A. Johnson, J. W. Keller, J. F. Laudadio, J. F. Lobell, K. W. Ogilvie, P. Rozmarynowski, S. A. Fuselier, A. G. Ghielmetti, E. Hertzberg, D. C. Hamilton, R. Lundgren, P. Wilson, P. Walpole, R. M. Stephen, B. L. Peko, B. Van Zylk, P. Wurz, J. M. Quinn and G. R. Wilson, The Low-Energy Neutral Atom (LENA) imager investigation, *Space Sci. Rev.*, *91*, 155-195, 2000.

Nakamura, M., I. Yoshikawa, A. Yamazaki, K. Shiomi, Y. Takizawa, M. Hirahara, K. Yamashita, Y. Saito, and W. Miyake, Terrestrial plasmaspheric imaging by an extreme ultraviolet scanner on Planet-B, *Geophys. Res. Lett., 27*, 141-144, 2000.

Newell, P. T., C.-I. Meng, D. G. Sibeck, and R. Lepping, Some low-altitude cusp dependencies on the interplanetary magnetic field, *J. Geophys. Res., 94*, 8921-8927, 1989.

Northrop, T. G., and E. Teller, Stability of the adiabatic motion of charged particles in the Earth's field, *Phys. Rev., 117*, 215-225, 1960.

Parker, E. N., Newtonian development of the dynamical properties of ionized gases of low density, *Phys. Rev., 107*, 924-933, 1957.

Peterson, W. K., H. L. Collin, M. F. Doherty, and C. M. Bjorklund, O^+ and He^+ restricted and extended (bi-modal) ion conic distributions, *Geophys. Res. Lett., 19*, 1439-1442, 1992.

Phan, T., H. U. Frey, S. Frey, L. Peticolas, S. Fuselier, C. Carlson, H. Reme, J.-M. Bosqued, A. Balogh, M. Dunlop, L. Kistler, C. Mouikis, I. Dandouras, J.-A. Savaud, S. Mende, J. McFadden, G. Parks, E. Moebius, B. Klecker, G. Paschmann, M. Fujimoto, S. Petrinec, M. F. Marcucci, A. Korth, and R. Lundin, Simultaneous Cluster and IMAGE observations of cusp

reconnection and auroral proton spot for northward IMF, *Geophys. Res. Lett., 30*(10), 1509, doi: 10.1029/2003GL016885, 2003.

Pollock, C. J., K. Asamura, J. Baldonado, M. M. Balkey, P. Barker, J. L. Burch, E. J. Korpela, J. Cravens, G. Dirks, M.-C. Fok, H. O. Funsten, M. Grande, M. Gruntman, J. Hanley, J.-M. Jahn, M. Jenkins, M. Lampton, M. Marckwordt, D. J. McComas, T. Mukai, G. Penegor, S. Pope, S. Ritzau, M. L. Schattenburg, E. Scime, R. Skoug, W. Spurgeon, T. Stecklein, S. Storms, C. Urdiales, P. Valek, J. T. M. Van Beek, S. E. Weidner, M. Wüest, M. K. Young and C. Zinsmeyer, Medium Energy Neutral Atom (MENA) imager for the IMAGE mission, *Space Sci. Rev.*, *91*, 113-154, 2000.

Pontius, D. H., and T. W. Hill, Departure from corotation of the Io plasma torus: local plasma production, *Geophys. Res. Lett., 9*, 1321-1324, 1982.

Rairden, R. L., L. A. Frank, and J. D. Craven, Geocoronal imaging with Dynamics Explorer, *J. Geophys. Res., 91*, 13,613-13,630, 1986.

Reiff, P. H., and J. L. Burch, IMF B_Y-dependent plasma flow and Birkeland currents in the dayside magnetosphere: 2. A global model for northward and southward IMF, *J. Geophys. Res*., *90*, 1595-1610, 1985.

Roelof, E. C., and A. J. Skinner, Extraction of ion distributions from magnetospheric ENA and EUV images, *Space Sci. Rev., 91*, 437-460, 2000.

Sandel, B. R., A. L. Broadfoot, C. C. Curtis, R. A. King, T. C. Stone, R. H, Hill, J. Chen, O. H. W. Siegmund, R. Raffanti, D. D. Allred, R. S. Turley, and D. L. Gallagher, The Extreme Ultraviolet (EUV) Imager Investigation for the IMAGE mission, *Space Sci. Rev.*, *91*, 197-242, 2000.

Sandel, B. R., R. A. King, W. T. Forrester, D. L. Gallagher, A. L. Broadfoot, and C. C. Curtis, Initial results from the IMAGE extreme ultraviolet imager, *Geophys. Res. Lett., 28***,** 1439-1442, 2001.

Sandel, B. R., J. Goldstein, D. L. Gallagher, and M. Spasojevic, Observations of the structure and dynamics of the plasmasphere, *Space Sci. Rev., 109*, 25-46, 2003.

Sckopke, N., A general relation between the energy of trapped particles and the disturbance field near the Earth, *J. Geophys. Res., 71*, 3125-3130, 1966.

Sheeley, N. R., Jr., J. W. Harvey, and W. C. Feldman, Coronal holes, solar wind streams, and recurrent geomagnetic disturbances: 1973-1976, *Solar Phys*., *49*, 271-278, 1976.

Smith, M. F., and M. Lockwood, Earth's magnetospheric cusps, *Rev. Geophys., 34*, 233-260, 1996.

Spasojevic, M., J. Goldstein, D. L. Carpenter, U. S. Inan, B. R. Sandel, M. B. Moldwin, and B. W. Reinisch, Global response of the plasmasphere to a geomagnetic disturbance, *J. Geophys. Res., 108*(A9), doi: 10.1029/2003JA009987, 2003.

Stern, D. P., The motion of a proton in the equatorial magnetosphere, *J. Geophys. Res., 80*, 595-599, 1975.

Terasawa, T., M. Fujimoto, T. Mukai, I. Shinohara, Y. Saito, T. Yamamoto, S. Machida, S. Kokubun, A. J. Lazarus, J. T. Steinberg, and R. P. Lepping, Solar wind control of density and temperature in the near-Earth plasma sheet: WIND/GEOTAIL collaboration, *Geophys. Res. Lett., 24*, 935-938, 1997.

Thorne, R. M., and R. B. Horne, Modulation of electromagnetic ion cyclotron instability due to interaction with ring current O^+ during magnetic storms, *J. Geophys. Res., 102*, 14,155-14,163, 1997.

Tsyganenko, N. A., A model of the near magnetosphere with a dawn-dusk asymmetry - 1. Mathematical Structure, *J. Geophys. Res., 107*(A8), doi: 10.1029/2001JA000219, 2002.

Vasyliunas, V. M., Theoretical models of magnetic field line merging, 1, *Rev. Geophys. Space Phys., 13*, 303-336, 1974.

Van Allen, J. A., George H. Ludwig, Ernest C. Ray and Carl E. McIlwain, Observation of high intensity radiation by satellites 1958 Alpha and Gamma, *Jet Propulsion, 28*, 588-592, 1958.

Volland, H., A semiempirical model of large-scale magnetospheric electric fields, *J. Geophys. Res., 78*, 171-180, 1973.

Weimer, D. R., Models of high-latitude electric potentials derived with a least error fit of spherical harmonic coefficients, *J. Geophys. Res., 100*, 19,595-19,608, 1995.

Weller, C. S., and R. R. Meier, First satellite observations of the He^+ 304-Å radiation and its interpretation, *J. Geophys. Res., 79*, 1572, 1974.

Williams, D. J., E. C. Roelof, and D. G. Mitchell, Global magnetospheric imaging, *Rev. Geophys., 30*, 183-208, 1992.

Wygant, J., D. Rowland, H. J. Singer, M. Temerin, F. Mozer, and M. K. Hudson, Experimental evidence on the role of the large spatial scale electric field in creating the ring current, *J. Geophys. Res., 103*, 29,527-29,544, 1998.

Yeh, H.-C., J. C. Foster, F. J. Rich, and W. Swider, Storm time electric field penetration observed at mid-latitude, *J. Geophys. Res., 96*, 5707-5721, 1991.

Young, J. M., G. R. Carruthers, J. C. Holmes, C. Y. Johnson, and N. P. Patterson, Detection of Lyman-α and helium resonance radiation in the night sky, *Science, 160*, 990, 1968.

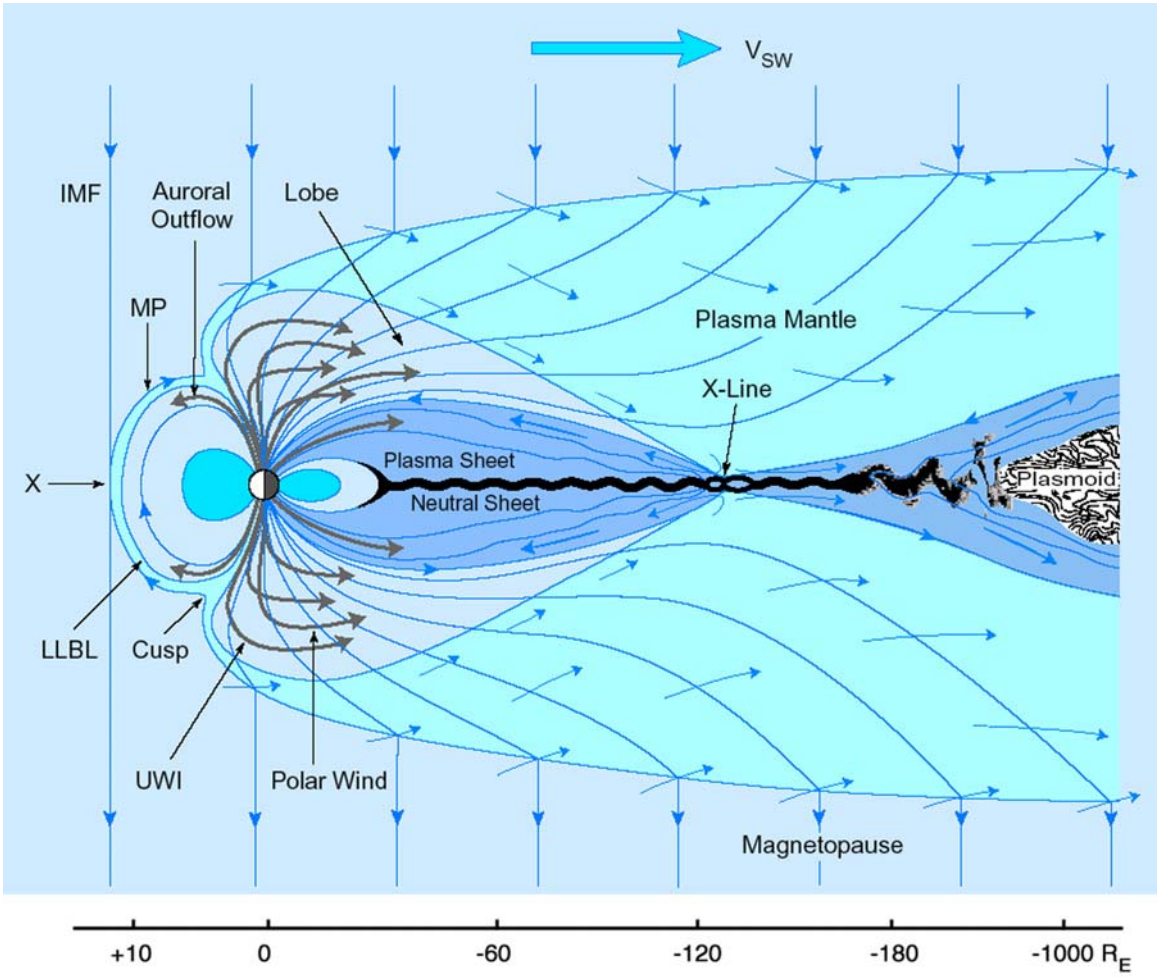

Fig. 1. Schematic (not to scale) of the magnetic field and plasma configurations of the magnetosphere. The processes of magnetopause and tail reconnection (X and X-Line) and plasma outflow from the ionosphere (Auroral Outflow; Polar Wind; and Upwelling Ions, UWI) are indicated. The figure has been drawn for purely southward IMF. Open field-lines resulting from magnetopause reconnection convect antisunward, allowing plasma to penetrate the magnetosphere and to form the plasma mantle (lighter turquoise area). Near-Earth mantle plasma convects slowly cross-tail towards the plasma sheet where reconnection generates plasma jetting in the Earthward and antisunward directions, causing a macroscopic instability of the neutral sheet tail current, plasmoids in the far distant tail, and plasma losses to ionosphere and solar wind. The plasmasphere, ring current, and radiation belts are Earthward of the plasma sheet and overlap the darker turquoise region nearest the Earth. Note that the distance scale along the bottom is highly nonlinear. Figure is reprinted from *Hultqvist et al*., [1999].

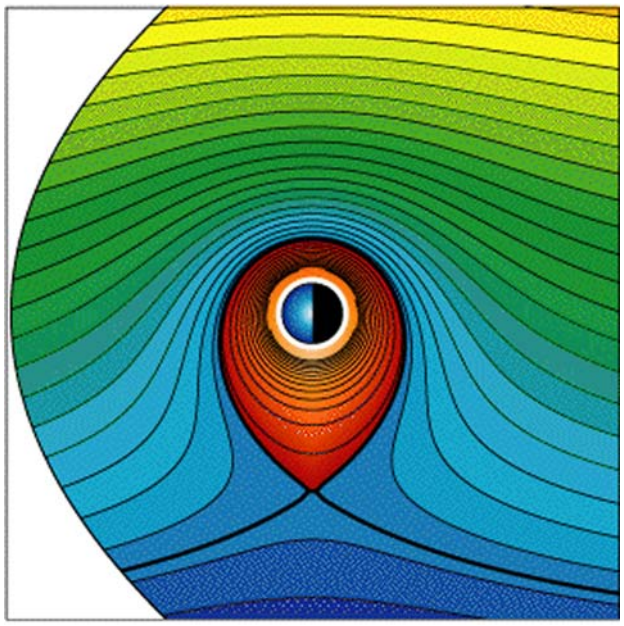

Fig. 2. Electric equipotentials in the equatorial inner magnetosphere for the combination of a corotation electric field and a dawn-dusk convection electric field. The view is looking down on the equatorial plane from above the north pole. The Sun is to the left. (Figure provided by J. Goldstein).

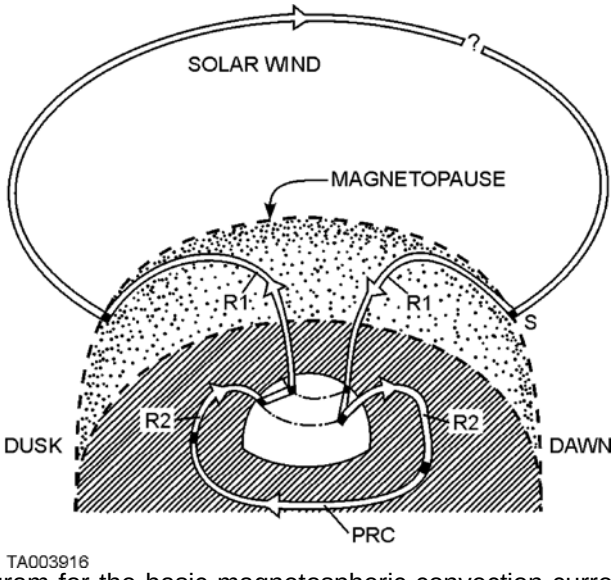

Fig. 3. Schematic diagram for the basic magnetospheric-convection current system. The view is from behind the Earth, looking sunward. The lined region is the equatorial plane; the dotted region the dayside magnetopause. R1, R2, and PRC stand for region-1 current, region-2 current and partial ring current, respectively [from *Harel et al*., 1981].

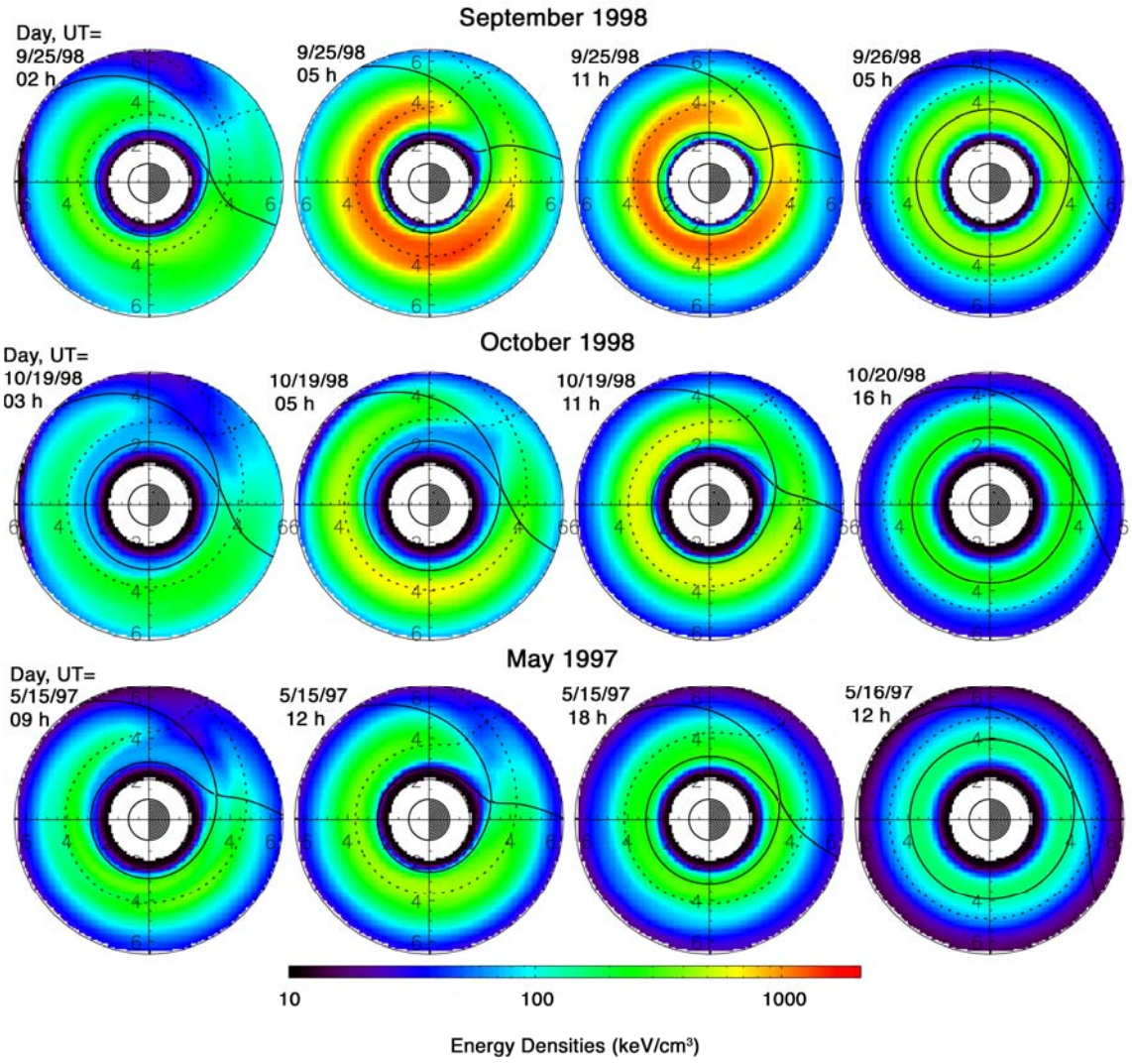

Fig. 4. Equatorial plane energy density of the simulated ring current (McIlwain field description, summed H^+ and O^+) at four times: (a) growth phase, (b) storm peak, (c) early recovery, and (d) late recovery during the three storms in (top) September 1998, (middle) October 1998, and (bottom) May 1997. The solid and dotted lines are the $E_{6.6}$=3 and 12 keV last closed drift trajectories for ions that have energies at geosynchronous orbit (6.6 Earth radii geocentric distance) of 3 Kev and 12 keV, respectively. Figure adapted from *Liemohn et al*. [2001].

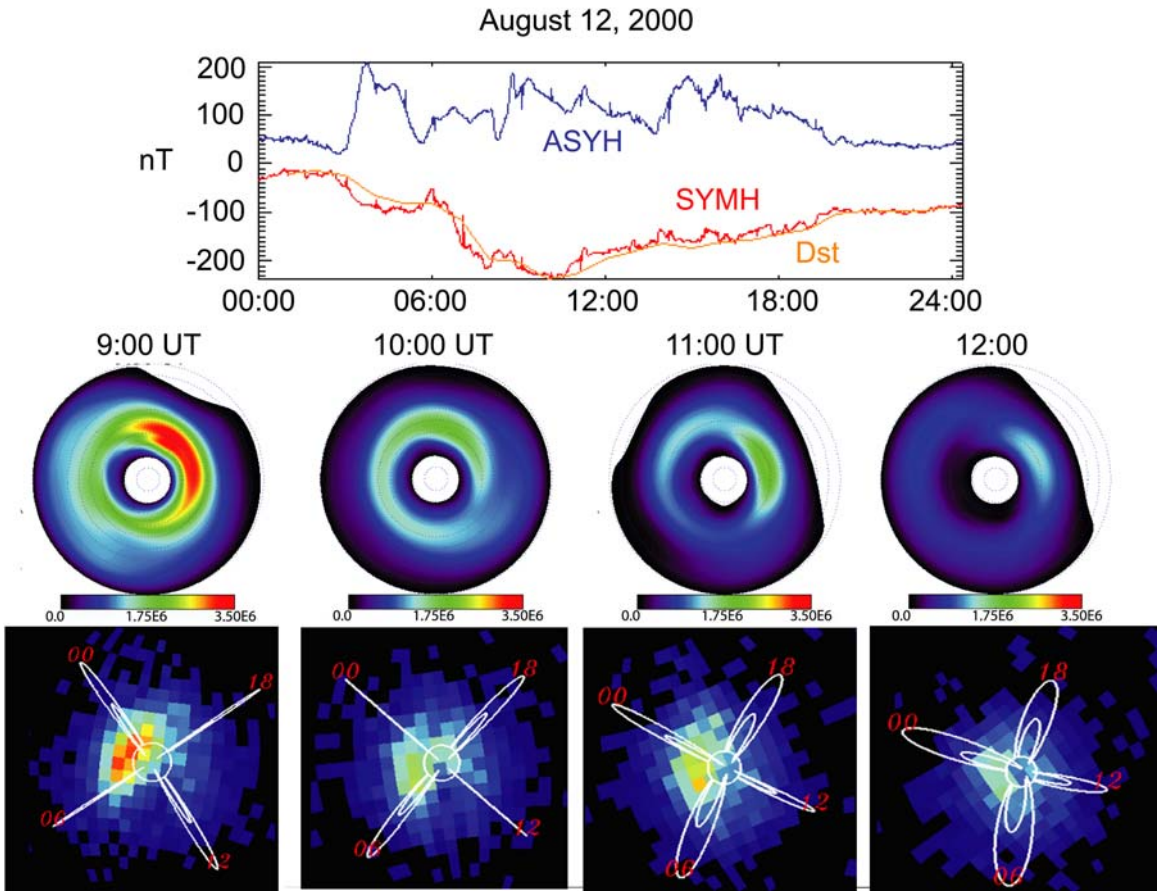

Fig. 5. Ring current observations for 12 August 2000. The top panel shows ASYH (blue), SYMH (red), and Dst (orange) for the entire day. The middle panel shows equatorial ion flux ([keV s sr cm^2]$^{-1}$) averaged over pitch angle in the energy range 27-39 keV deconvolved from HENA ENA images from 9:00-12:00 UT; the Sun is to the left, and dawn is up; the dotted circles are 1 R_E apart. The third row shows the HENA data. Field lines for L=4 and L=8 are shown, and MLT is noted in red on each image. The color bars shown apply to the simulations and not to the data. Note that in the simulations and the data, the ring current peaks in the 00 – 06 MLT range. Figure adapted from *Fok et al*. [2003].

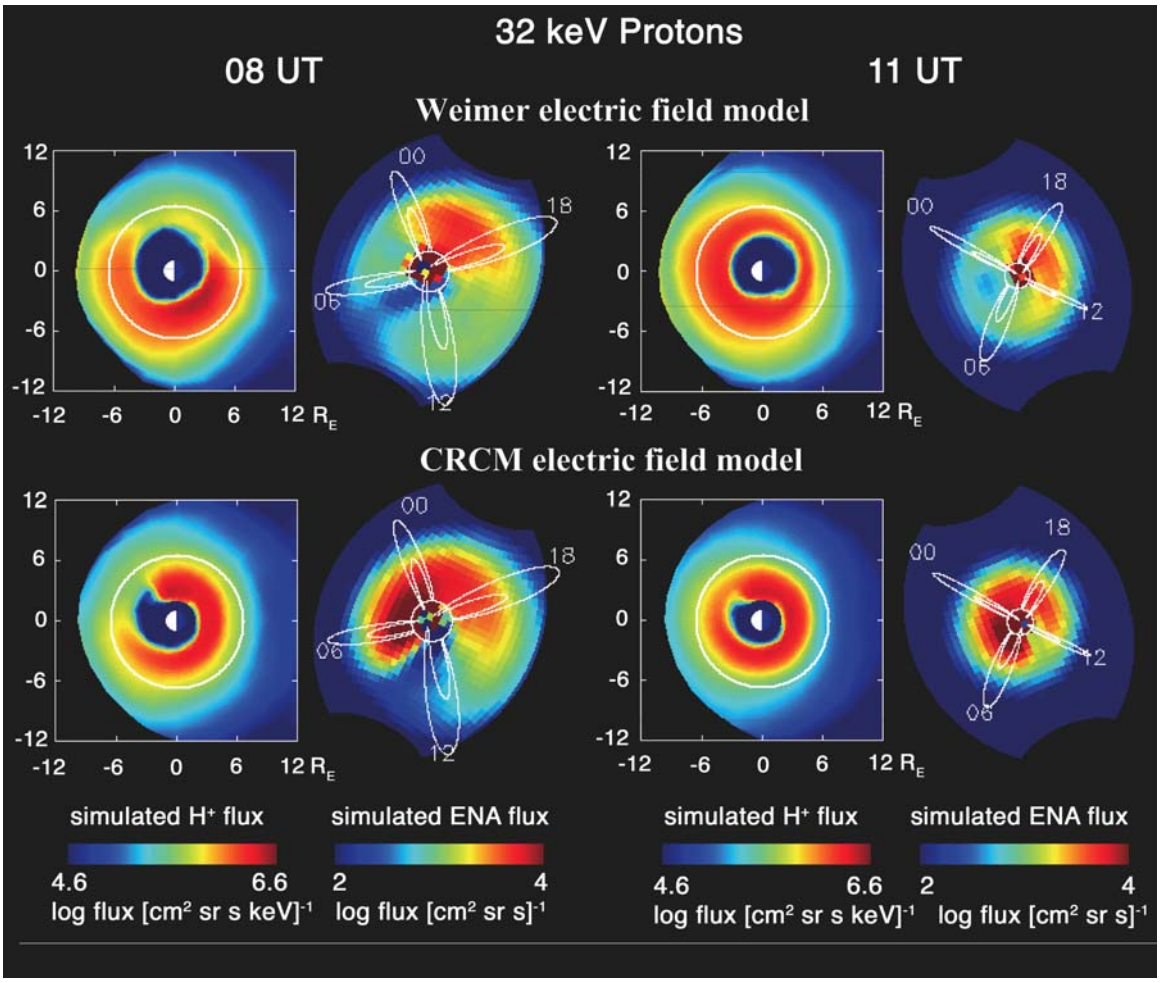

Fig. 6. Simulated 32 keV H^+ fluxes at the equator and the associated ENA images at 8 UT (2 left columns) and 11 UT (2 right columns) on 12 August 2000. In the ion plots, the Sun is to the left and the white circles are at an equatorial distance of 6.6 R_E [from *Fok et al*., 2003].

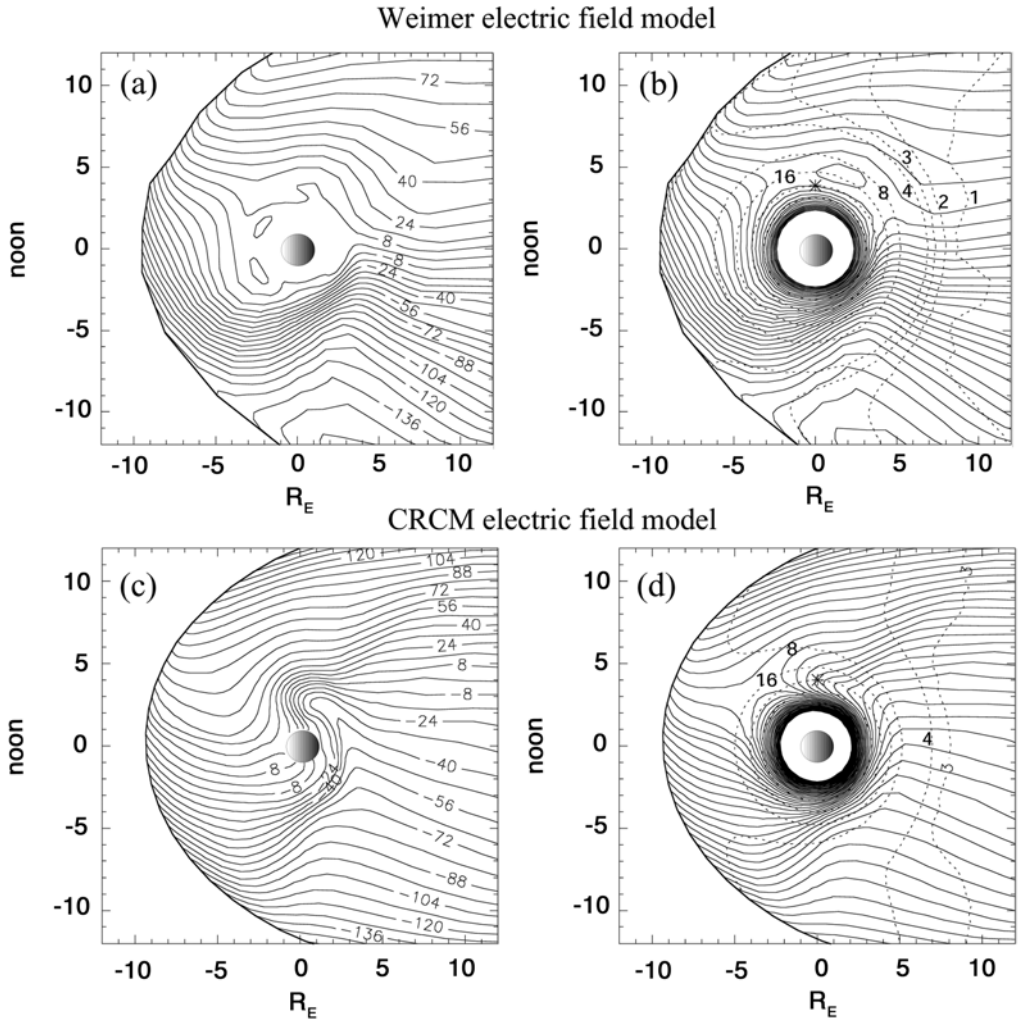

Fig. 7. Left panels: model potential contours at the magnetic equator at 8 UT, 12 August 2000, (a) Weimer model, and (c) CRCM. Contours are drawn at every 8 kV. Right panels: drift paths (solid lines) of equatorially mirroring ions with constant magnetic moment calculated with (b) Weimer model, and (d) CRCM. Dashed lines are energy contours in keV. The energy of these ions is 32 keV at 3.9 R_E and 06 MLT [from *Fok et al*., 2003].

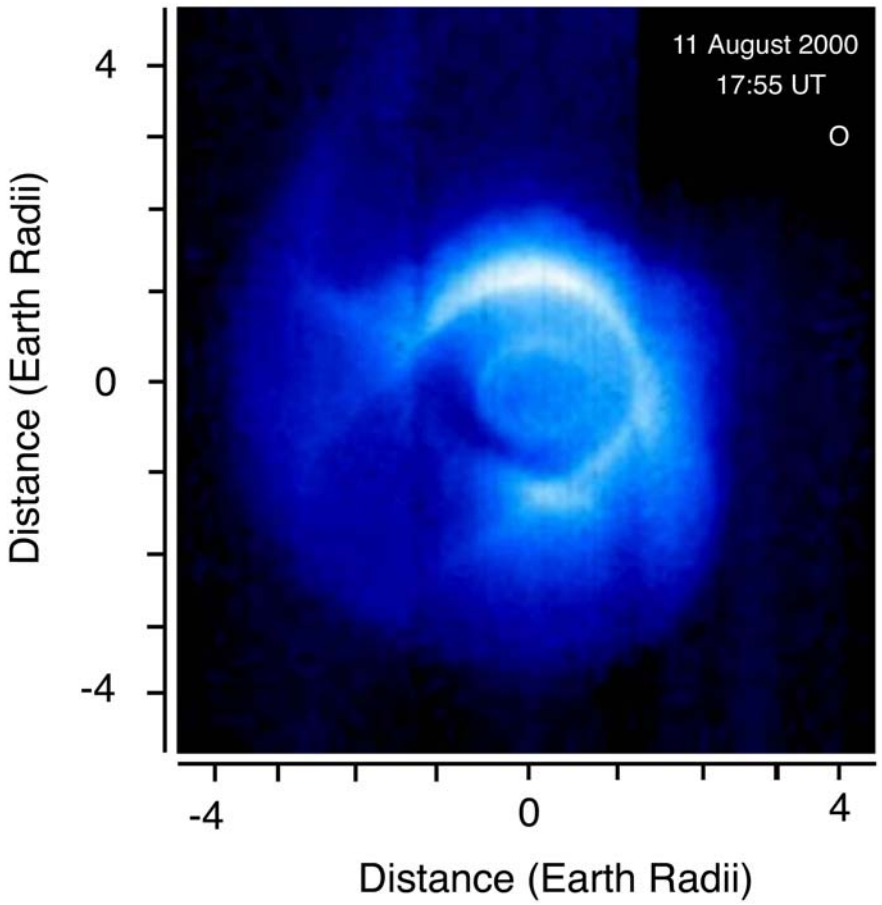

Fig. 8. He^+ distributions on August 11, 2000. The small circle to the upper right marks approximately the direction toward the Sun, and Earth's shadow is the dark region extending through the plasmasphere toward the lower left. A plasma tail extends sunward from the main plasmasphere near the dusk meridian [adapted from *Sandel et al*., 2001].

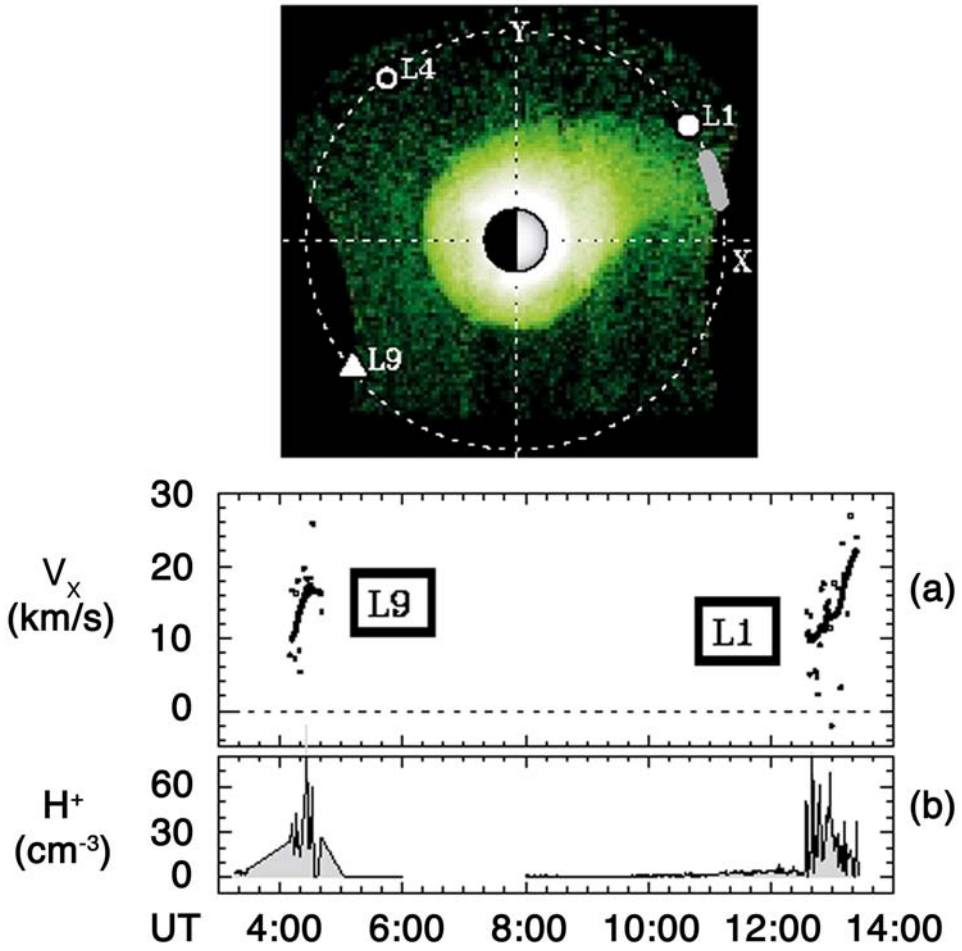

Fig. 9. (Top panel) Snapshot of the plasmasphere during a plasma plume event at 14:06 UT on June 26, 2000. The locations of LANL geosynchronous satellites L1, L4, and L9 are shown with the encounter of L1 with the plasma plume denoted by the gray bar. (Bottom panel) LANL MPA sunward flows and densities of plume plasma measured on 26 June 2000 during plasmasphere erosion. Panels (a) and (b) plot the *X*-component (Sunward) of the flow velocities and the plasma densities, respectively, for LANL satellites L1 and L9. The bold curves are the 14-minute averaged sunward flows. Adapted from *Goldstein et al*. [2004].

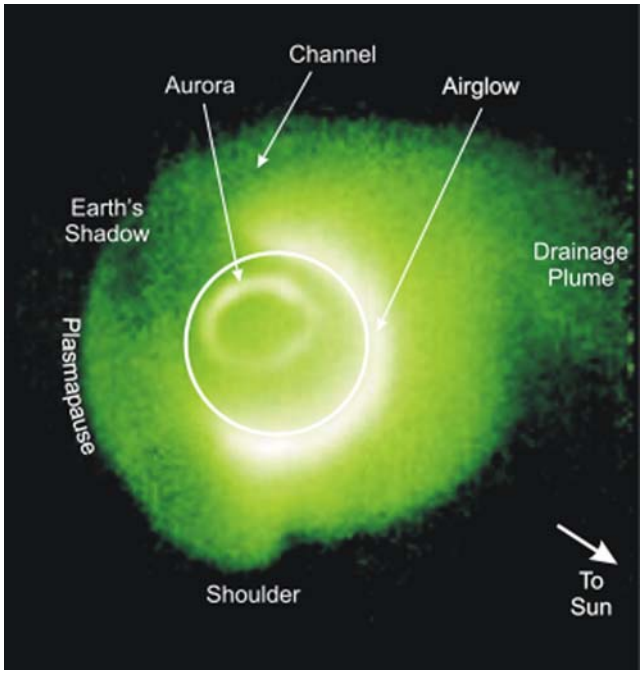

Fig. 10. IMAGE-EUV image of the plasmasphere on May 24, 2000. Several commonly observed features of the images are noted, including the drainage plume and shoulder. Figure provided by B. R. Sandel.

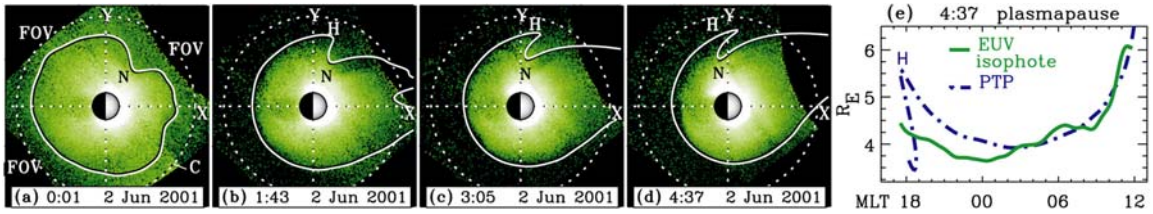

Fig. 11. Four snapshots of the June 2, 2001 plasmaspheric erosion showing the EUV equatorial He^+ abundance. Bright patch 'C' in panel (a) is sunlight contamination. The Sun is to the right. The X- and Y- axes, and geosynchronous orbit are drawn as dotted lines. The solid white curves represent the plasmapause (major plasma gradients) determined by a test-particle simulation in the Volland-Stern electric field model. "N" denotes a notch; "H" denotes the bulge. Panel e shows plasmapause position in MLT and radial distance derived from the EUV image (solid green) and the simulation (broken blue) for the time plotted in panel d. Figure taken from *Goldstein et al*., [2003c].

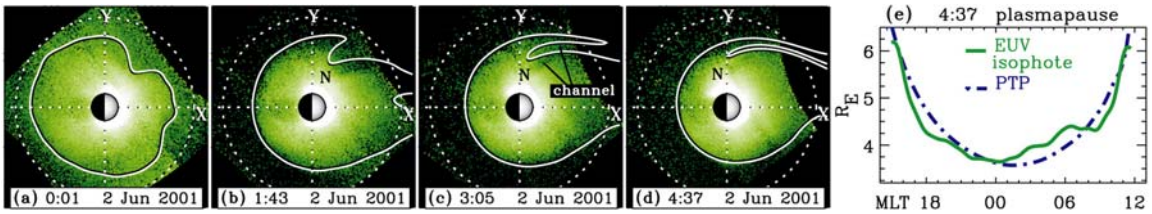

Fig. 12. Same as Figure 11 except solid white curves are loci of major plasma gradients for Volland-Stern plus SAPS model. Figure taken from *Goldstein et al*., [2003c].

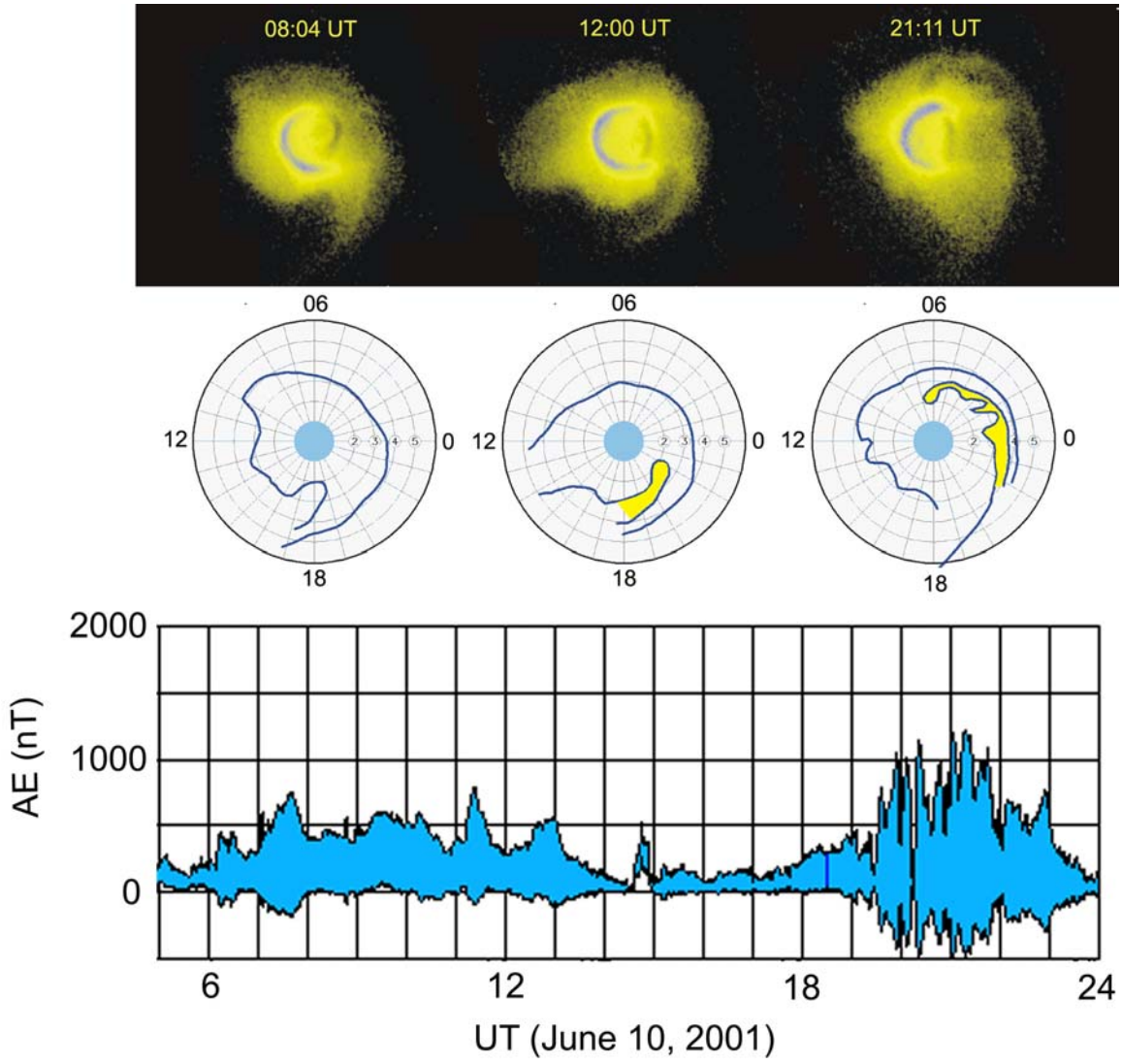

Fig. 13. (Top) EUV images, on June 10, 2001 scaled to a common range and rotated so that the Sun is to the left. (Bottom) Mapping of the prominent brightness gradients to the plane of the magnetic equator in [L, MLT] space [*Sandel et al*., 2003].

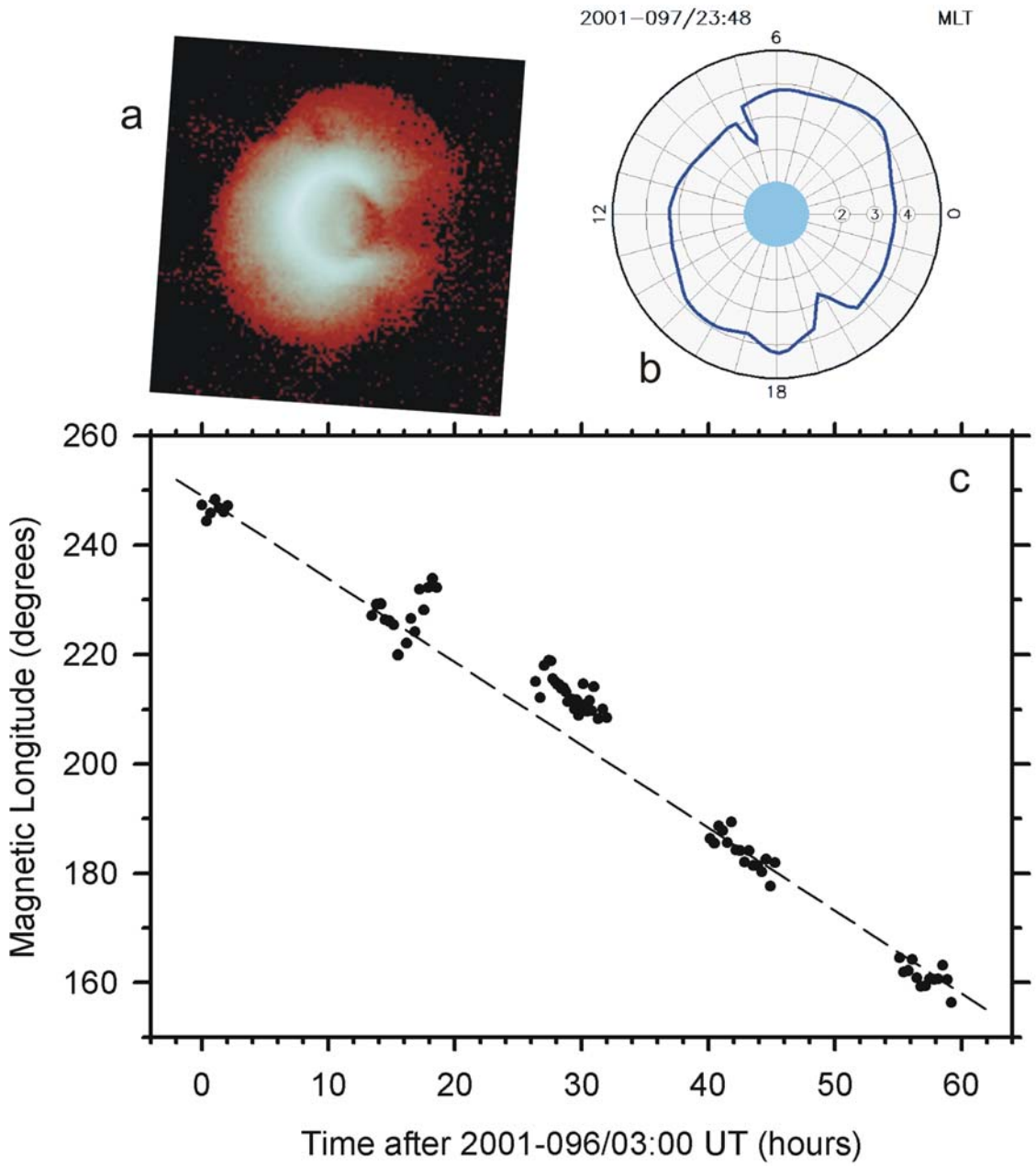

Fig. 14. Example of a measurement of the angular velocity of plasmaspheric plasma. (a) The EUV image for 23:48 UT on 7 April 2001, showing two notches separated by about 180° in azimuth. (b) Mapping of prominent brightness gradients to the plane of the magnetic equator in [L, MLT] space. (c) Magnetic longitude of the notch near 7.5 hours MLT in panel b as a function of time. Over this period of 60 hours, the notch drifted in longitude at a nearly constant rate. The dashed line corresponds to an angular velocity that is 90% of the corotation velocity [from *Sandel et al*., 2003].

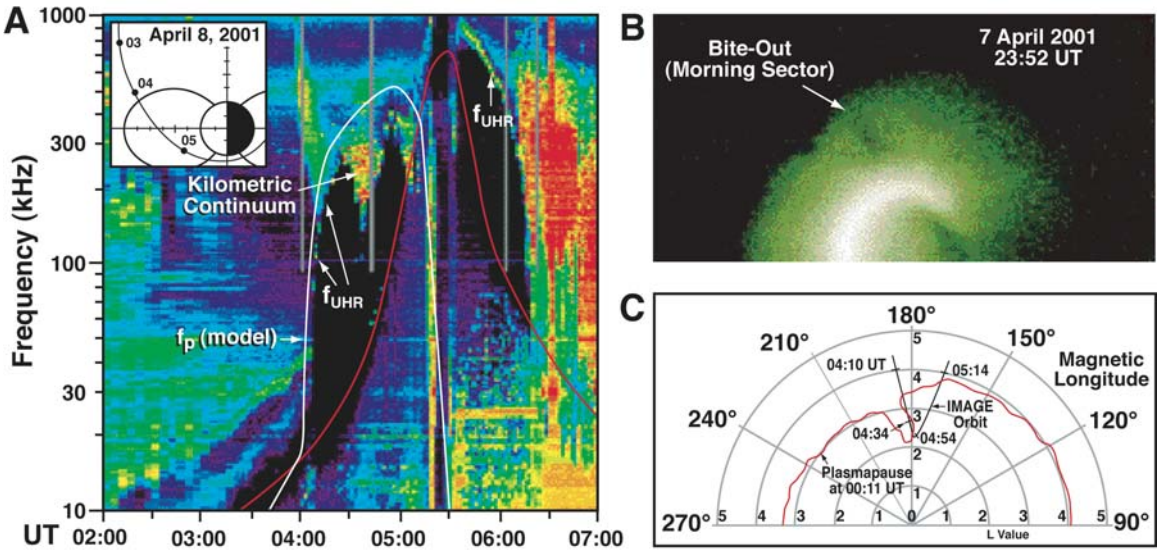

Fig. 15. Panel A is a RPI spectrogram obtained during the passage of the IMAGE spacecraft through the plasmasphere nearly in the noon-midnight meridian plane on April 8, 2001. The deviation of the f_{uhr} emission from the model f_p from 04:25 to 04:50 UT indicates that IMAGE passed through a deep density depression in the dayside plasmasphere. Panel B is an EUV He^+ image of the plasmasphere showing a distinct bite-out (notch) region taken several hours before the passage of IMAGE through the plasmasphere. Assuming that the bite-out (notch) region continues to corotate, panel C shows that the deep density depression observed by RPI was the bite-out structure previously observed by EUV. As shown in panel A, kilometric continuum was observed to be confined to the bite-out region. This figure was adapted from *Green et al*., [2003b].

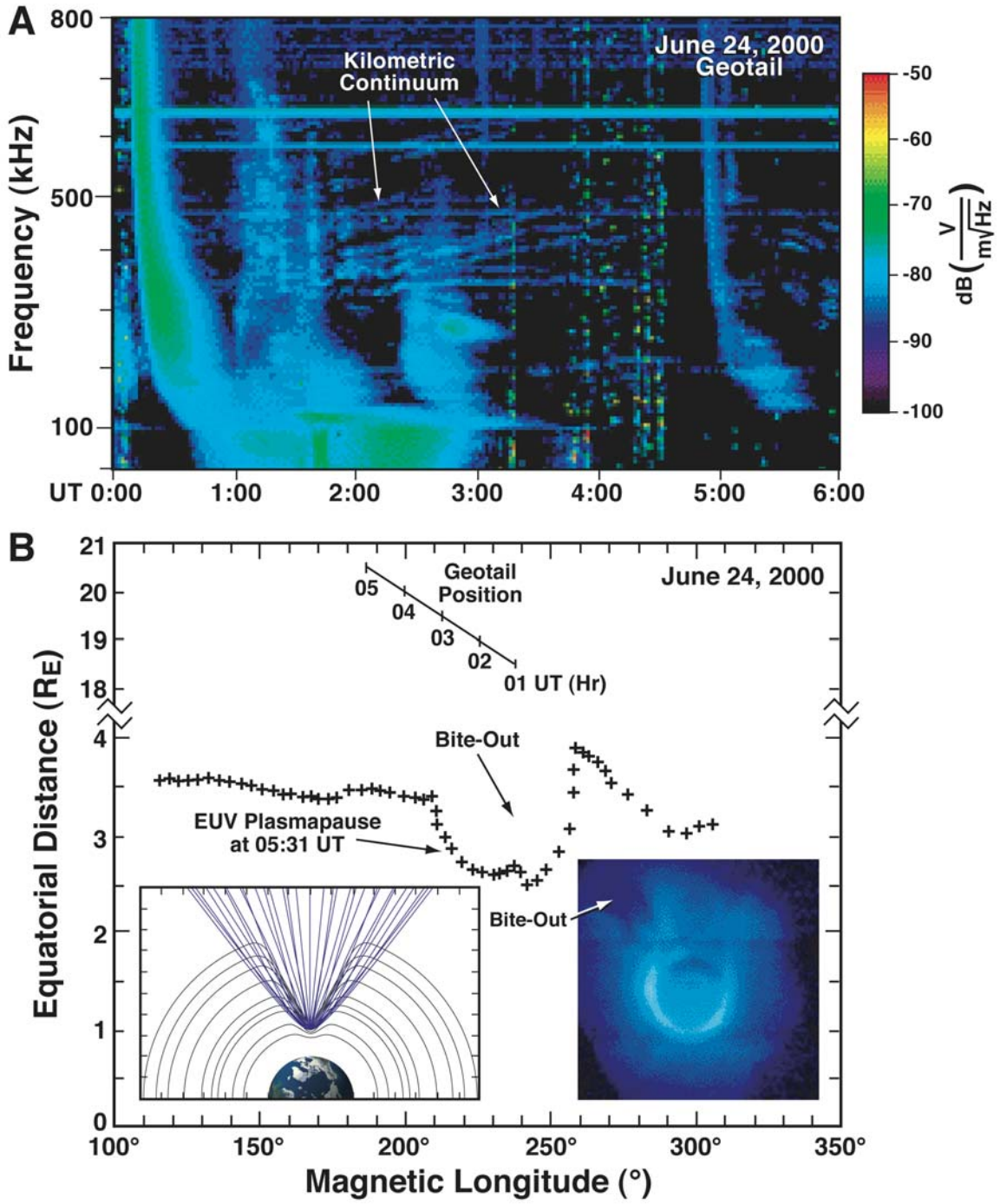

Figure 16. Panel A is a frequency time spectrogram from the Geotail spacecraft showing the banded structure of the kilometric continuum stretching from about 01:00 to 05:00 UT over the frequency range above 100 kHz to 600 kHz. Panel B shows the simultaneous EUV observations (inset) from IMAGE of a large bite-out structure plotted in magnetic longitude and compared to the position of Geotail during its observations of kilometric continuum of panel A. Ray tracing results (inset in panel B) show that a source of kilometric continuum at the f_{uhr} frequency deep inside the bite-out structure produces an emission cone largely confined to the bite-out structure which is also consistent with the Geotail observations. This figure was adapted from *Green et al*., [2003, 2004].

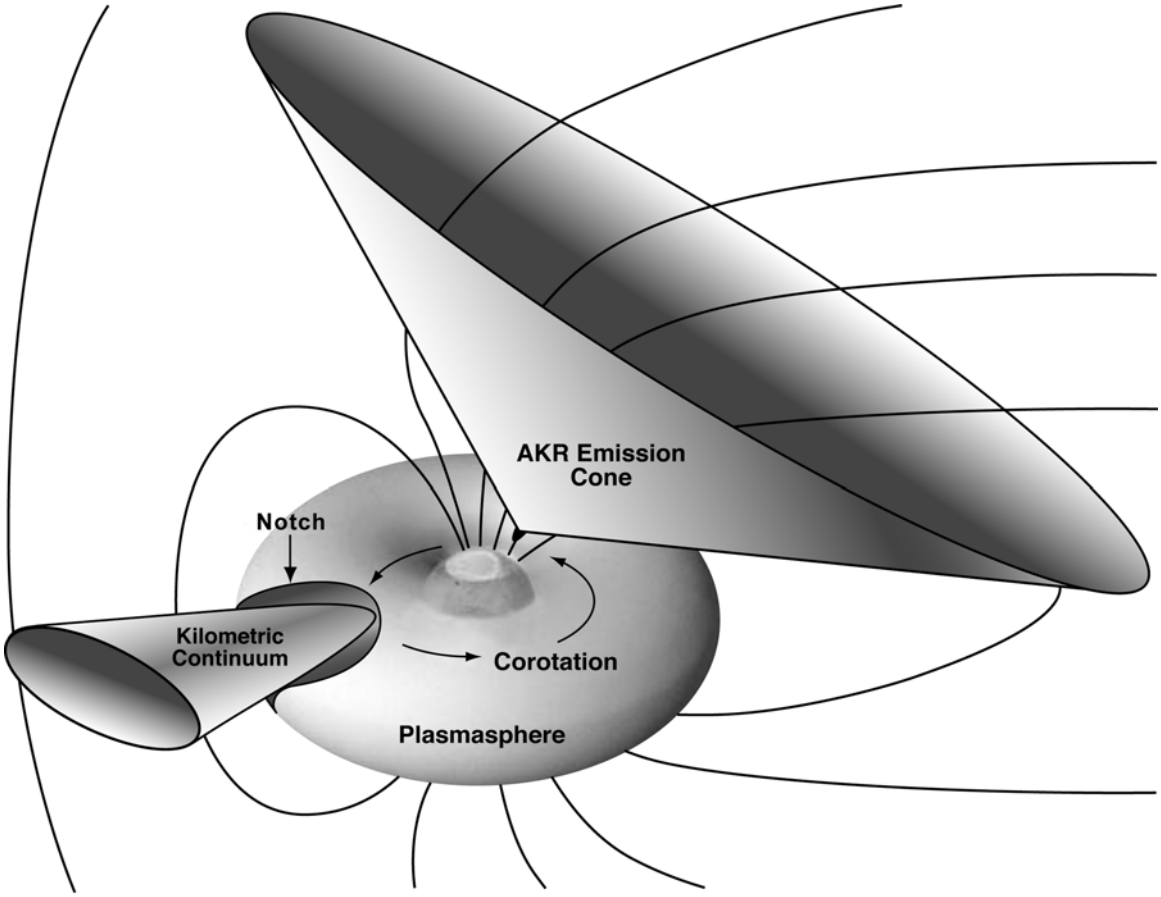

Fig. 17. Schematic of auroral and continuum radiation emission cones. The Sun is to the left; the bow shock and magnetospheric field lines are shown by the solid curves. The AKR emission cone is tilted back away from the Sun and beamed tailward while the kilometric continuum emission cone has been found to be generated at the plasmapause in notch regions of the plasmasphere and beamed into an emission cone covering typically less than 15^{o} in latitude around the magnetic equator. Adapted from Figure 11 of *Green et al*. [2002]

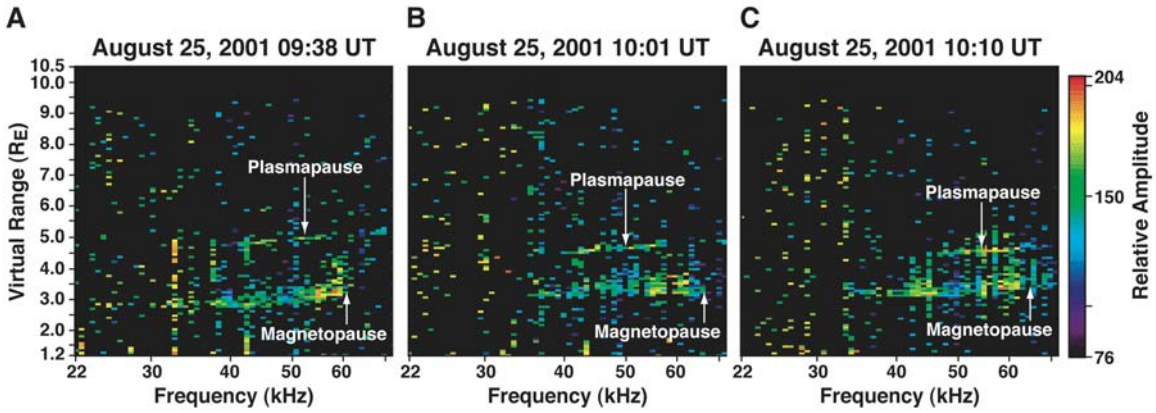

Fig. 18. Three plasmagrams from a 32-minute period when the RPI simultaneously observed the magnetopause/boundary layer and the plasmapause. The IMAGE spacecraft was just beginning the inbound portion of its trajectory from apogee during these observations. The diffuse nature of the magnetopause boundary layer echoes are an indication of the irregular nature of that boundary. [from *Green et al*., 2003]

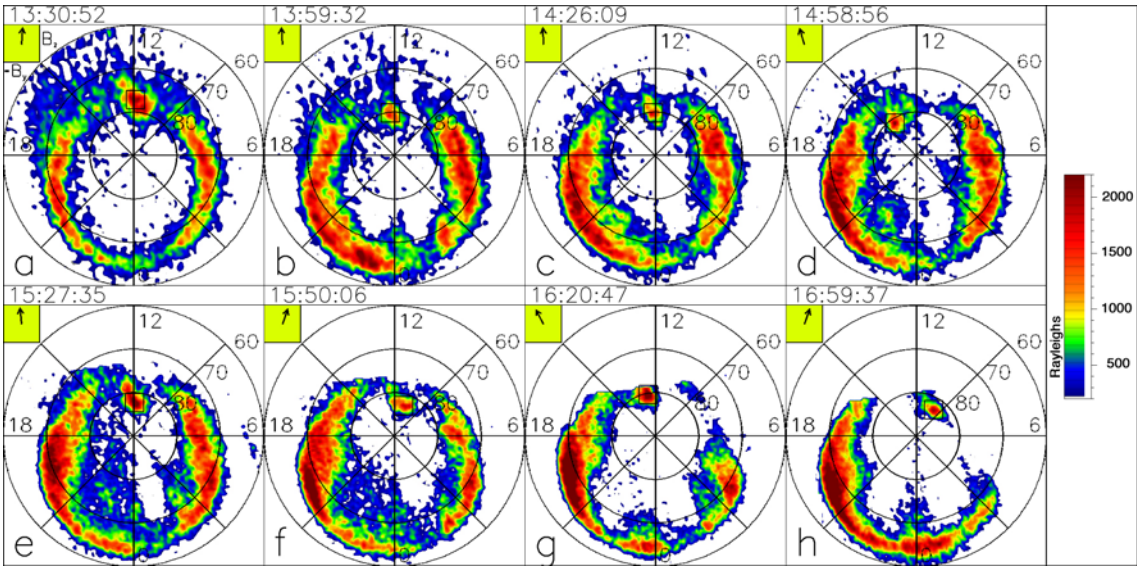

Fig. 19. Snapshots of the proton aurora on 18 March 2002 showing the continuous presence of the proton aurora spot. The images are shown in a geomagnetic grid of latitude and local time with the noon meridian at the top and 06:00 (dawn meridian) pointing to the right. The solar-wind magnetic field in the y_{GSM}–z_{GSM} plane is shown in the upper left inset, with north ($B_z > 0$) pointing up and east ($B_y > 0$) pointing to the left. The black square in each panel covers a 500 x 500 km area around the spot. The dayside proton aurora spot is seen continuously over ~4 hours. The spot appears on the dayside at ~80° latitude. Its location in magnetic local time (MLT) is correlated with the y-component of the solar-wind magnetic field, being in the pre-noon (post-noon) sector for negative (positive) B_y. Color scale shows Lyman-alpha brightness in Rayleighs. [from *Frey et al*., 2003a]

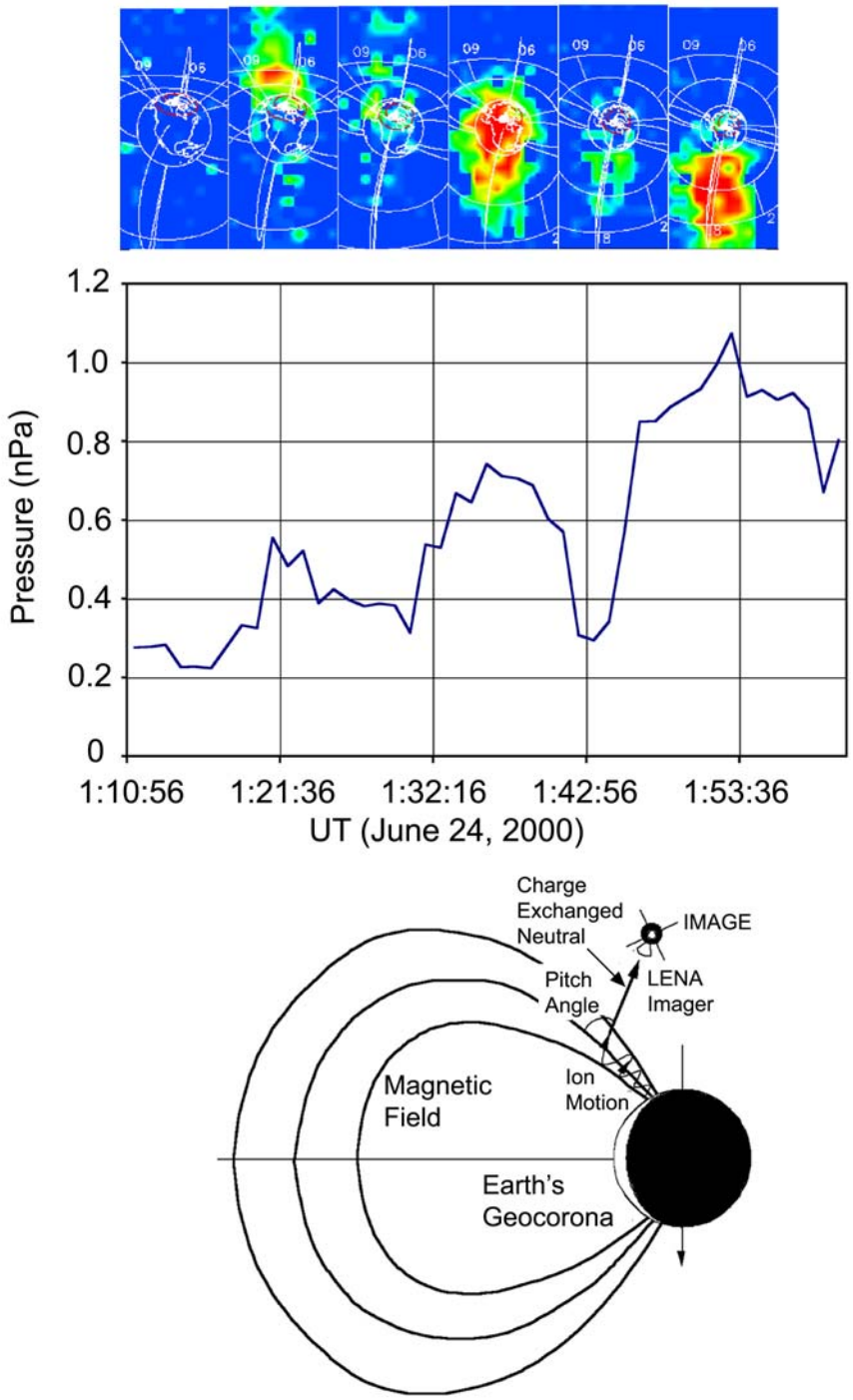

Fig. 20. LENA images of ionospheric neutral-atom outflow (top) along with Geotail solar-wind pressure data (middle) on June 24, 2000. The time delay between Geotail and the Earth was four minutes. This delay is taken into account in the time markers associating the LENA images with the Geotail data. The cartoon at the bottom illustrates the charge exchange of ionospheric outflow. Ions from the auroral oval spiral along the magnetic fields and charge exchange with exospheric neutral atoms. The resulting neutral atom propagates in a straight line. By tracing

back along the arrival direction of the atom, the charge-exchange altitude and the pitch angle of the ion is determined. [adapted from *Fuselier et al*., 2003 and *Burch*, 2003]

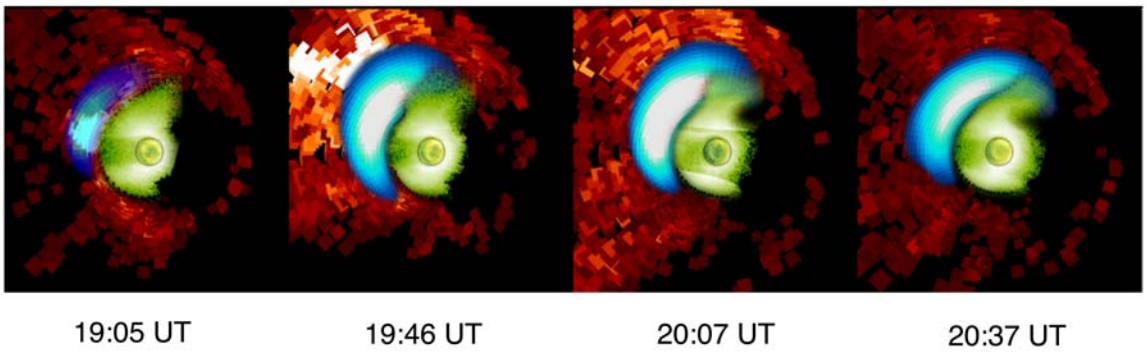

Fig. 21. Composite image on April 17, 2002 in the magnetic equatorial plane, with the Sun to the right. Orange pixels are IMAGE-FUV auroral measurements mapped to the equator. Blue pixels are ring current data from IMAGE-HENA. Green pixels are He^{+} densities from IMAGE-EUV. Figure provided by J. Goldstein.

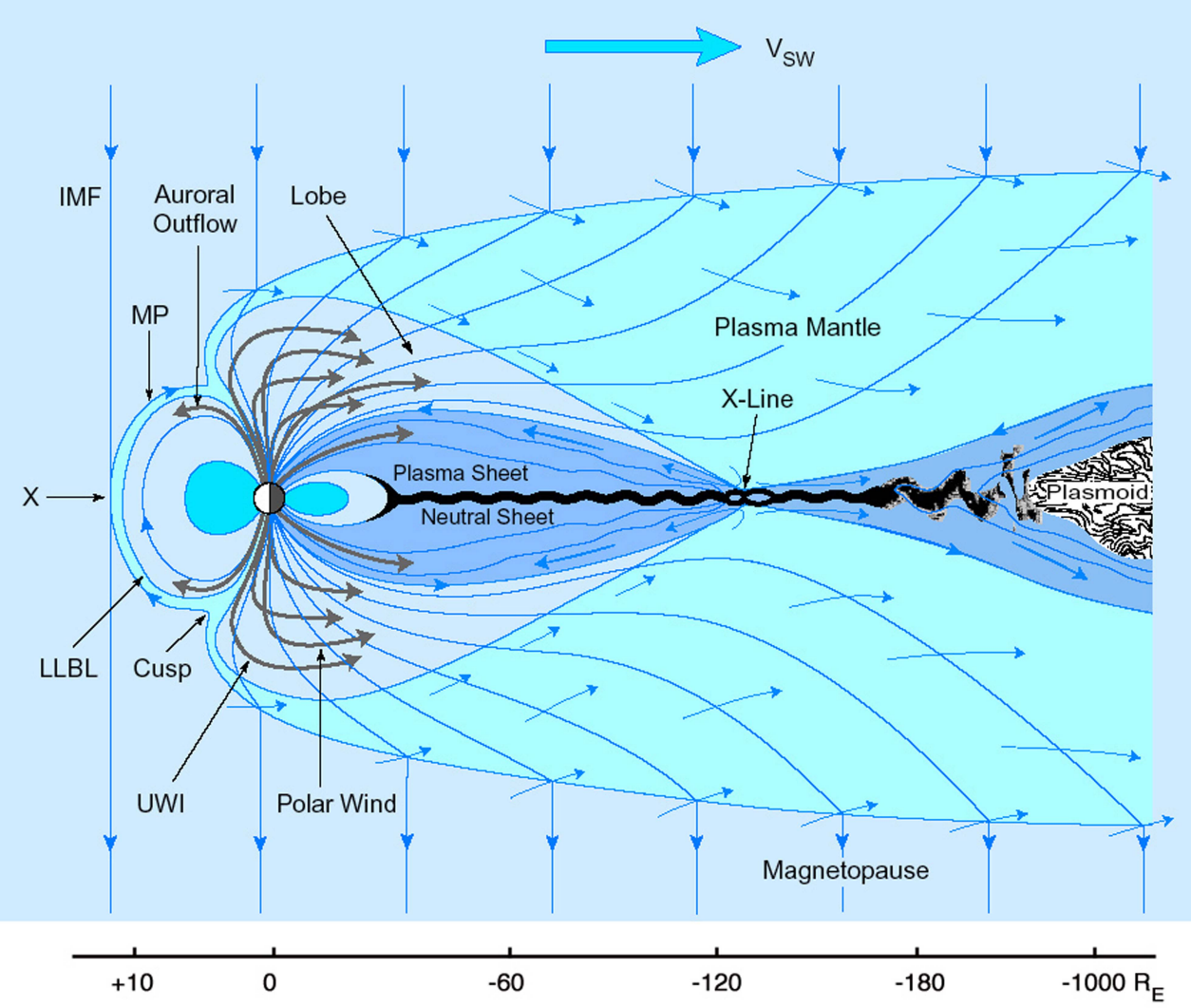
V_{SW}
IMF
Auroral Outflow
Lobe
MP
Plasma Mantle
X-Line
X
Plasma Sheet
Neutral Sheet
Plasmoid
LLBL
Cusp
UWI
Polar Wind
Magnetopause
+10
0
-60
-120
-180
-1000 R_E

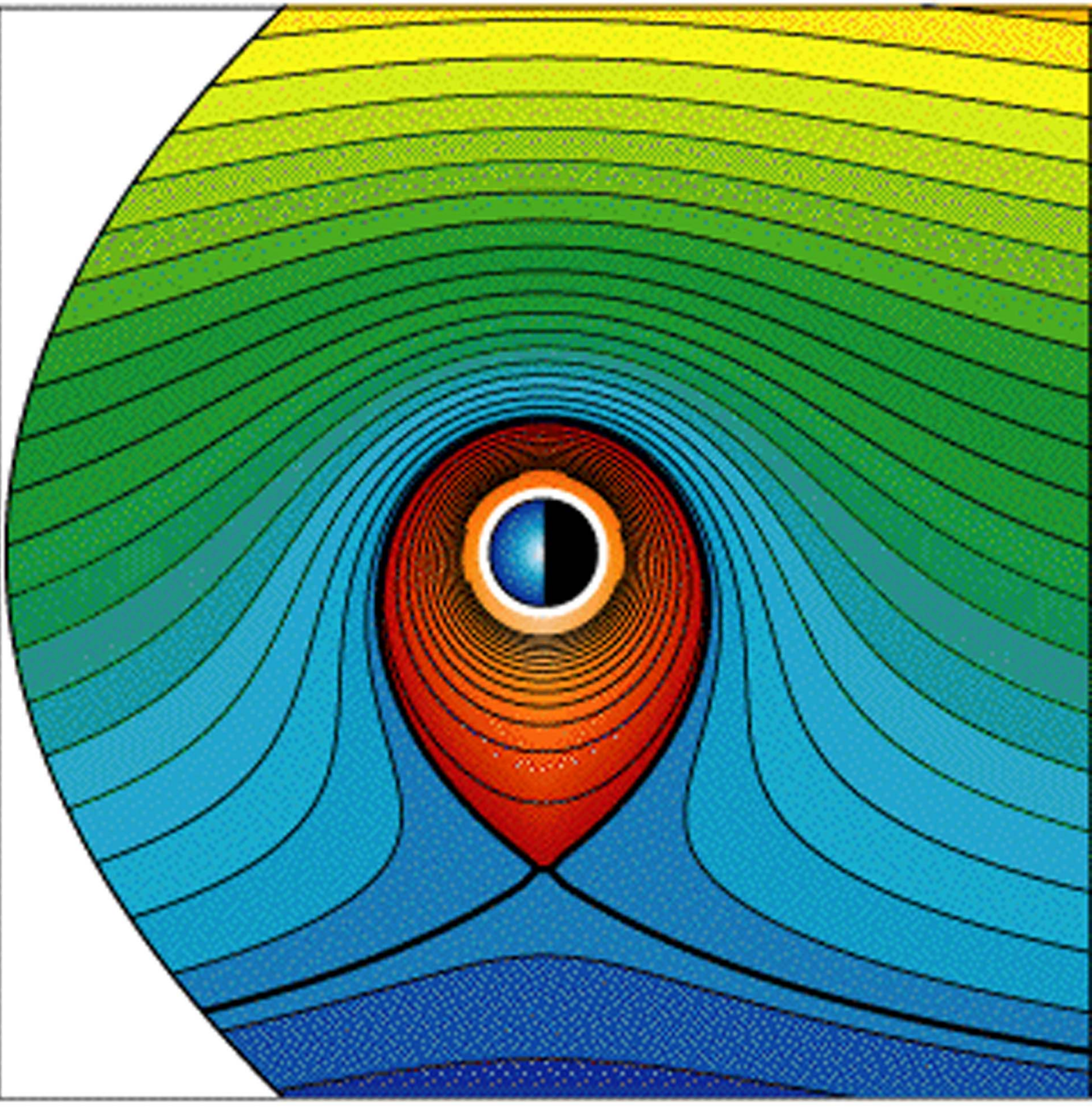

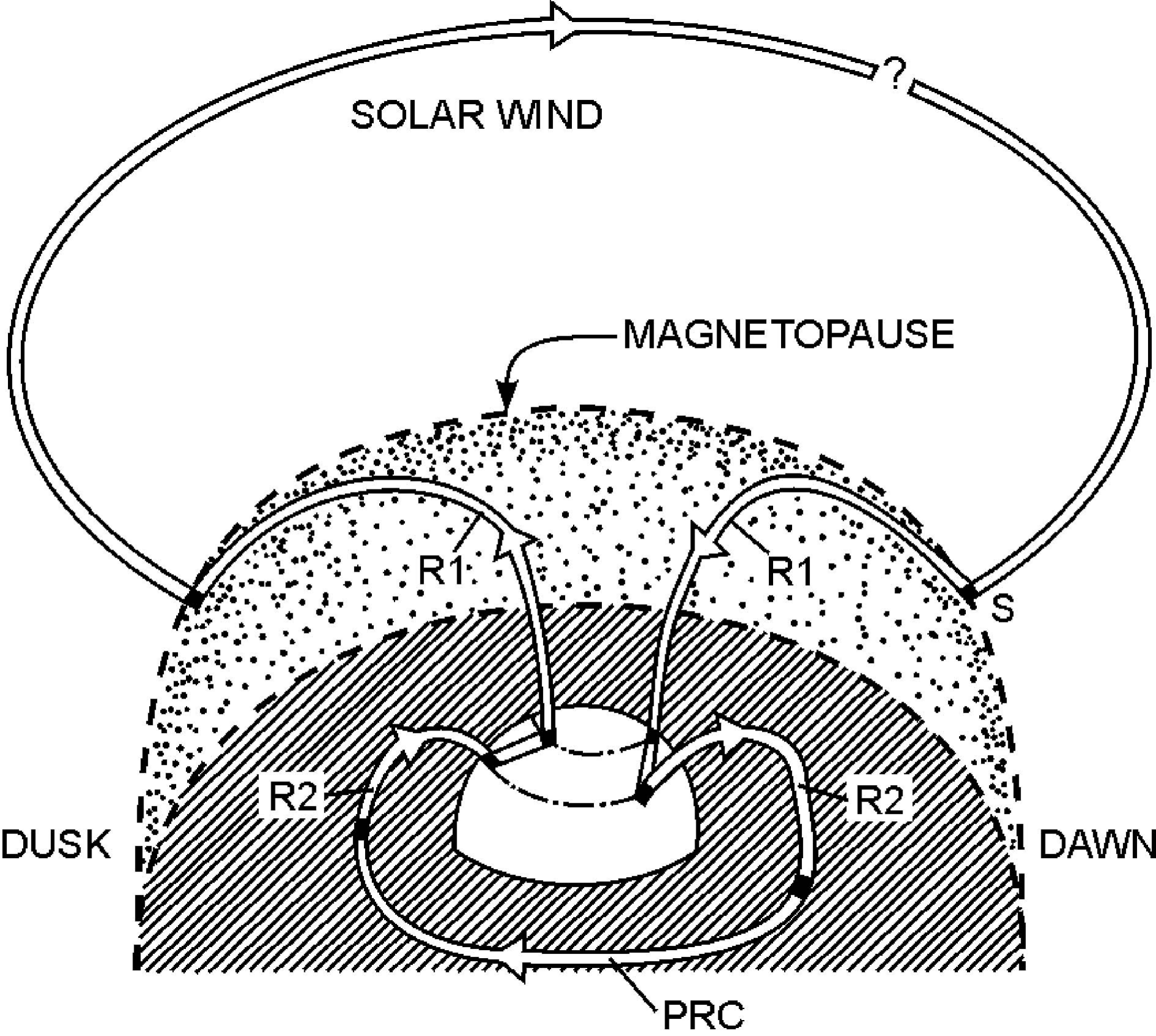

TA003916

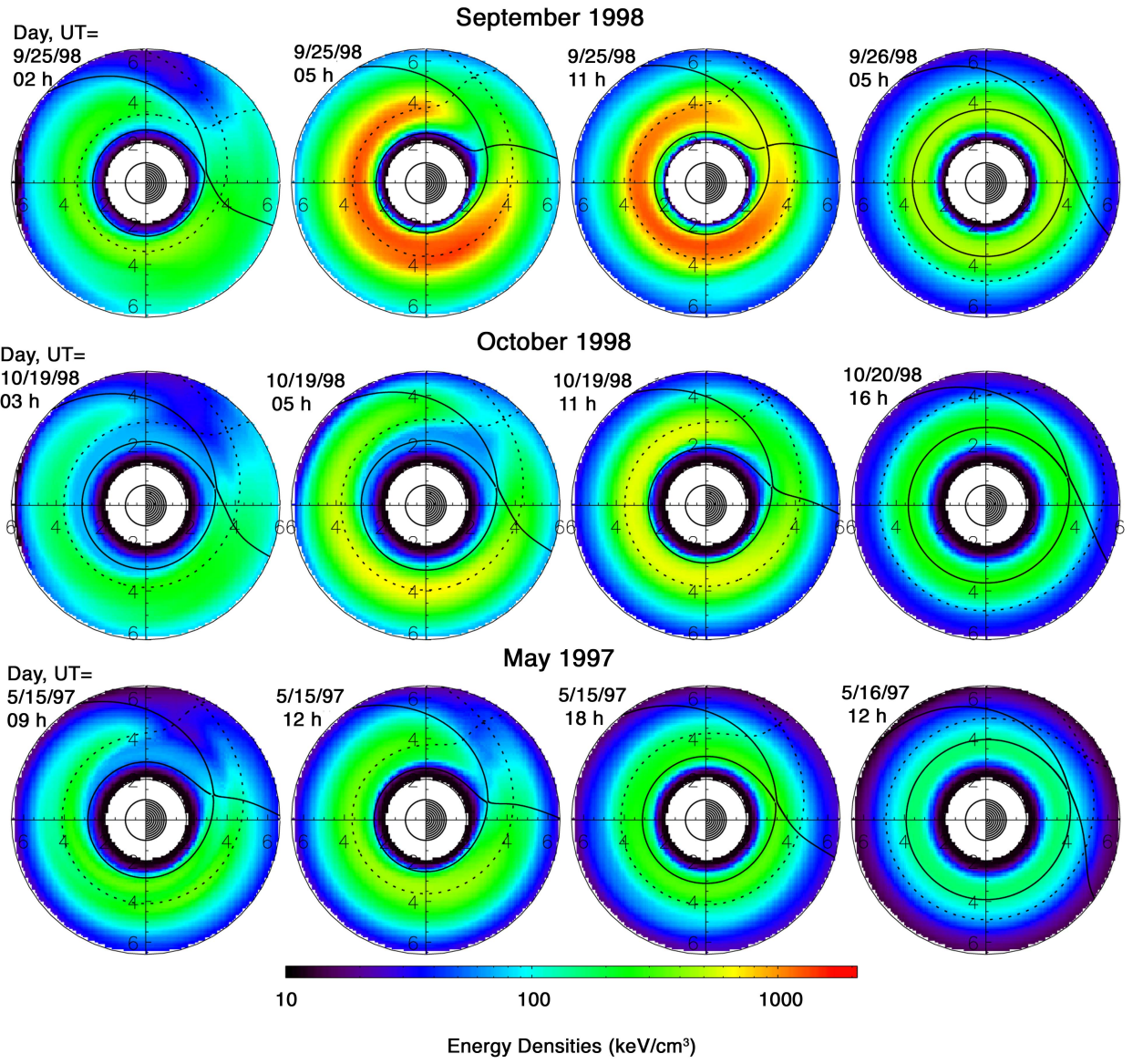
September 1998
Day, UT=
9/25/98
02 h
9/25/98
05 h
9/25/98
11 h
9/26/98
05 h
October 1998
Day, UT=
10/19/98
03 h
10/19/98
05 h
10/19/98
11 h
10/20/98
16 h
May 1997
Day, UT=
5/15/97
09 h
5/15/97
12 h
5/15/97
18 h
5/16/97
12 h
10
100
1000
Energy Densities (keV/cm³)

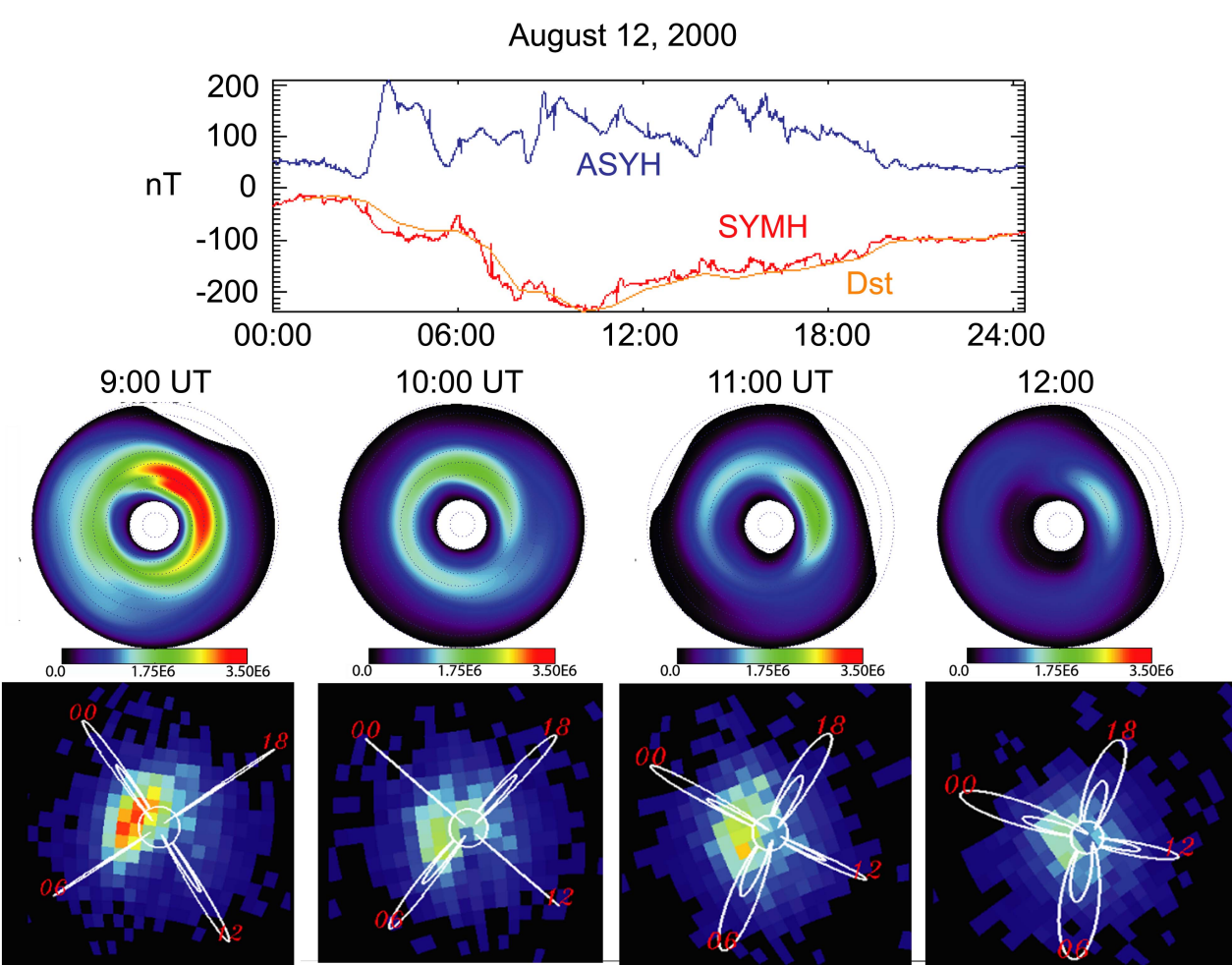
August 12, 2000
200
100
0
-100
-200
nT
ASYH
SYMH
Dst
00:00
06:00
12:00
18:00
24:00
9:00 UT
10:00 UT
11:00 UT
12:00
0.0
1.75E6
3.50E6
00
18
06
12

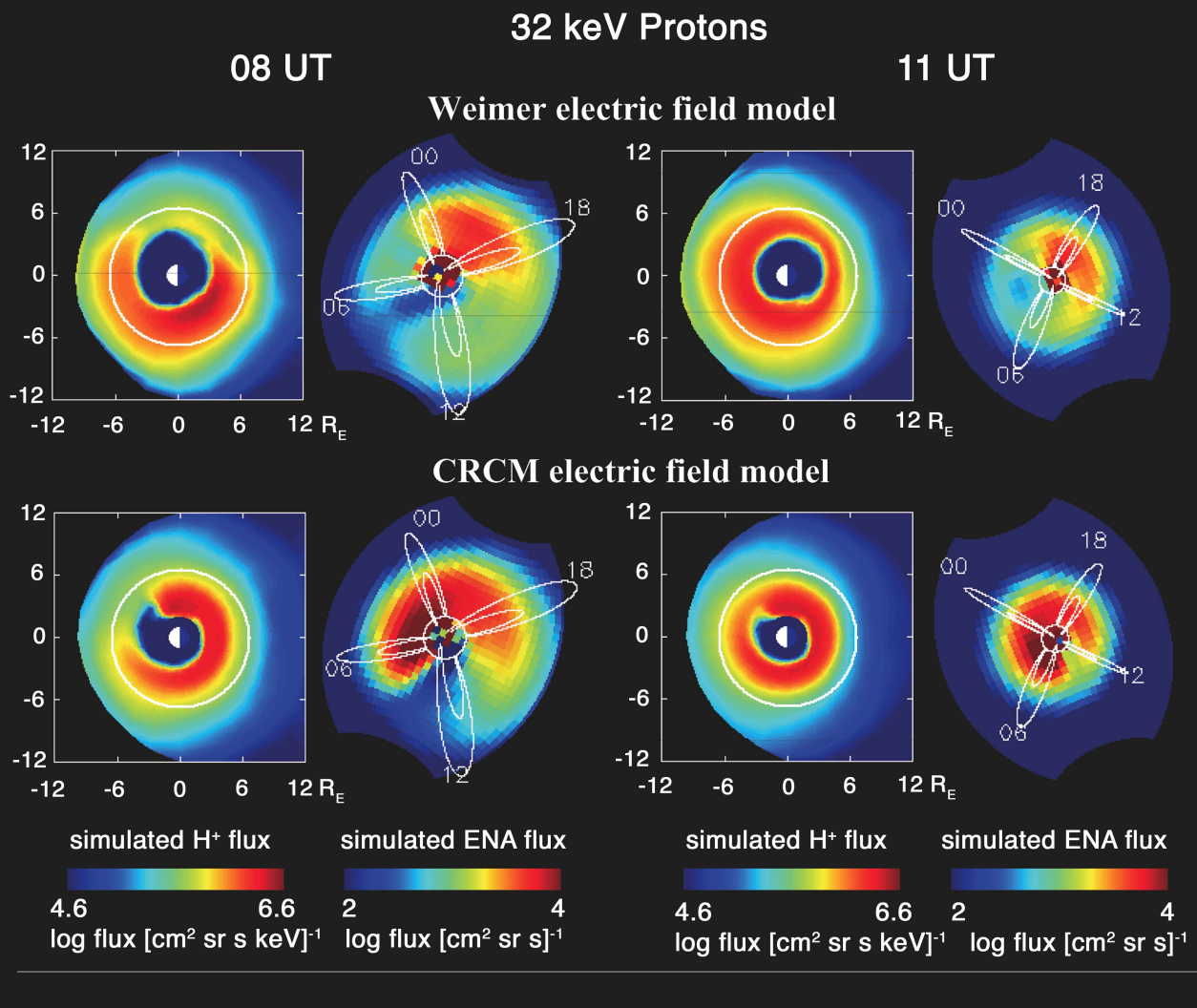
32 keV Protons
08 UT
11 UT
Weimer electric field model
CRCM electric field model
12
6
0
-6
-12
-12 -6 0 6 12 R_E
00
06
12
18
simulated H+ flux
4.6
6.6
log flux [cm² sr s keV]-1
simulated ENA flux
2
4
log flux [cm² sr s]-1

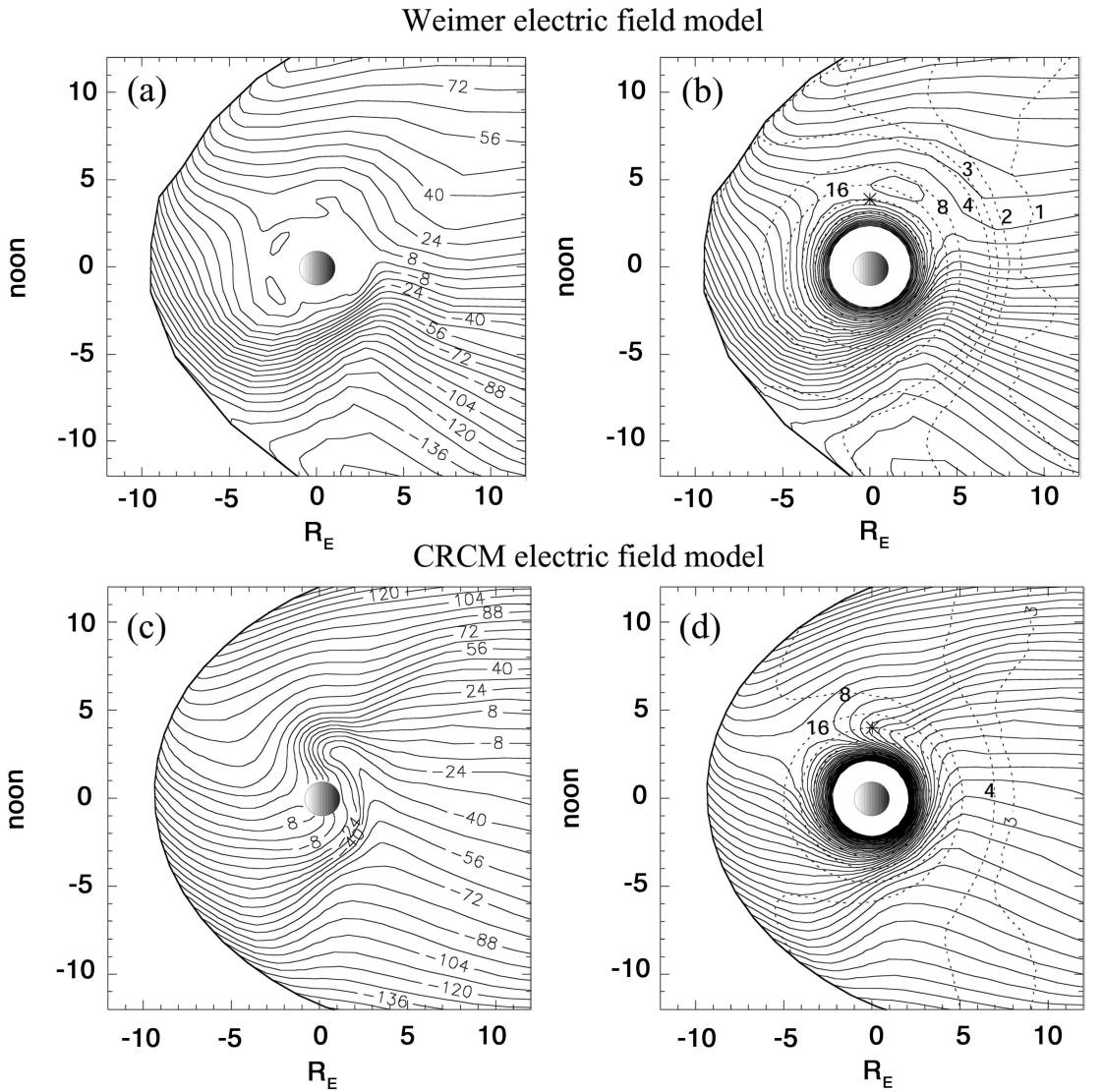
Weimer electric field model
(a)
(b)
CRCM electric field model
(c)
(d)
noon
R_E
10
5
0
-5
-10
72
56
40
24
8
-8
-24
-40
-56
-72
-88
-104
-120
-136
16
8
4
3
2
1
120
104
88

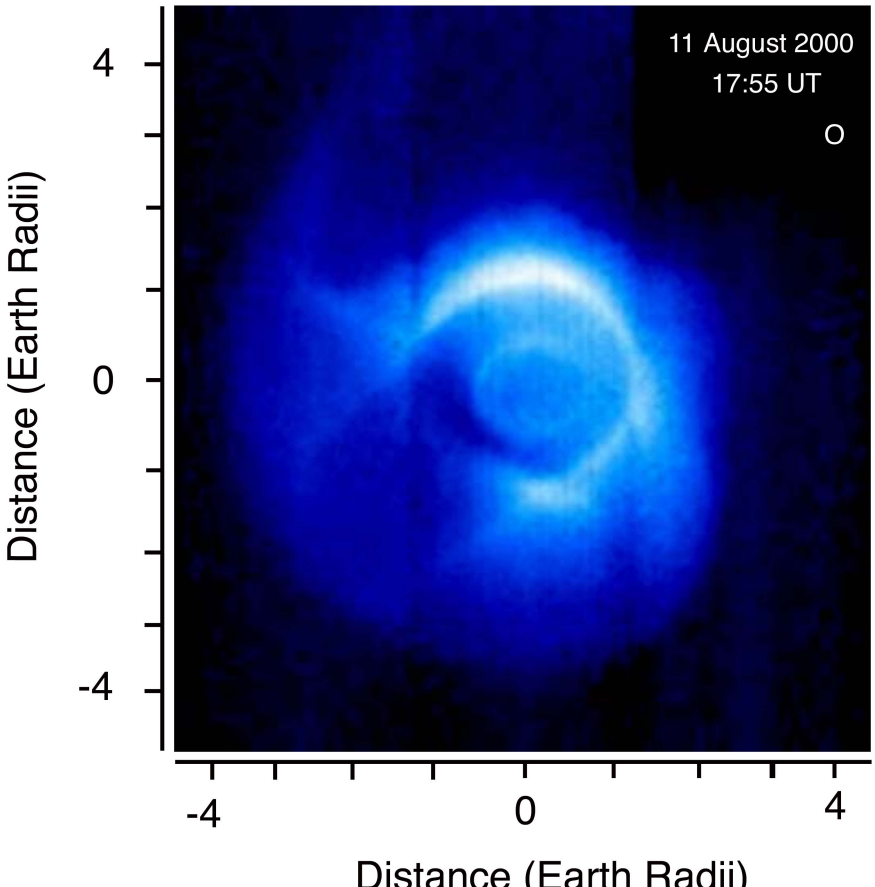
11 August 2000
17:55 UT
O
4
0
-4
Distance (Earth Radii)
-4
0
4
Distance (Earth Radii)

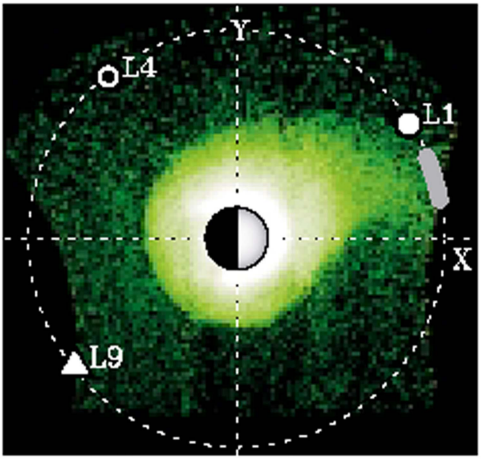
Y
L4
L1
X
L9

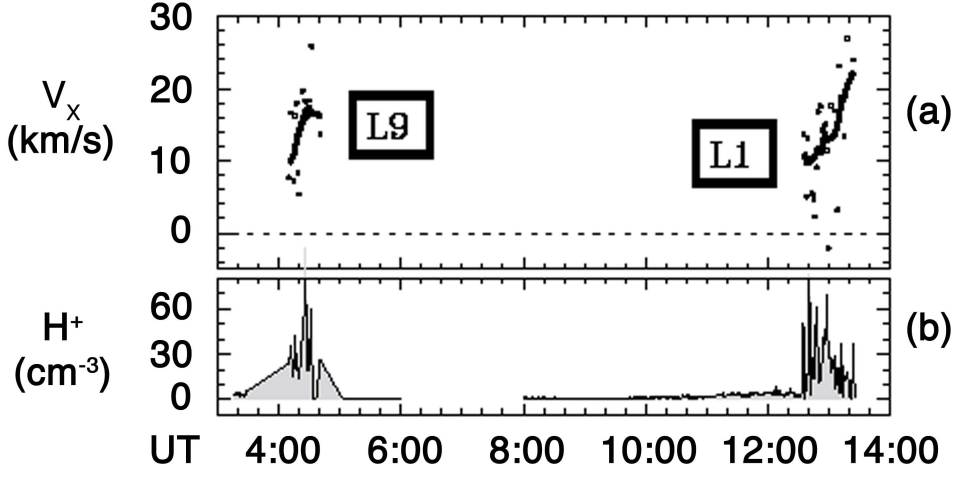
30
20
10
0
V_X
(km/s)
L9
L1
(a)
60
30
0
H^+
(cm^{-3})
(b)
UT
4:00
6:00
8:00
10:00
12:00
14:00

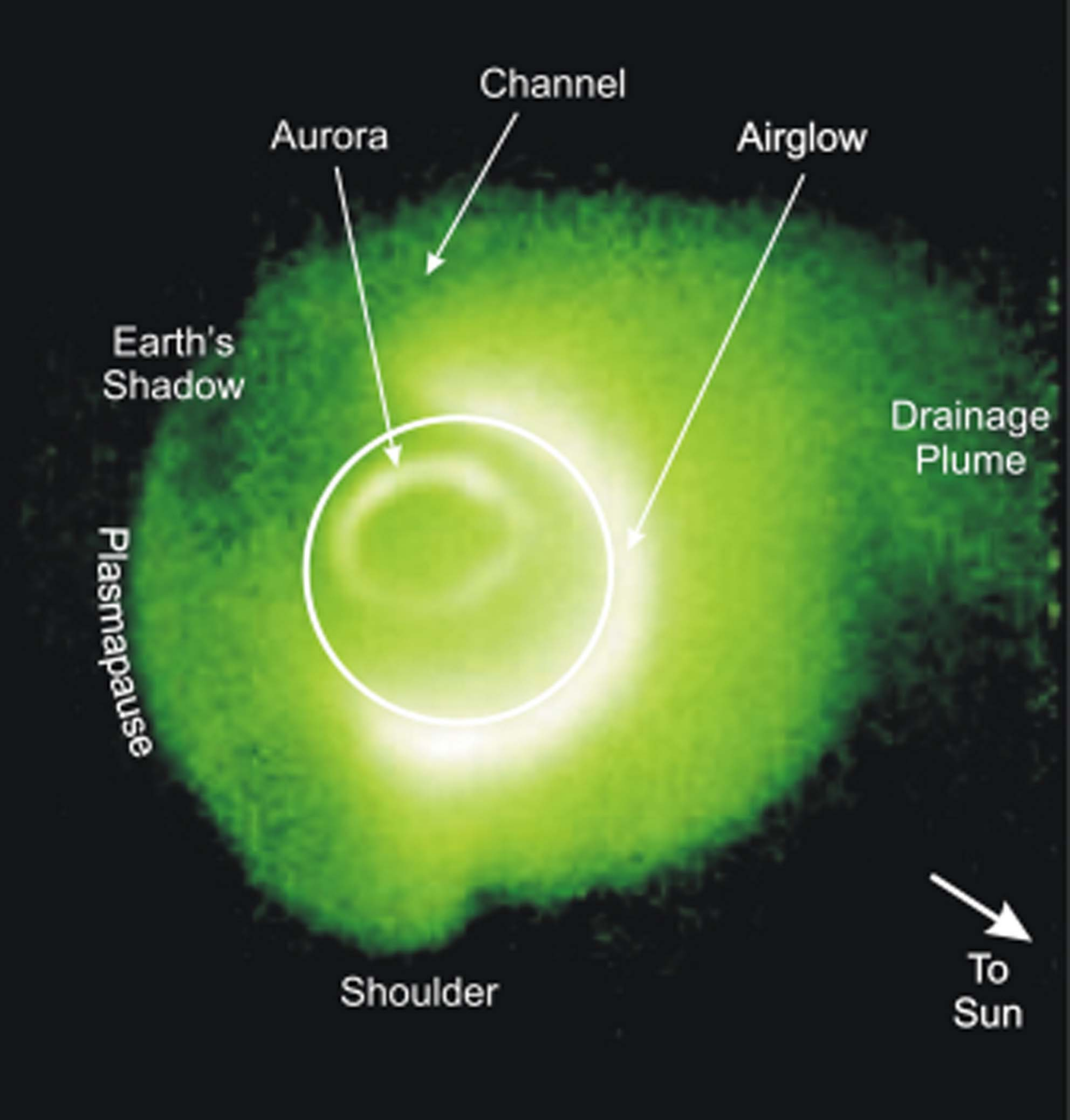
Channel
Aurora
Airglow
Earth's
Shadow
Drainage
Plume
Plasmapause
Shoulder
To
Sun

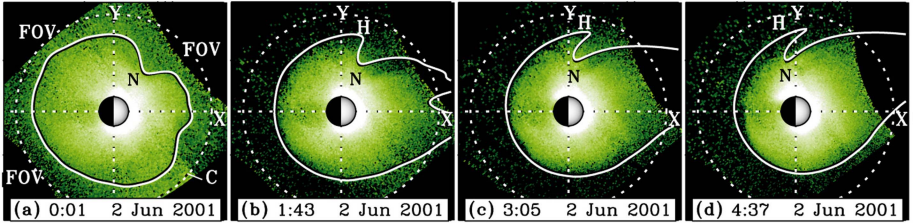
FOV
Y
FOV
N
X
FOV
C
(a) 0:01 2 Jun 2001
H
(b) 1:43 2 Jun 2001
(c) 3:05 2 Jun 2001
(d) 4:37 2 Jun 2001

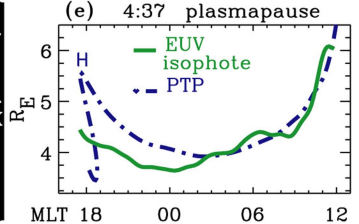
(e) 4:37 plasmapause
EUV
isophote
PTP
H
R_E
6
5
4
MLT 18 00 06 12

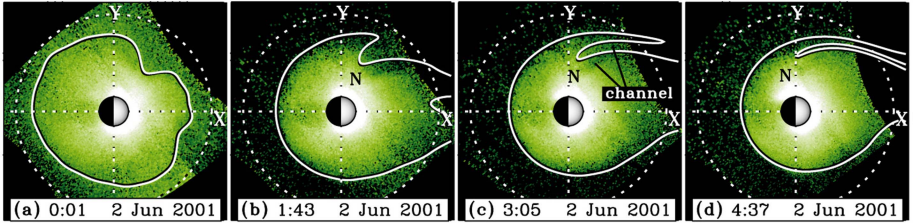
Y
X
N
channel
(a) 0:01 2 Jun 2001
(b) 1:43 2 Jun 2001
(c) 3:05 2 Jun 2001
(d) 4:37 2 Jun 2001

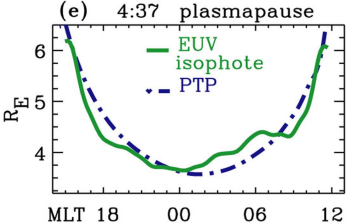
(e) 4:37 plasmapause
EUV
isophote
PTP
R_E
6
5
4
MLT 18
00
06
12

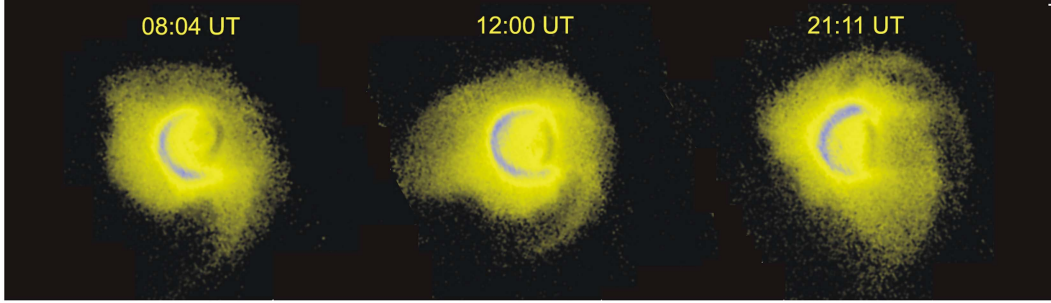
08:04 UT
12:00 UT
21:11 UT

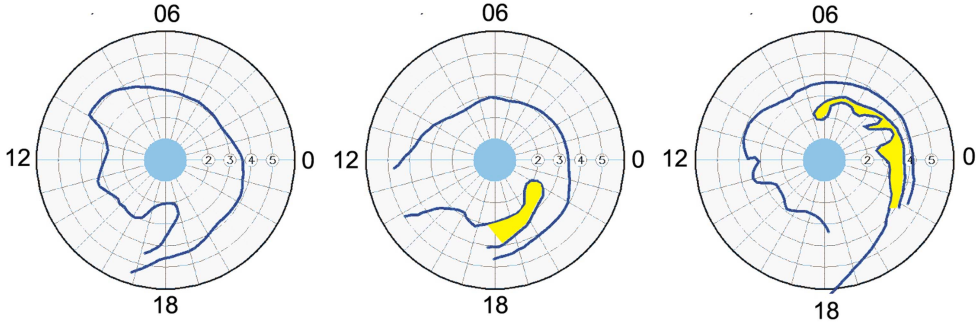
06
12
0
18
2
3
4
5

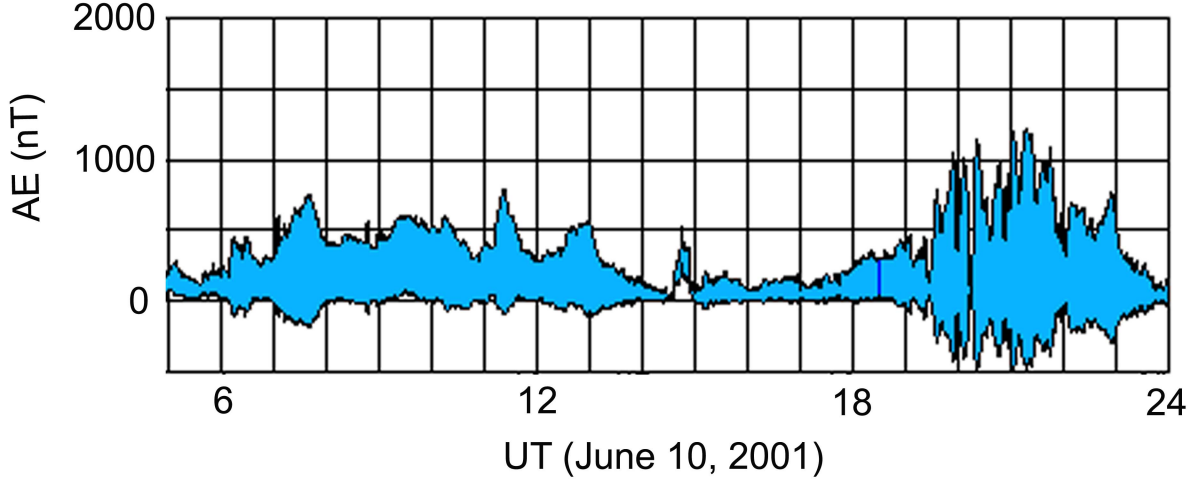
2000
1000
0
AE (nT)
6
12
18
24
UT (June 10, 2001)

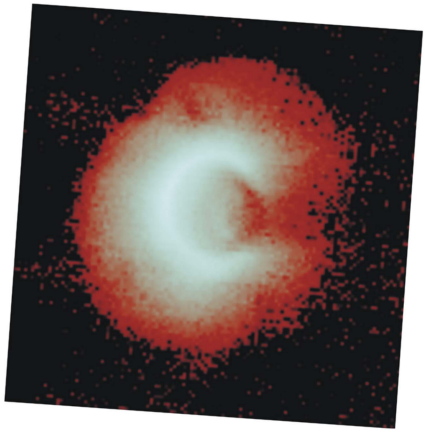
a

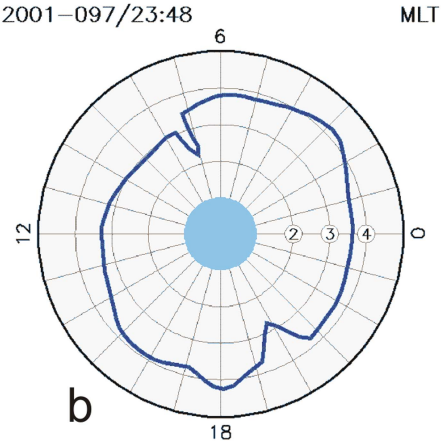
2001−097/23:48
MLT
6
12
0
18
2
3
4
b

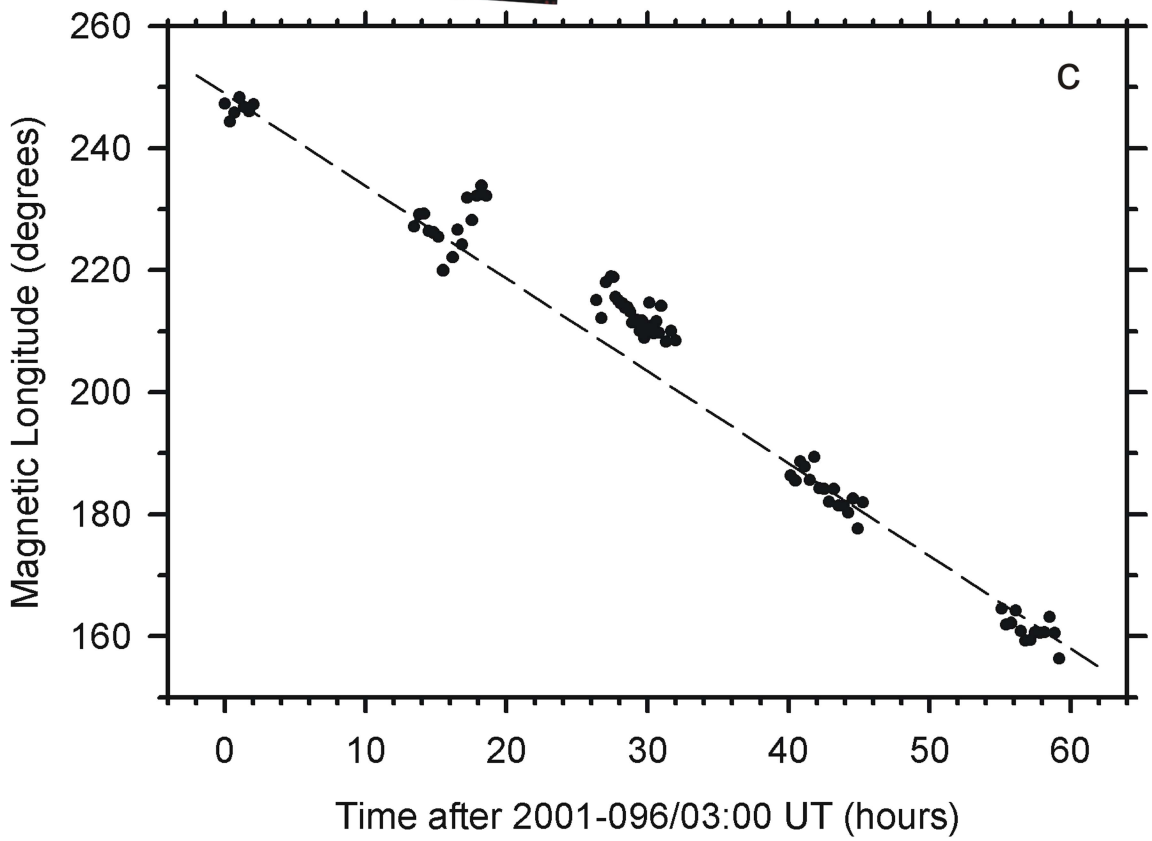
c
Magnetic Longitude (degrees)
260
240
220
200
180
160
0
10
20
30
40
50
60
Time after 2001-096/03:00 UT (hours)

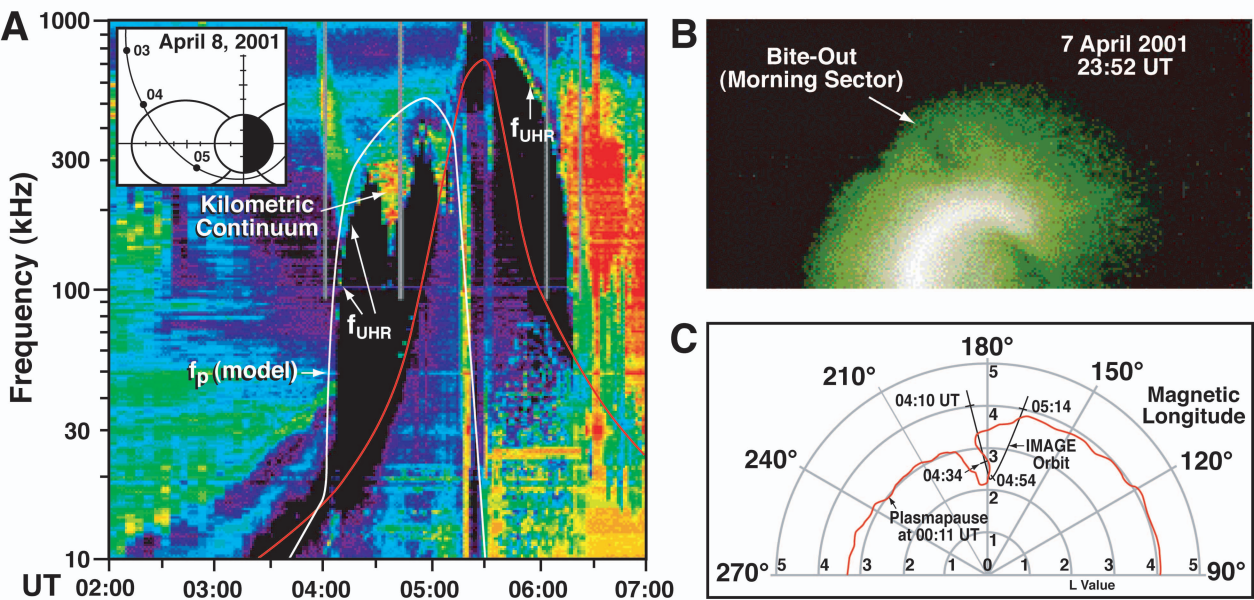
A
April 8, 2001
03
04
05
Kilometric Continuum
f_{UHR}
f_{UHR}
f_p (model)
Frequency (kHz)
1000
300
100
30
10
UT
02:00
03:00
04:00
05:00
06:00
07:00
B
Bite-Out (Morning Sector)
7 April 2001
23:52 UT
C
180°
210°
150°
240°
120°
270°
90°
Magnetic Longitude
04:10 UT
05:14
IMAGE Orbit
04:34
04:54
Plasmapause at 00:11 UT
L Value

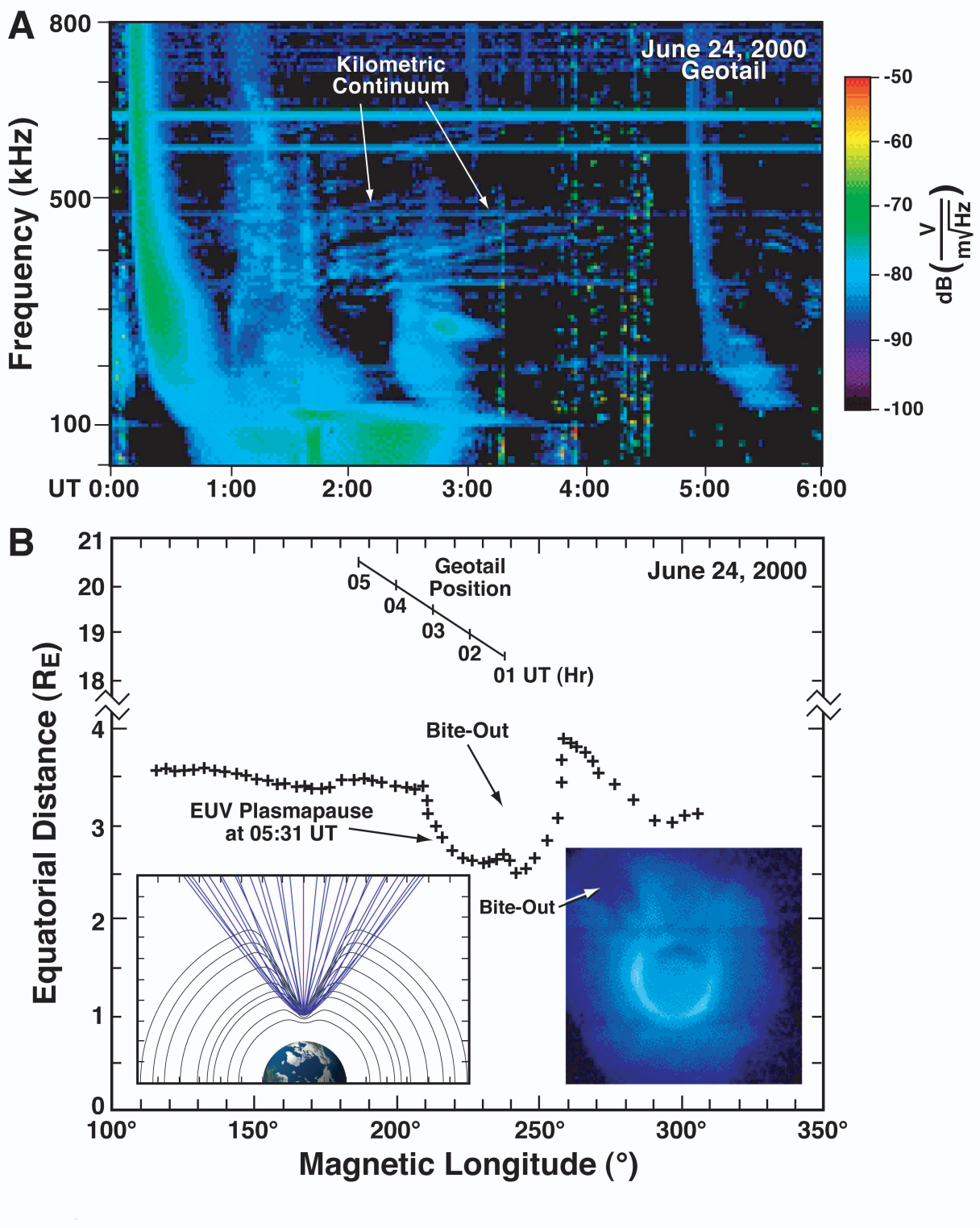
A
800
500
100
Frequency (kHz)
Kilometric
Continuum
June 24, 2000
Geotail
-50
-60
-70
-80
-90
-100
dB(V/m√Hz)
UT 0:00
1:00
2:00
3:00
4:00
5:00
6:00
B
21
20
19
18
4
3
2
1
0
Equatorial Distance (RE)
Geotail
Position
05
04
03
02
01 UT (Hr)
June 24, 2000
Bite-Out
EUV Plasmapause
at 05:31 UT
Bite-Out
100°
150°
200°
250°
300°
350°
Magnetic Longitude (°)

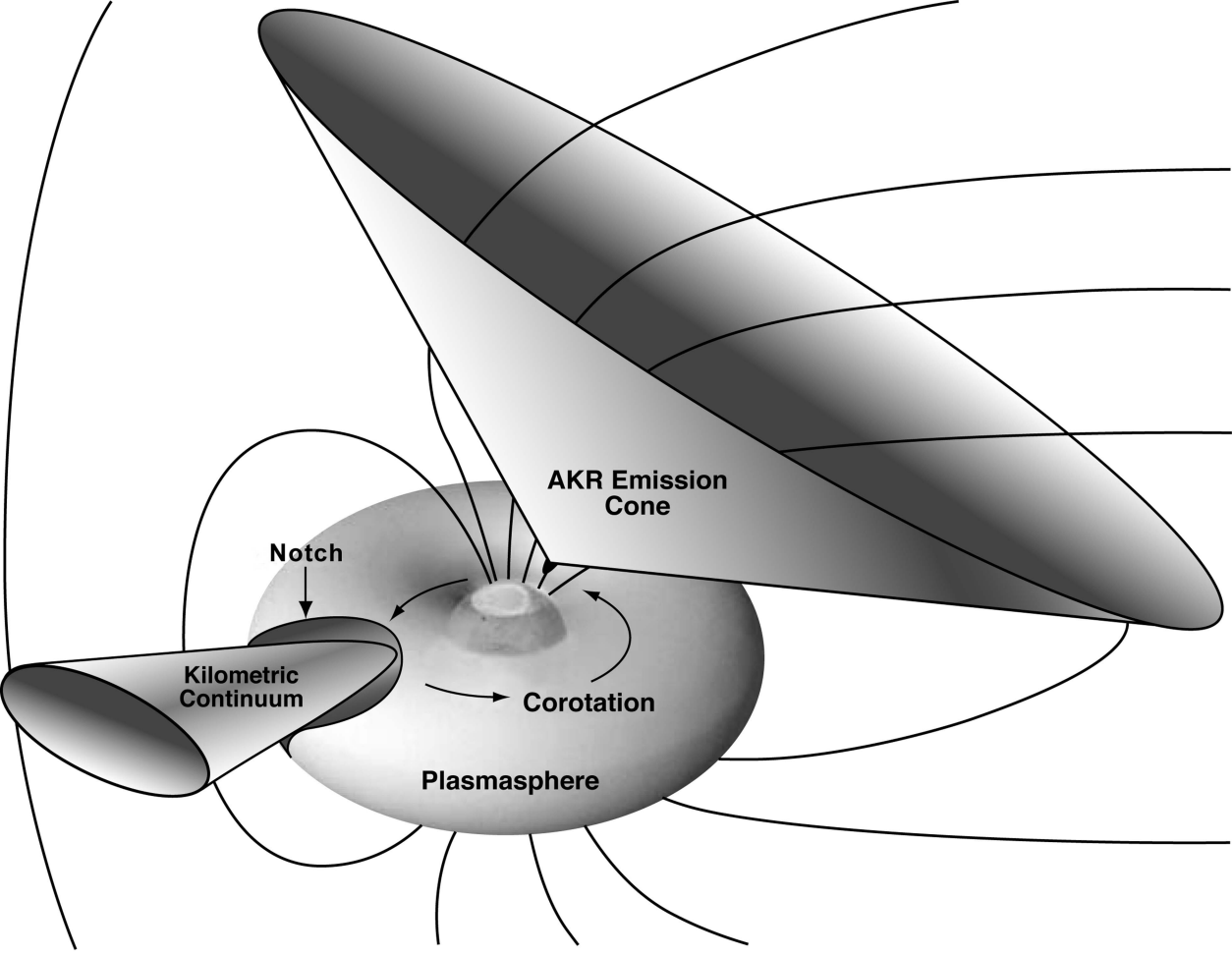
AKR Emission
Cone
Notch
Kilometric
Continuum
Corotation
Plasmasphere

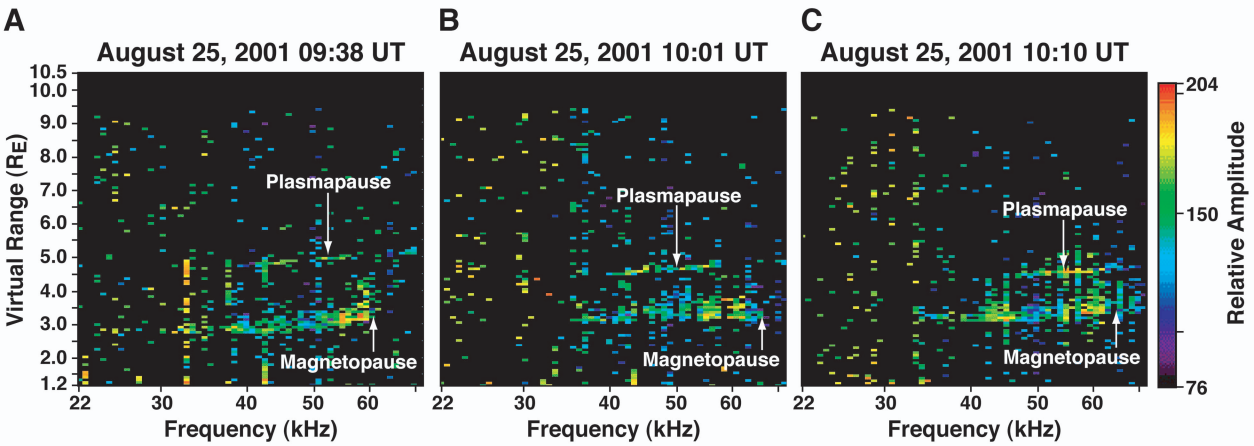
A
August 25, 2001 09:38 UT
B
August 25, 2001 10:01 UT
C
August 25, 2001 10:10 UT
Virtual Range (RE)
10.5
10.0
9.0
8.0
7.0
6.0
5.0
4.0
3.0
2.0
1.2
Plasmapause
Magnetopause
22
30
40
50
60
Frequency (kHz)
204
150
76
Relative Amplitude

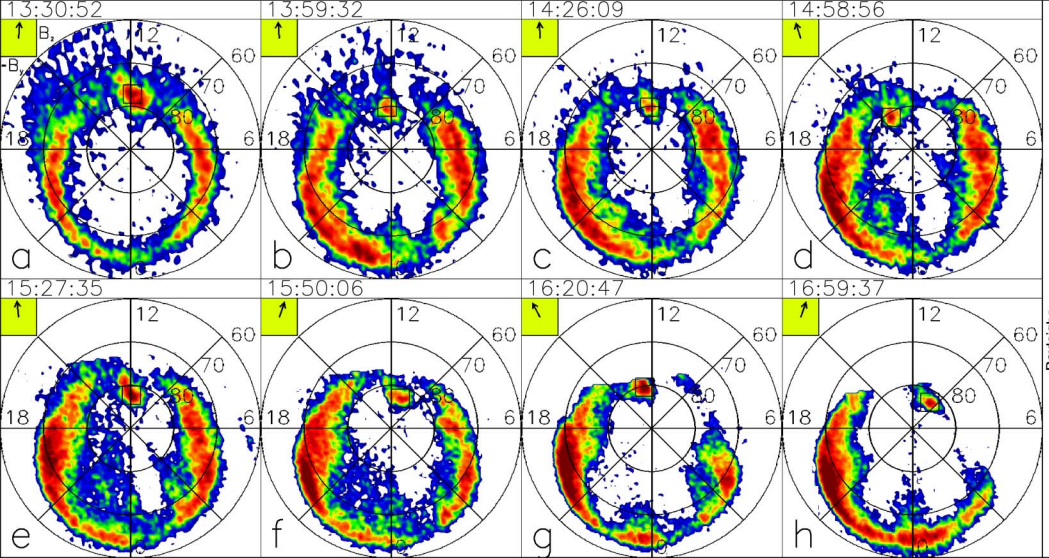
13:30:52
13:59:32
14:26:09
14:58:56
15:27:35
15:50:06
16:20:47
16:59:37
B_z
-B_z
12
60
70
80
18
6
a
b
c
d
e
f
g
h
2000
1500
1000
500
Rayleighs

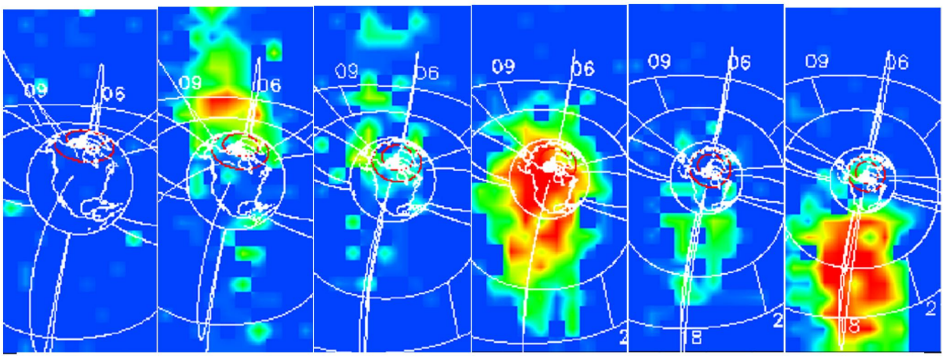
09
06

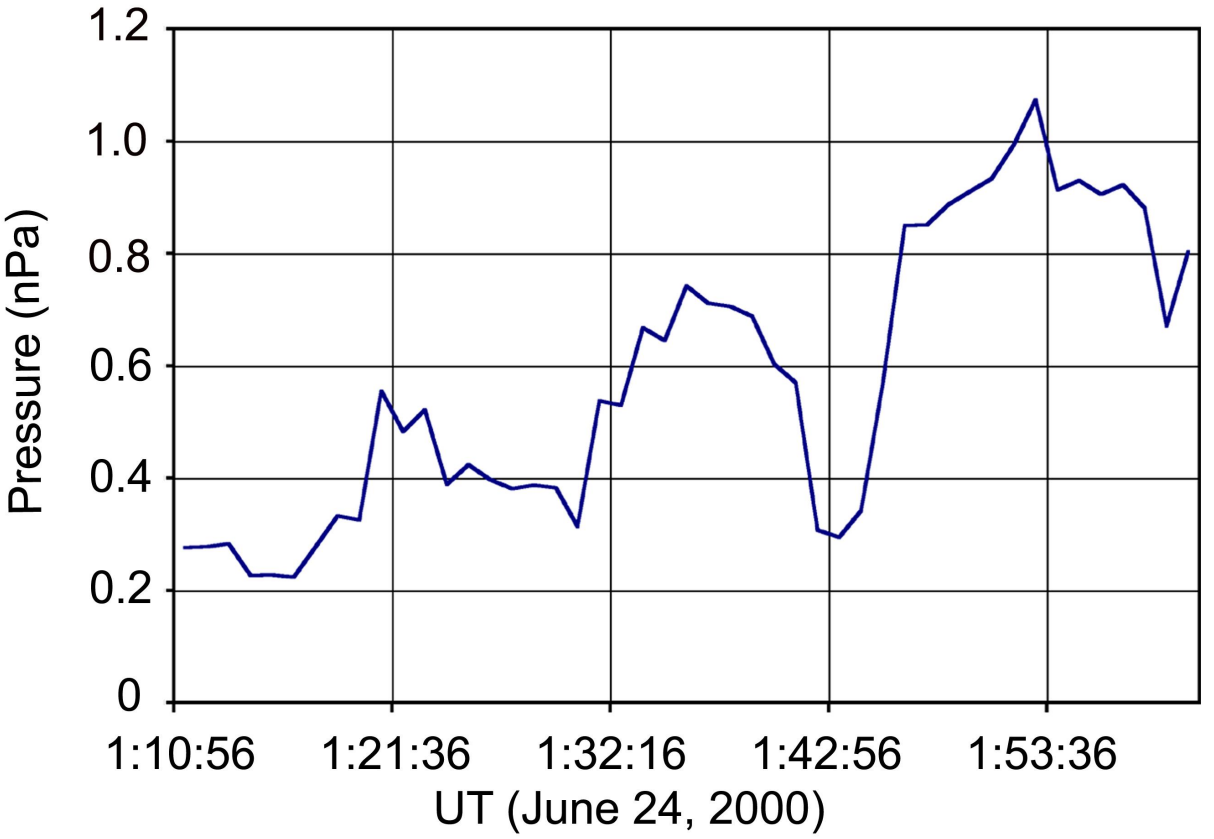
Pressure (nPa)
1.2
1.0
0.8
0.6
0.4
0.2
0
1:10:56
1:21:36
1:32:16
1:42:56
1:53:36
UT (June 24, 2000)

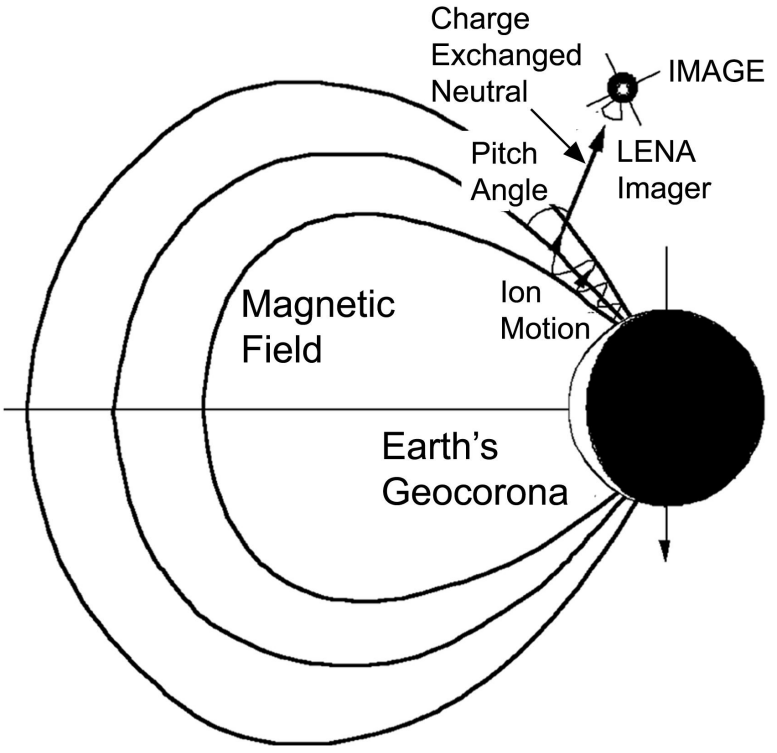
Charge
Exchanged
Neutral
IMAGE
Pitch
Angle
LENA
Imager
Ion
Motion
Magnetic
Field
Earth's
Geocorona

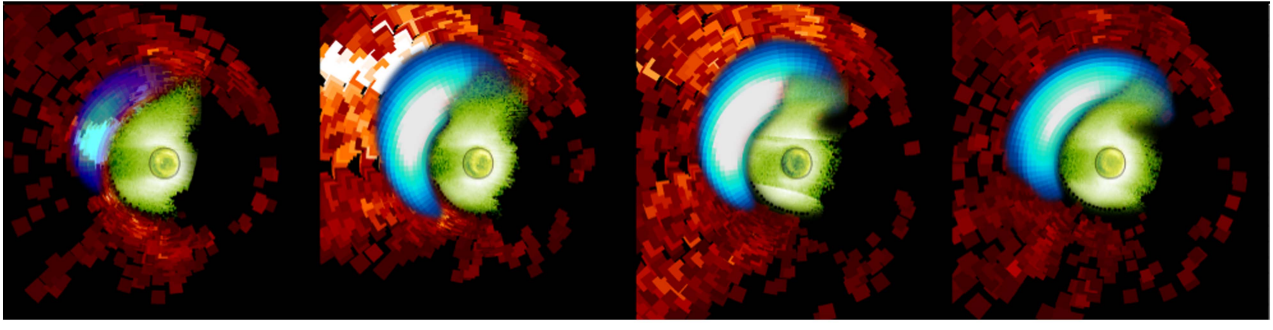

19:05 UT

19:46 UT

20:07 UT

20:37 UT